COOLING AND EXHUMATION OF THE HIMALAYAN MID-CRUST, KHIMTI-TAMAKOSHI-SINDHULIGADHI SECTION, EAST CENTRAL NEPAL

by

Kumar K C

A THESIS SUBMITTED IN PARTIAL FULFILLMENT OF
THE REQUIREMENTS FOR THE DEGREE OF

MASTER OF SCIENCE

in

THE COLLEGE OF GRADUATE STUDIES

(Environmental Sciences)

THE UNIVERSITY OF BRITISH COLUMBIA

(Okanagan)

July 2017

The undersigned certify that they have read, and recommend to the College of Graduate Studies for acceptance, a thesis entitled:

Cooling and exhumation of the Himalayan mid-crust, Khimti-Tamakoshi-Sindhuligadhi section, east central Nepal

submitted by Kumar K C in partial fulfilment of the requirements of

Dr. Kyle P. Larson, Department of Earth, Environmental and Geographic Sciences
Supervisor, Associate Professor

Dr. John Greenough, Department of Earth, Environmental and Grographic Sciences
Supervisory Committee Member, Professor

Dr. Yuan Chen, Department of Earth, Environmental and Geographic Sciences
Supervisory Committee Member, Associate Professor

Dr. Kevin Smith, Department of Chemistry
University Examiner, Professor

Dr. Ross Hickey, Department of Economics, Philosophy and Political Science
Neutral Chair, Assistant Professor

Abstract

This thesis presents a new $^{40}Ar^*/^{39}Ar$ thermochronologic dataset that constrains the cooling history of the exhumed, former mid-crust exposed in the Khimti-Tamakoshi-Sindhuligadhi section of east-central Nepal. These results are incorporated with existing geological and geochronological data to prepare a revised, internally consistent kinematic model of the geologic evolution of the study area.

Except for those from the highest structural levels, biotite examined as part of this study are contaminated with excess argon and therefore yield anomalously old, geologically meaningless ages. Muscovite cooling ages, however, are more robust, and constrain the timing of exhumation of the leading edge of the Himalayan Metamorphic Core to the late Oligocene/early Miocene in advance of deeper-seated material in the orogenic hinterland. Most of the muscovite ages from rocks in the lower part of the Himalayan Metamorphic Core are partially reset, indicating that these rocks experienced only limited burial and heating prior to exhumation. The structural position and cooling ages of these partially reset rocks indicate their incorporation into the thrust system through underplating and subsequent exhumation facilitated by out-of-sequence thrusting. Cooling ages obtained from the more hinterland, structurally higher portion of the Himalayan Metamorphic Core are consistent with it evolving as a result of movement along multiple late-stage, thrust-sense structures. These faults, which facilitated cooling as young as late Miocene, occur as discrete out-of-sequence thrust sheets within the Himalayan Metamorphic Core. These out-of-sequence structures, which have not been accounted for in total shortening estimates across the Himalaya, accommodated significant convergence and helped modify the shape/geometries of the original midcrustal structures. This indicates a need to revisit existing models of the orogen that integrate the current orientation of the major structures as representative of past geometries.

Preface

I conducted major portion of the research and writing included in this thesis including parts of the field work, specimen collection and description; petrographic study; $^{40}Ar^*/^{39}Ar$ specimen preparation and dating; electron microprobe analysis; interpretation of results and conclusions. Dr. Kyle Larson provided guidance, supervision and editorial support to the work. $^{40}Ar^*/^{39}Ar$ dating and electron microprobe analyses were carried out at the University of Manitoba, Winnipeg under the guidance of Dr. Alfredo Camacho. Part of the field work in Tamakoshi section including specimen collection and thin-section preparation was done by Richard Fromage. Sudip Shrestha conducted field work and specimen collection in the Khimti Khola section. He was a part of the field work in the lower Tamakoshi and Sindhuligadhi section.

Table of Contents

Abstract iii
Preface iv
List of Tables viii
List of Figures ix
Acknowledgements x

Chapter 1 Introduction 1
1.1 The Himalaya 1
1.2 Geologic Background 1
1.2.1 Tethys Sedimentary Sequence 3
1.2.2 Greater Himalayan Sequence 3
1.2.3 Lesser Himalayan Sequence 5
1.2.4 Sub-Himalaya 5
1.3 Kinematic Evolution of the Himalaya 6
1.4 Exhumation and Metamorphism 9
1.5 Current Study 9

Chapter 2 Methods 14
1.2 $^{40}Ar^*/^{39}Ar$ Thermochronology Overview 14
2.2 Procedure 16
2.3 Data Presentation and Analysis 18
2.4 Extraneous Argon 21
2.5 Closure Temperature 22

Chapter 3 $^{40}Ar^*/^{39}Ar$ Thermochronology in Nepal 23
3.1 Overview 23
3.2 North West India 24
3.3 Far West Nepal 26
3.4 West-Central Nepal 27
3.5 Central Nepal 28
3.6 Eastern Nepal 29
3.7 Sikkim/Bhutan 30

Chapter 4 Results 32
4.1 Isotopic Analysis 32
KM 078 33
KM 074 41
KM 073 41
KM 068 41
KM 060 41
KM 054 42
KM 053A 42
KM 051B 42
KM 051A 43
KM031 43
KM030 43
KM 025A 44
KM 014 44
KM 013 44
LK 032 44
LK 039 45
LK 046 45
LK 048 45
LK 051 45
LK 052 46
LK 055 46
LK 059 46

Chapter 5 Excess Argon 47
5.1 The Himalayan Biotite Problem 47
5.2 Diffusion of Argon in mica 47
5.3 Mica Chemical Composition 49

Chapter 6 Discussion 537
6.1.1 The Mahabharat Range 53
6.1.2 The Lower HMC 55
6.1.3 The Upper HMC 56

6.2 Cooling History and Exhumation of the of the Khimti-Tamakoshi-Sindhuligadhi Region 57

6.3 Kinematic Model 59

Chapter 7 Conclusions and Future Work 64

7.1 Conclusions 64

7.2 Future Work 65

References 66

Appendices 84

Appendix A: Thermochronology data from different regions of Himalaya 84

Appendix B: Photomicrographs of specimen used for $^{40}Ar/^{39}Ar$ thermochronology analyses 103

Appendix C: Photographs of mica grains used for $^{40}Ar/^{39}Ar$ thermochronology Analyses 106

List of Tables

Table 4.1 Argon ages ……...…34
Table 5.1 Electron microprobe analysis of muscovite ….……...…50
Table 5.2 Electron microprobe analysis of biotite …...……...…51
Table A.1 Thermochronology of north-western India ……84
Table A.2 Thermochronology of far-western Nepal …….……...…….87
Table A.3 Thermochronology of west-central Nepal ……....…….88
Table A.4 Thermochronology of central Nepal …….……...93
Table A.5 Thermochronology of eastern Nepal …….…….…….96
Table A.6 Thermochronology of Sikkim-Bhutan …….…..…….100

List of Figures

Figure 1.1 Overview of Himalaya ……2
Figure 1.2 Geology of Himalaya ……...4
Figure 1.3 Different models for extrusion of Himalaya ...…….7
Figure 1.4 Hybrid model for extrusion of Himalaya ....…….8
Figure 1.5 Geological map of the study area ...……10
Figure 1.6 Geological cross-section of the study area ...……..……12
Figure 2.1 Decay scheme for ^{40}K ……..……...……15
Figure 2.2 Core of nuclear reactor at Oregon State University ……...17
Figure 2.3 Instrument setup for $^{40}Ar/^{39}Ar$ analysis at University of Manitoba ...…..……...17
Figure 2.4 An example of step-heat spectrum ……..……...19
Figure 2.5 An example of inverse Isochron diagram ……...20
Figure 3.1 Overview of past thermochronological studies …...……...25
Figure 4.1 $^{40}Ar/^{39}Ar$ age spectra ……...……...…35
Figure 4.2 $^{40}Ar/^{39}Ar$ age spectra ……...……...….36
Figure 4.3 $^{40}Ar/^{39}Ar$ age spectra ……...……...…37
Figure 4.4 Geological map of the study area showing $^{40}Ar/^{39}Ar$ age …...……...….38
Figure 4.5 Geological cross section showing $^{40}Ar/^{39}Ar$ age ……..…...……...….40
Figure 6.1 Spatial disrtribution of $^{40}Ar/^{39}Ar$ age ……...…...……...….54
Figure 6.2 Schematic kinematic model of evolution of the study area ....……...….60

Acknowledgements

I would like to express immense gratitude from the deepest corner of my heart to my supervisor Dr. Kyle P. Larson for his guidance, supervision, wisdom and patience, without whose support this projects would not have materialized. I would also like to thank the members of my committee Dr. John Greenough and Dr. Yuan Chen for their useful comments. Likewise, I thank all the staff at University of British Columbia, Okanagan, especially Janet Heisler, for their help and support.

I am grateful to everyone in the lab at FIP370A in UBCO (Sudip, Jaida, Shah, Asghar, Tyler, Heather, Alex and Iva) for their kind support, suggestions and insights throughout this project. I am especially thankful to Sudip for his constant companionship both in and out of the lab throughout my entire stay in Kelowna.

Many thanks to Dr. Alfredo Camacho for his invaluable suggestions and supervision for conducting $^{40}Ar^*/^{39}Ar$ dating and electron microprobe analyses at the University of Manitoba, Winnipeg. Thanks also to Laura Bergen and Ravinder Sidhu for helping with the analyses. I would like to appreciate Richard Fromage and Kana san for their hospitality during my stay in Winnipeg.

Thanks are owed to Bishow Silwal and Shiva Banskota for helping me out with the GIS map.

I would like to acknowledge the financial support from UBCO thorough the University Graduate Fellowships as well as various teaching assistanceships and research assistanceships throughout the duration of this project.

Finally, I thank my family for their everlasting affection and encouragement throughout my entire student life including this project. I am eternally grateful to my loving wife for enduring my virtual absence during some of her most difficult days and to my daughters for helping me keep my sanity during the most intense phases of this project. Without their support and love I couldn't have made it this far, they are the motivation that kept me going.

Chapter 1 Introduction

1.1 The Himalaya

The Himalaya-Karakoram-Tibet orogen is the manifestation of the collision between the Indian craton to the south and Eurasia to the north. It forms part of the greater Himalayan-Alpine system that extends from the Mediterranean Sea in the west to the Sumatra arc of Indonesia in the east over a distance of more than 7000 km (Gansser, 1964; LeFort, 1975; Yin and Harrison, 2000). The elevated southern front of the orogen forms the arcuate Himalayan mountain chain, which includes the highest topography on Earth, creating a physiographic divide between India and Eurasia (Fig. 1.1). The mountain chain, which trends generally E-W at its centre, becomes more N-S in orientation at its extremities before bending around syntaxial bends at Namche Barwa in the east and Nanga Parbat in the west (Fig. 1.1)

The Himalaya is an actively evolving mountain belt forming in response to the continued convergence between the Indian and Eurasian continental plates (Gansser, 1964; Le Fort, 1975; Schelling, 1992; Yin and Harrison, 2000). The initial collision took place ~59 million years ago with the final closure of the Tethys sea and underthrusting of the northern edge of India beneath the southern Eurasian margin (Patriat and Achache, 1984; Yin and Harrison, 2000; Hu et al., 2016). As the collision evolved, the dominantly sedimentary rocks deposited on the northern, former passive margin of the underriding Indian plate were scraped off by the overriding plate, variably metamorphosed, horizontally shortened and vertically thickened (Larson et al., 2010; Searle, 2006) giving rise to the Himalaya. This ongoing collision is the archetype for continent-continent orogens and as such, understanding the processes that have resulted in the evolution of the Himalaya can aid in our understanding of similar active and ancient orogens around the world (Gansser, 1964; Le Fort, 1975; Schelling, 1992; Upreti, 1999; Yin and Harrison, 2000, and references therein).

1.2 Geologic Background

At a broad scale, the Himalaya comprises four main lithotectonic units separated by large-scale, dominantly north-dipping fault systems that are more or less contiguous along the entire length of the orogen (Fig. 1.2; Le Fort, 1975; Upreti, 1999; Yin and Harrison, 2000).

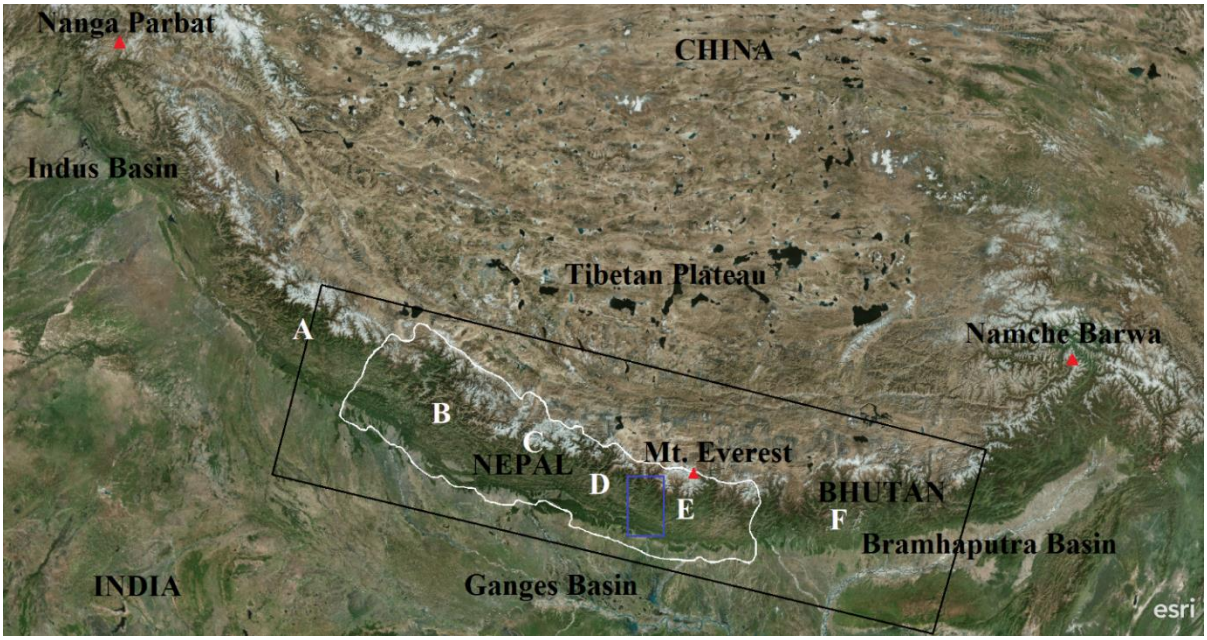

Figure 1.1. Overview of Himalaya. This map (Source: ESRI) shows the geographic location of the Himalayan arc that represents the physiographic boundary between India to the south and Eurasia to the north. Political boundary of Nepal is in white. Blue box represents the geographic location of the current study area that lies in east-central Nepal, just east of the centre of the Himalayan arc. The black box shows extent of the simplified geological map (Figure 1.2). A: North-western India, B: Far-western Nepal, C: West-central Nepal, D: Central Nepal, E: Eastern Nepal, F: Sikkim/Bhutan

From north to south these units include the Tethyan Sedimentary Sequence (TSS), Greater Himalayan Sequence (GHS), Lesser Himalayan Sequence (LHS) and Sub-Himalaya (SH) or Siwaliks (Fig. 1.2; Heim and Gansser; 1939; Le Fort, 1975; Gansser, 1981; Upreti, 1999; Yin and Harrison, 2000).

1.2.1 Tethys Sedimentary Sequence

The TSS comprises Neoproterozoic to Eocene sedimentary rocks deposited in the Tethys basin that separated the Indian and Eurasian plates prior to their collision (Garzanti et al., 1986; Vannay and Hodges, 1996; Hodges, 2000; Hu et al., 2016). The northern margin of the TSS is the Indus-Tsangpo Suture Zone (ITSZ) (Fig. 1.2; Allegre et al., 1984; Searle et al., 1987; Kellett et al., 2013; Yin and Harrison, 2000), which separates rocks of Indian affinity from those of Asian affinity. Its southern boundary is marked by a system of north-dipping, top-to-the-north-sense faults, the South Tibetan detachment system (Fig. 1.2; Burg et al., 1984; Burchfiel et al., 1992).

The basal-most portion of the unit is commonly metamorphosed at up to middle amphibolite facies and pervasively deformed due to motion along the South Tibetan detachment system. The severity of both metamorphism and deformation decreases rapidly structurally upwards, away from the shear zone, leaving the majority of the package virtually unmetamorphosed and affected by only upper crustal-style deformation.

1.2.2 Greater Himalayan Sequence

The GHS comprises the majority of the amphibolite to granulite facies metamorphic rocks exposed in the Himalaya. It occupies the footwall of the South Tibetan detachment system and is itself thrust over the subjacent LHS along the Main Central Thrust, a top-to-the-south sense ductile shear zone (Fig. 1.2; Gansser, 1964; Arita, 1983). Like the TSS, the GHS was sourced from dominantly sedimentary protoliths deposited on the northern Indian passive margin (Searle et al., 2008). Detrital zircon geochronology indicates a late Proterozoic to early Paleozoic protolith age (Parrish and Hodges, 1996; DeCelles et al., 2000).

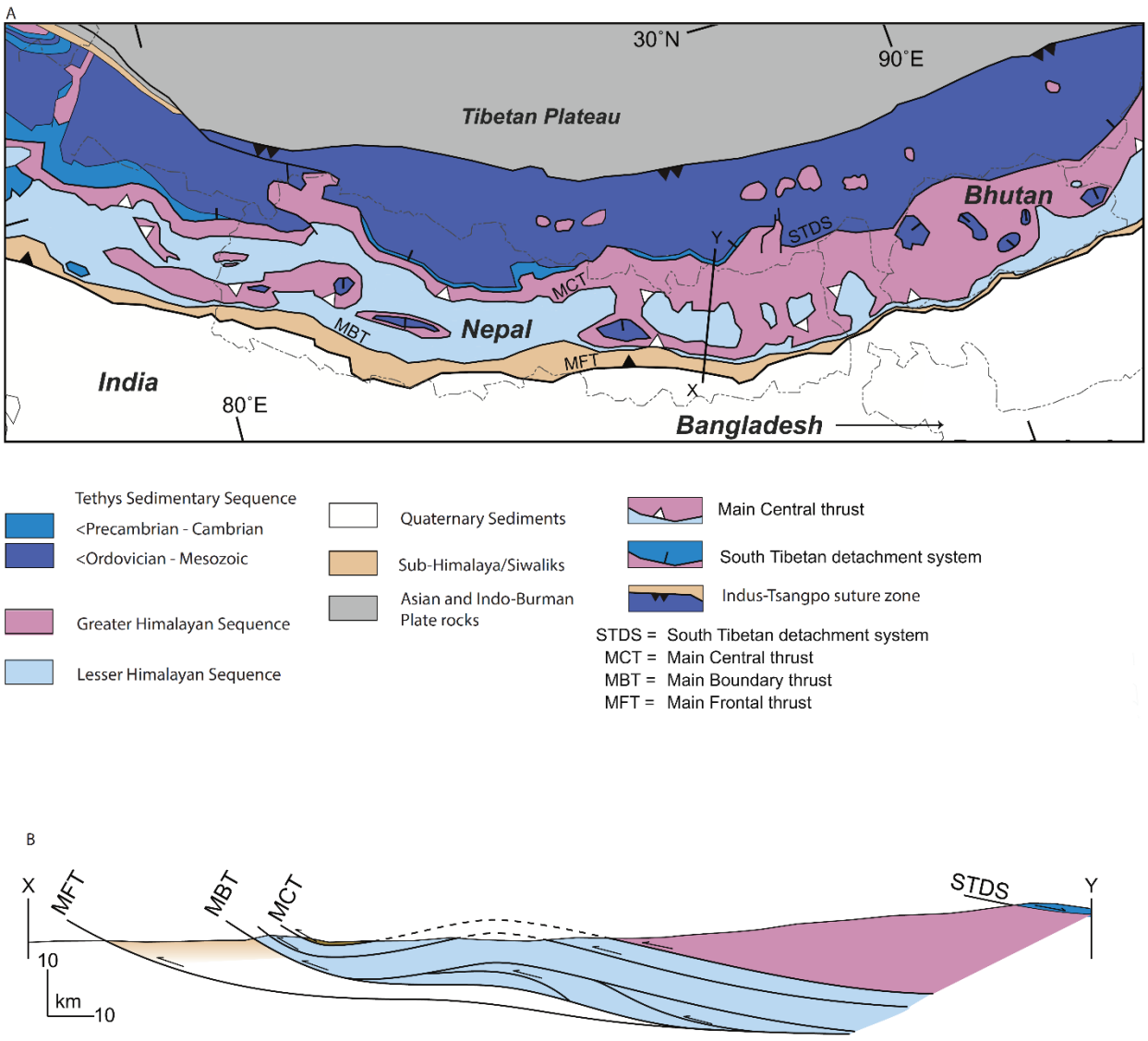

Figure 1.2. Geology of Himalaya. A. Simplified geological map of Himalaya after Cottle et al. (2015), He at al. (2015) and Webb et al. (2011). B. Schematic vertical geological section drawn across the east central Nepal Himalaya after Cottle et al. (2015)

The GHS represents the exhumed former midcrustal core of the orogen (Larson et al., 2010). It was extruded and at least partially exhumed from the mid-crust by coeval movement along the South Tibetan detachment system and the Main Central thrust during the early to middle Miocene. Though traditionally viewed as a single monotonous unit, recent work has shown that the GHS is actually an assemblage of discrete thrust sheets with distinct metamorphic and exhumation histories (Carosi et al., 2010; Larson et al., 2013; 2015; 2016; Montomoli et al., 2013; 2015; Larson and Cottle, 2014; Cottle et al., 2015).

1.2.3 Lesser Himalayan Sequence

The LHS is made up of sub-greenschist to lower amphibolite facies metasedimentary rocks that, like the GHS and TSS, are derived from protoliths deposited on the northern passive margin of the Indian plate (Searle et al., 2008; Sakai et al., 2013). The LHS is thrust over rocks of the subjacent SH along the Main Boundary Thrust (Fig. 1.2; Stocklin, 1980; Hubbard and Harrison, 1989). The base of the LHS has not been observed and as such its maximum thickness is unconstrained. The lowermost exposed sections of the LHS comprise phyllite, quartzite, and intercalated felsic igneous rocks. These igneous rocks yield Paleoproterozoic U-Pb zircon ages (ca. 1.7-1.9 Ga), which is consistent with detrital mineral geochronology from the phyllites and quartzites it is associated with (DeCelles et al., 2000; Kohn et al., 2010; Martin et al., 2011; Sakai et al., 2013). The middle portion of the LHS is more calcareous and locally contains stromatolites, though is otherwise unfossiliferous. Its age is estimated to be Mesoproterozoic to Paleozoic (Martin et al., 2011). The upper LHS extends from the late Paleozoic to the middle Mesozoic where rocks exposed at the very top of the sequence record a transition from marine to terrestrial environment (Sakai, 1983).

1.2.4 Sub-Himalaya

The SH also known as the Siwaliks is composed of sediments shed off of the developing Himalaya during the middle Miocene to early Pleistocene (Hubbard and Harrison, 1989) and deposited into the foreland basin. The evolving orogen and its encroachment into the foreland is reflected by a general upward coarsening of sediments and an increasingly proximal source through the sequence. The SH rides over recent foreland deposits along the active Main Frontal thrust (Fig. 1.2; Hubbard and Harrison, 1989).

1.3 Kinematic Evolution of the Himalaya

Of the four main fault systems bounding the lithotectonic units of Himalaya, three are thrust faults, the Main Frontal thrust, Main Boundary thrust, and Main Central thrust. They are interpreted to reflect the forward propagation of an orogenic wedge (Le Fort, 1975; Herman et al., 2008). The thrusts are interpreted to merge at depth into the Main Himalayan thrust, a north dipping décollement that extends at least 150 - 200 km to the north (Schelling and Arita, 1991; Bollinger et al., 2006; Wobus et al., 2008).

Until recently, discussions about the kinematic history of the Himalaya have typically revolved around a few major models: the Channel Flow model (Fig. 1.3A; e.g. Beaumont et al., 2001; 2004; Hodges, 2000; 2006; Godin et al., 2006; Searle et. al., 2006; 2008), the Critical/Wedge Taper model (Figure 1.3B; e.g. Bollinger et al., 2006; Kohn, 2008; Robinson et al., 2006) and, to a lesser degree, the Tectonic Wedging model (Fig. 1.3C; e.g. Webb et al., 2007; 2011; Webb, 2013; He et al., 2015; 2016). In the Channel Flow model (Fig. 1.3A), large-scale lateral mid-crustal flow accommodates a significant amount of the convergence in the orogen. The Critical/Wedge Taper model (Fig. 1.3B), in contrast, explains convergence accommodation and deformation in terms of an evolving accretionary wedge. Finally the Tectonic Wedging model (Fig. 1.3C) argues that the convergence is facilitated by insertion of a tectonic block (GHS in this case) between a floor thrust and roof back-thrust.

These models have previously been considered as mutually exclusive end members; however, more recently, researchers have proposed new alternatives that often incorporate aspects of two or more of these models (e.g. Beaumont and Jamieson., 2010; Larson et al., 2010; 2013; Larson and Cottle, 2014;). These ‘hybrid’ models (Fig. 1.4) generally propose that channel flow was active in the deep hinterland (mid-crustal levels), while wedge taper-controlled processes were active in the shallow foreland (upper crustal levels) simultaneously during the Miocene evolution of the mountain belt with some component of wedging as material migrated from the hinterland to the foreland.

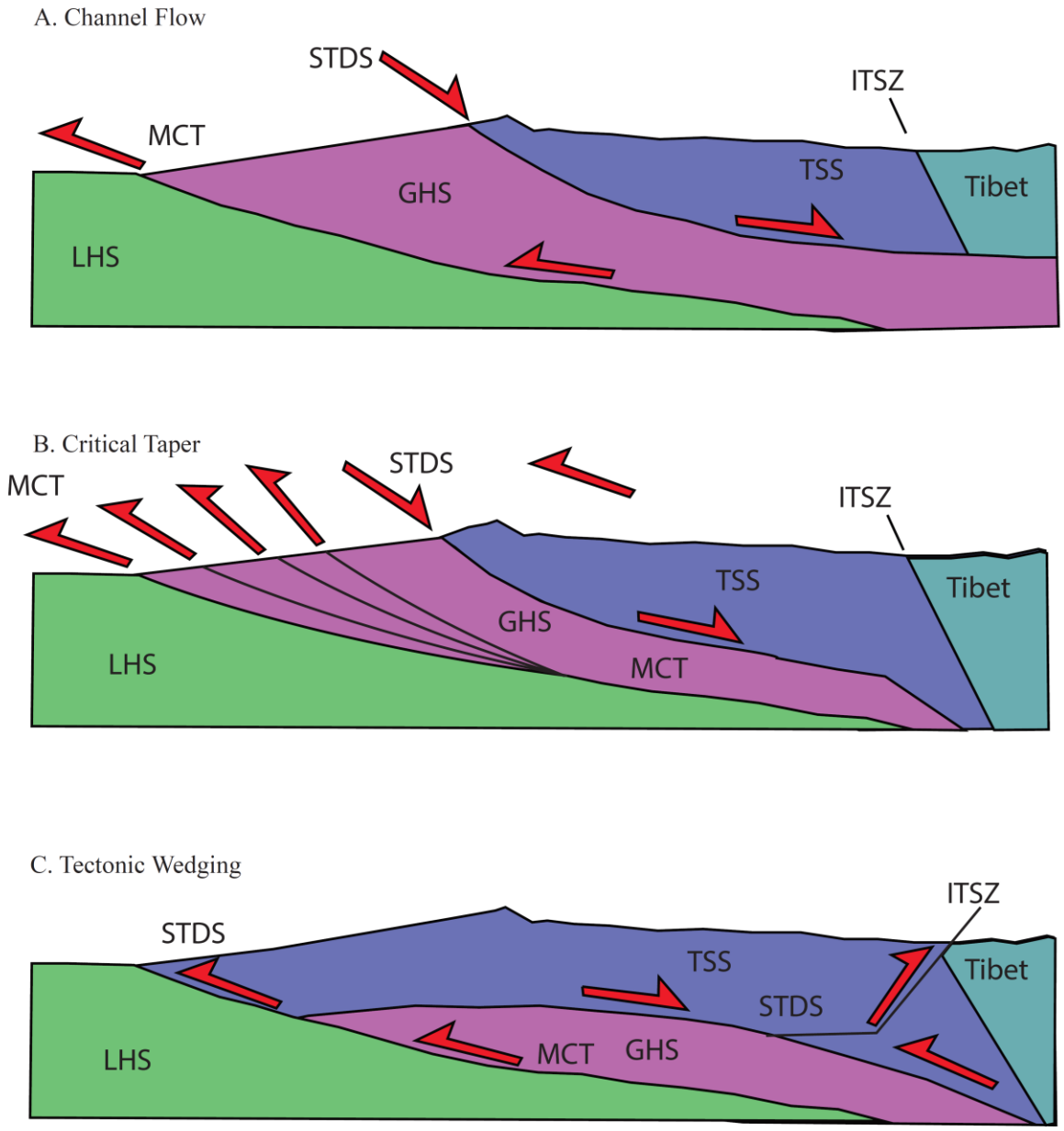

Figure 1.3. Different models for extrusion of Himalaya after Montomoli et al. (2013); Cottle et al. (2015).

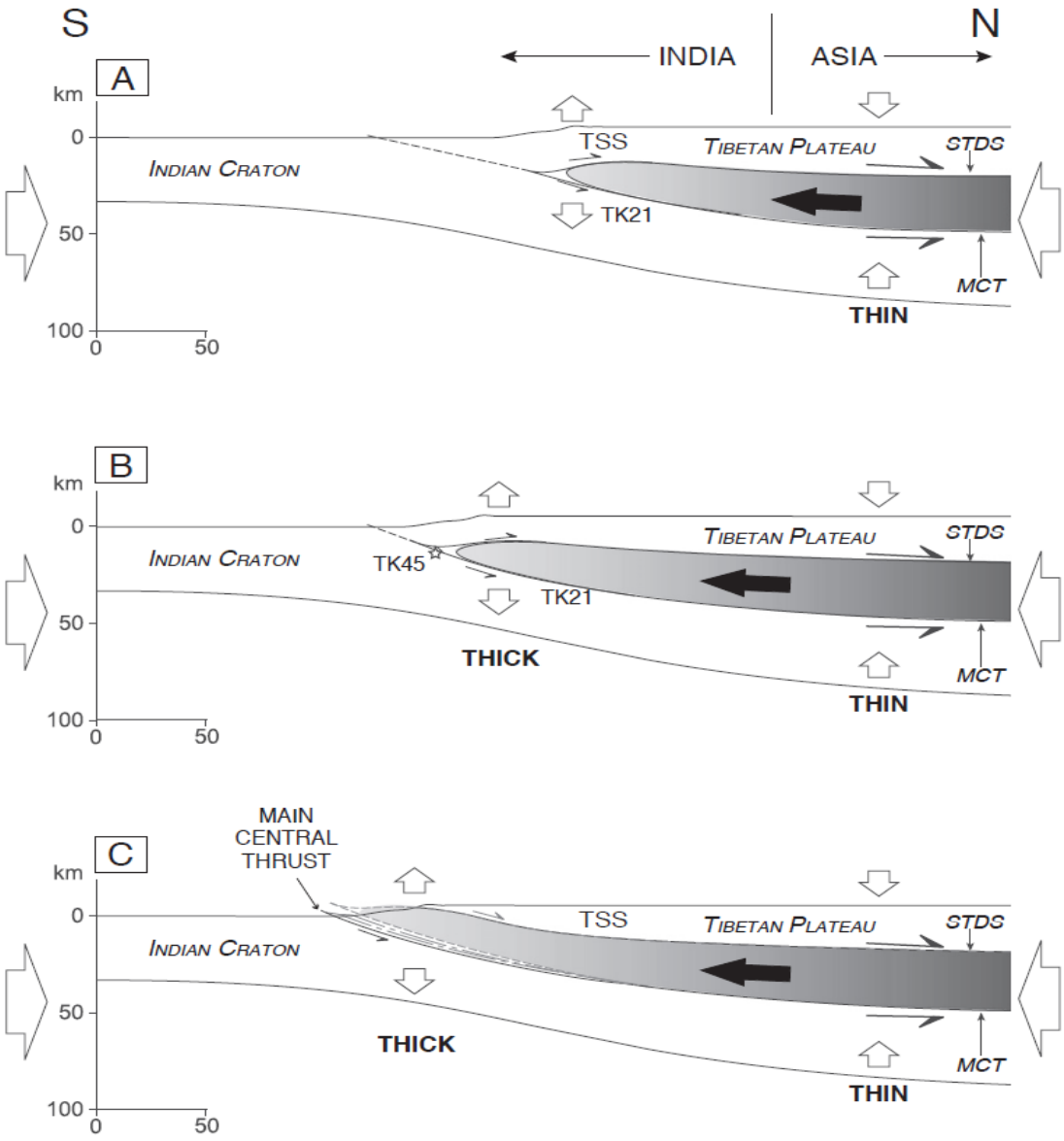

Figure 1.4. Hybrid model for extrusion of Himalaya, involving ductile deformation (channel flow) processes in the hinterland and brittle deformation (wedge tapering) process in the thinner foreland with tectonic wedging transporting material from one area to the other. (Larson et al., 2013).

1.4 Exhumation and Metamorphism

The GHS and LHS both contain rocks that represent the exhumed former mid-crust of the orogen. Collectively, these rocks, which are characterized by Cenozoic deformation, metamorphism, and cooling have been termed the Himalayan metamorphic core (HMC) (From et al., 2014; Larson and Cottle, 2014; Cottle et al., 2015). The HMC records an inverted metamorphic sequence with grade of metamorphism increasing from biotite grade at its base to sillimanite grade in the upper portion of the unit.

Geochronological studies implementing various methods have yielded constraints on the timing of metamorphism and deformation in the high-grade rocks of the middle and upper portions of the HMC, which outline a general decrease in metamorphic age towards lower structural levels and lower metamorphic grade (Hubbard and Harrison, 1989; Copeland et al., 1991; Macfarlane, 1995; Wobus et al., 2008). This has been variously interpreted as reflecting: 1) reactivated out-of-sequence brittle motion within the Main Central thrust zone (Macfarlane, 1993; Hodges et al., 2004) or 2) downward migration of strain and the development of the Lesser Himalayan duplex (Schelling and Arita, 1991; DeCelles et al., 2001; Robinson et al., 2003; Avouac, 2003; Bollinger et al., 2004; 2006).

Similarly, the cooling history of the HMC, derived from Rb-Sr, K-Ar and $^{40}Ar/^{39}Ar$ methods, shows a general younging from higher structural levels in the north to the lower structural levels farther south (Hubbard and Harrison, 1989; Copeland et al., 1991; Macfarlane, 1995; Edwards, 1995; Wobus et al., 2008). This has been related to late-stage hydrothermal activity within the Main Central thrust zone (Copeland et al., 1991) in the Pliocene or simply result of increased erosion in the south and recent exposure/cooling due to intensification of climatic factors (Wobus et al., 2008).

1.5 Current Study

The current study examines the thermochronology of a little-studied portion of the Himalaya in east central Nepal (Figs. 1.1; 1.5). The almost NE-SW traverse along the Tamakoshi and its tributary Khimti river valleys cuts across the general ESE-NNW strike of

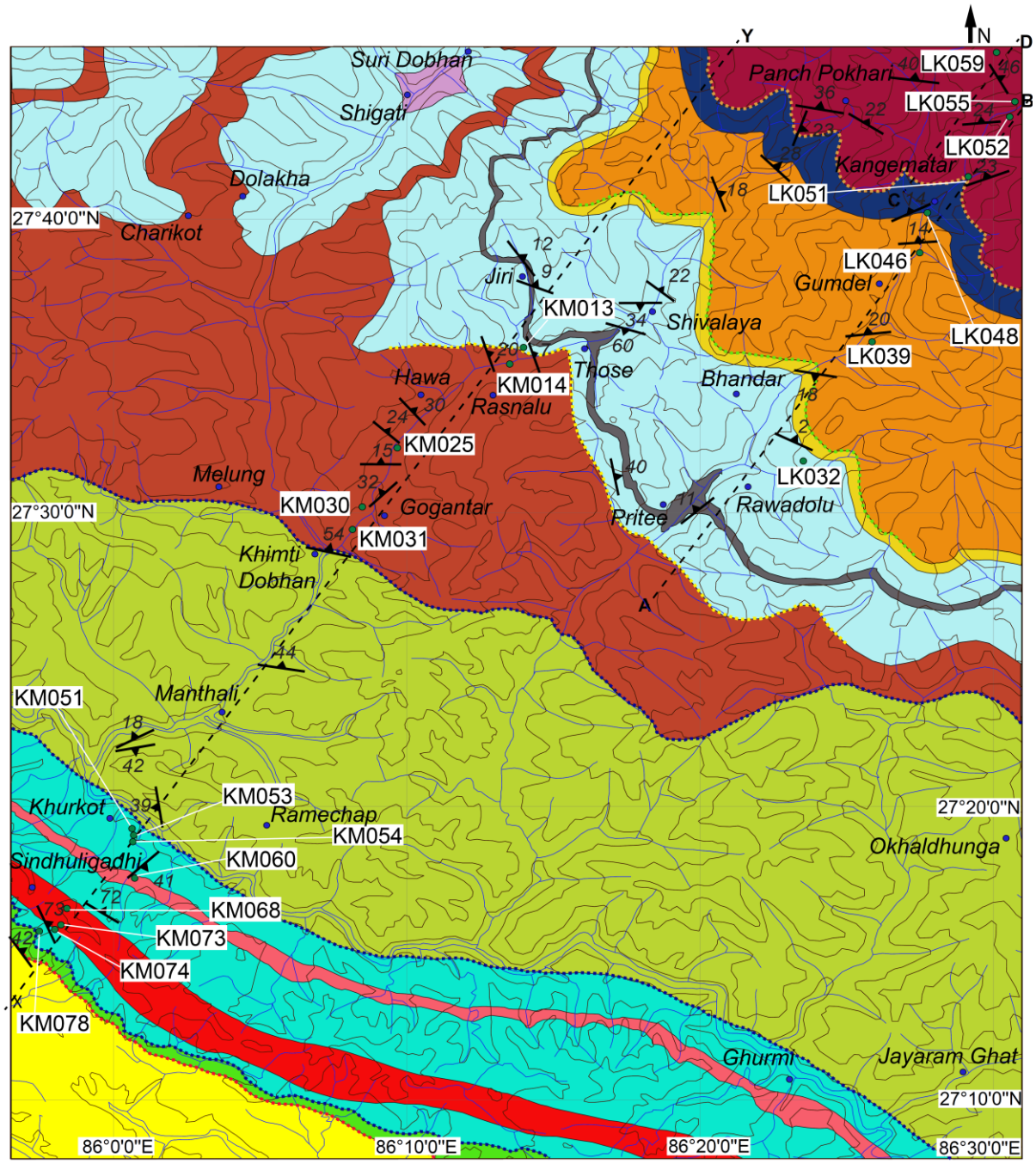

Figure 1.5. Geological map of the study area. Geological contacts incorporated from Ishida, 1969, Schelling, 1992, From and Larson (2014), Larson and Cottle (2014). The location of the study area is indicated in Fig. 1.1. (legends on next page)

Figure 1.5 continued

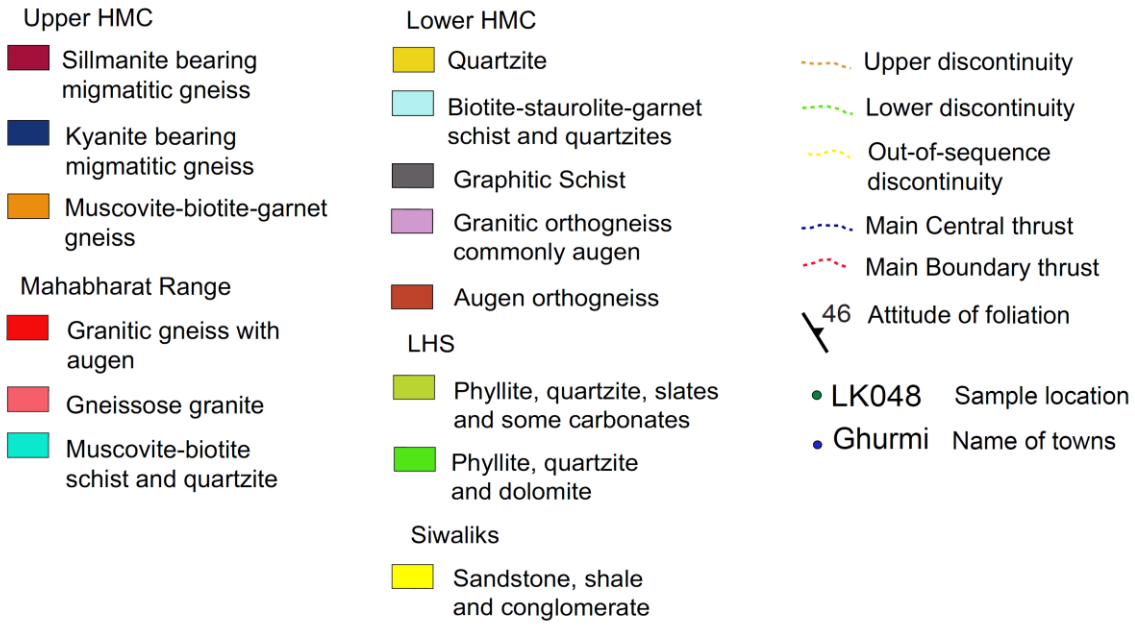

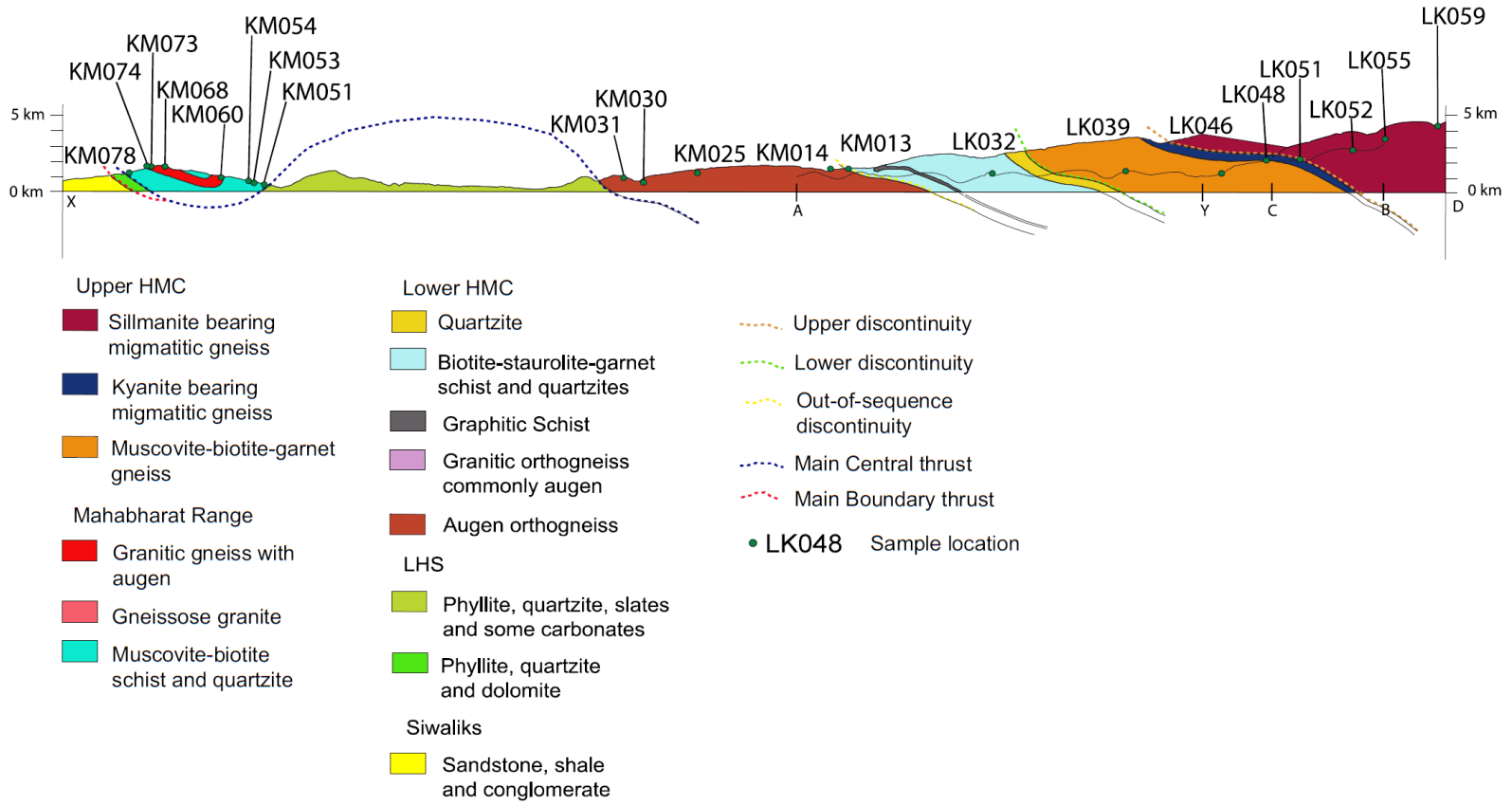

Figure 1.6. Geological cross-section of the study area. (Vertical = Horizontal)

the exhumed mid-crust and adjacent portions of the subjacent, low-grade to unmetamorphosed rocks of the LHS, creating an excellent vertical section through the regional geology (Fig. 1.6).

Regionally, the metamorphic rocks of the HMC occur as an extensive thrust sheet that underlays much of the study area while the subjacent LHS rocks are mainly exposed in an erosional window toward the southern half of the area (Figs. 1.5; 1.6). The leading edge of the thrust sheet is exposed at the southernmost part of the study area as a partial klippe, forming the Mahabharat Range (Figs. 1.5; 1.6).

The current study attempts to constrain the age of cooling and exhumation of the rocks in the area using $^{40}Ar^{*}/^{39}Ar$ (* stands for radiogenic fraction; see Chapter 2) analyses of biotite (Bt) and muscovite (Ms) mica, separated from specimens collected across the region. These ages are representative of the time when the specimen that was buried and heated during Himalayan orogenesis cooled through a certain temperature threshold during exhumation. The study of regional cooling histories assists in understanding the processes operating to bring the rocks to the surface and create its present-day geometry. Different processes will impart different spatial cooling age 'fingerprints' across an area. The findings of the current research will provide an important dataset where none currently exist, opening up an opportunity to better understand the late evolution this portion of the orogen. Moreover, the thermochronologic dataset generated will be used in conjunction with existing data to further understand the processes that have controlled the recent development of the Himalaya and perhaps the kinematic development of orogenic systems in general.

Chapter 2 Methods

1.2 $^{40}Ar^*/^{39}Ar$ Thermochronology Overview

^{40}K is a naturally occurring radioactive isotope of potassium with a half-life of 1250 Ma (McDougall and Harrison, 1999). The decay of ^{40}K is a branching process (Fig. 2.1). 10.48% of ^{40}K undergoes decay by electron capture (or positron emission) to produce ^{40}Ar while the remaining 89.52% decays into ^{40}Ca through negatron decay. This $^{40}K(n,p)^{40}Ar$ reaction is used as the basic principle for dating rocks and minerals by the $^{40}Ar^*/^{39}Ar$ method (Merrihue, 1965; Merrihue and Turner, 1966) and its predecessor K-Ar dating (Kelly, 2002; McDougall and Harrison, 2000). The $^{40}Ar^*/^{39}Ar$ method is essentially an improvement over the conventional K-Ar method (McDougall and Harrison, 1999). Unlike conventional K-Ar geochronology that relies upon the measurement of absolute concentrations of ^{40}K and ^{40}Ar to determine parent-daughter ratios while making age determinations, the $^{40}Ar^*/^{39}Ar$ method involves the measurement of the ratio of the two Ar isotopes, which is more accurate than absolute measurements. The method overcomes some of the limitations of the K-Ar method through the use of a single aliquot of sample for measurement of $^{40}Ar^*/^{39}Ar$ ratio, as opposed to two different aliquots in case of the latter, thus improving both accuracy and precision. Likewise the sample volume is significantly reduced in $^{40}Ar^*/^{39}Ar$ reducing potential sample heterogeneity.

The $^{40}Ar^*/^{39}Ar$ method makes use of the principle of artificially induced radioactive decay of another isotope of potassium, ^{39}K into an isotope of argon, ^{39}Ar, described by the reaction $^{39}K(n,p)^{39}Ar$, which is induced by the irradiation of a K-bearing specimen with thermal and fast neutrons in a nuclear reactor. The ^{39}Ar is an unstable isotope of argon with a half-life of just 269 years that undergoes negatron decay to produce ^{39}K. It does not exist in nature and is thus used in the $^{40}Ar^*/^{39}Ar$ method as the proxy for ^{40}K as the ratio of the potassium isotopes in nature is constant (Faure and Mensing, 2005).

Therefore, the ratio of $^{40}Ar^*/^{39}Ar$ is directly proportional to the age and determined using the relation:

$$t = \lambda \ln [1 + J (^{40}Ar^*/^{39}Ar)] \quad .. (i)$$

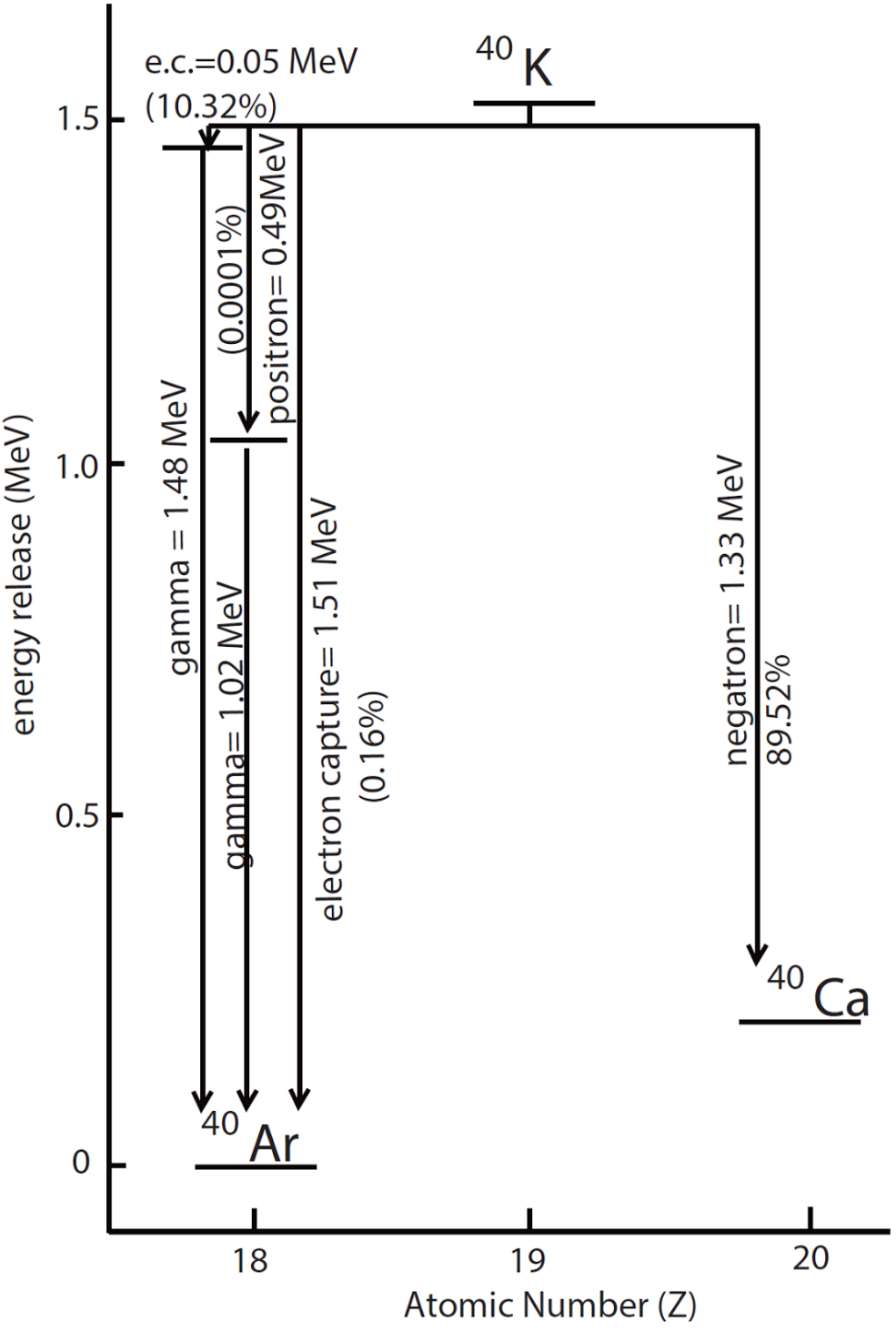

Figure 2.1. Decay scheme for ^{40}K, showing decay to ^{40}Ar and ^{40}Ca (after McDougall and Harrison, 1999).

Where:

t = age

J = dimensionless irradiation-related parameter

The dimensionless irradiation parameter J is introduced to relate the production of ^{39}Ar through the irradiation of ^{39}K by fast neutrons, which is a function of duration of irradiation, neutron flux and neutron capture cross-section of the specimen, parameters whose direct measurement is not practical. The problem is thus circumnavigated by the determination of the value of J by irradiating a mineral of known age, called the fluence monitor or flux monitor, along with the unknown specimen (McDougall and Harrison, 2000).

The $^{40}Ar^*/^{39}Ar$ method has been used to date a wide range of rocks and minerals of varying ages. It can be applied to not only potassium-rich minerals like biotite, muscovite, sanidine, but can be applied to also minerals that have relatively low potassium concentrations like hornblende, pyroxene, plagioclase, pyrite and magnetite, as well as clay minerals. Though it is possible to use this method to date, with fairly acceptable accuracy, samples as young as a few thousand years, there is practically no limit to applying this method to date old specimens (McDougall and Harrison, 2000). The scope of this dating method has been further enhanced by the advent of laser heating analysis and laser techniques for single spot investigation (Kelly, 2002b) and improvement in instrument precision that allow the dating of single crystals.

2.2 Procedure

The $^{40}Ar^*/^{39}Ar$ method can be utilized to date bulk rock samples, individual mineral separates or single grains. The material to be dated is first irradiated by fast neutrons inside a nuclear reactor (Fig. 2.2), along with strategically placed flux monitors to determine the degree of irradiation. The irradiated material is then heated using either the traditional furnace method or a laser (Fig. 2.3) to promote the diffusion of Ar out of its host crystal structure. The Ar released is sent over high vacuum to a mass spectrometer (Fig. 2.3) to determine the ratio of different isotopes of argon. Heating method can be either bulk heating until fusion, mostly used for bulk rock samples, or step heating where single or multiple crystals of a single specimen is/are heated in a series of steps with increasing temperature. Likewise, in the laser heating

Figure 2.2. Core of nuclear reactor at Oregon State University.
(http://radiationcenter.oregonstate.edu/content/irridiation-facility)

Figure 2.3. Instrument setup for $^{40}Ar^*/^{39}Ar$ analysis at University of Manitoba including Photon Machines CO2 laser, SAES getters, and Argus VI mass spectrometer.

method the specimen is heated using steps with increasing voltage, effectively increasing temperature in successive stages until the specimen is fused. Laser step heating has become the standard procedure for $^{40}Ar^*/^{39}Ar$ dating because of the excellent precision and sensitivity permitted by this method in dating selected mineral or rock grains (Faure and Mensing, 2005). Lasers can now also be used for in-situ targeting of specific domains in a mineral – though this is limited to a fusion age and restricted to older specimens that have accumulated measurable radiogenic daughter material.

2.3 Data Presentation and Analysis

The two most common ways to present step heating data are as an age spectrum (Fig. 2.4) or an age isochron (Fig. 2.5). Turner (1966) first proposed plotting the apparent age at each successive heating step against the cumulative ^{39}Ar released, as this isotope is representative of the total parent isotope involved. The resulting graphical representation, termed an age spectrum, is currently the standard way to present step heating data (Fig. 2.4).

The simplest age spectrum occurs when the material analyzed acts as a closed system and has experienced a fast cooling history, like a rapidly extruded volcanic rock. The step heating results in an essentially flat age spectrum with each step showing the same age, which approximates the crystallization age. This is said to define a 'plateau age'. Such simple cooling histories are generally the exception. When the material examined has undergone a prolonged cooling history or repeated heating and cooling episodes then the shape of age spectrum may change significantly to reflect that unique thermal history (McDougall and Harrison, 2000).

In the case of a complex age spectrum, a 'plateau age' can be determined by only using the steps that exhibit concordant ages, i.e. ages consistent within analytical errors, while discarding those that are discordant. Numerous different definitions of a plateau exist, however, all of them attempt to include the maximum number of concordant steps and to minimize variation between individual steps (McDougall and Harrison, 2000).

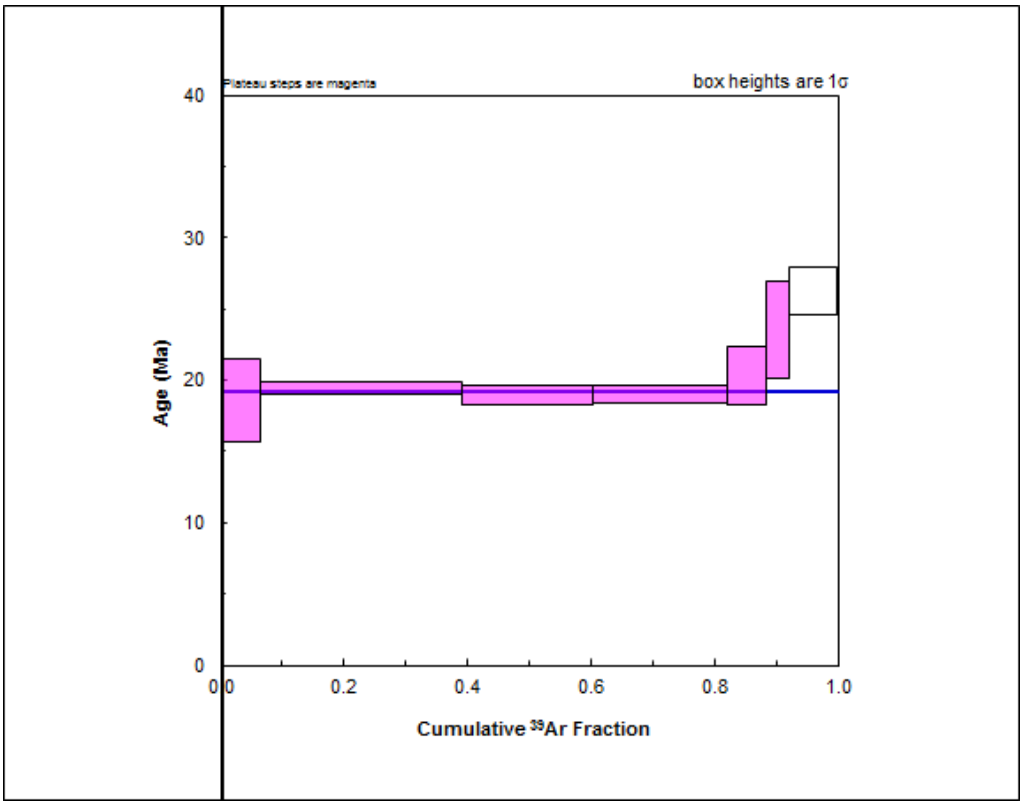

Figure 2.4. An example of step-heating spectrum. The pink boxes represent the plateau steps while the blue line represents the plateau age.

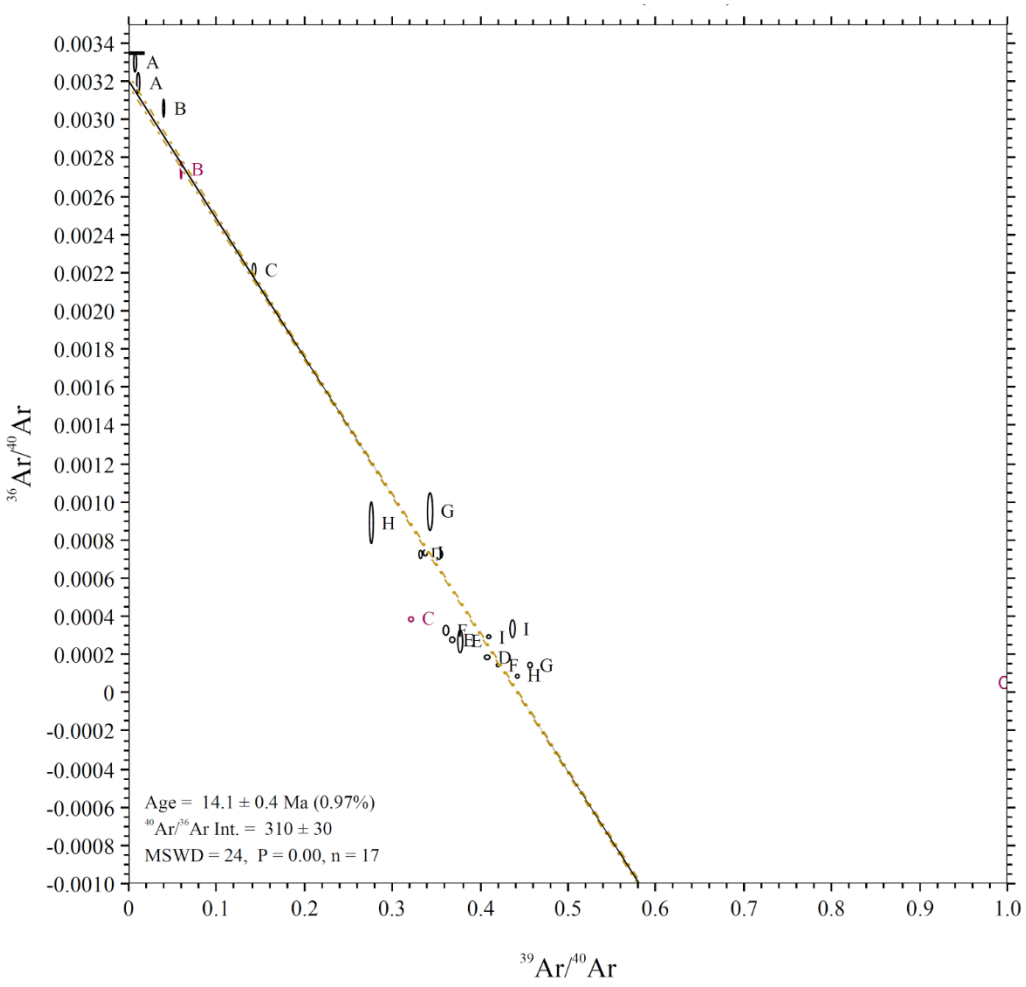

Figure 2.5. An example of inverse Isochron diagram. The labelled error ellipses account for errors in both x and y axes.

The component of a non-uniform age spectrum that is associated with atmospheric argon content before becoming a closed system can be deciphered by the use of an isochron (McDougall and Harrison, 2000). In an isochron plot, measured $^{36}Ar/^{40}Ar$ ratios from consecutive heating steps are shown along the y-axis versus $^{39}Ar/^{40}Ar$ ratios along the x-axis. Ideally, the plots define a straight line whose slope corresponds to the age of the specimen while the y-intercept gives the isotopic proportion of excess argon (defined in following section) of atmospheric origin present in the specimens initially (McDougall and Harrison, 2000).

2.4 Extraneous Argon

The interpretation of $^{40}Ar^*/^{39}Ar$ age data can be further complicated by the presence of extraneous argon, which can be incorporated into the specimen in various ways. Extraneous argon is the phenomenon when there is ^{40}Ar in a system that was not generated by in situ decay of potassium (Kelly, 2002a). There can be several different types and sources of extraneous argon. The term 'inherited argon' is used when there is contamination by older material or due to only partial resetting of minerals in metamorphic rocks (Kelly, 2002a). In those cases the source of the inherited argon is within the grain/system (Kelly, 2002a). However, $^{40}Ar^*$ may also exceed in situ production due to the introduction of 'excess argon' sourced from outside the system. 'Excess Argon' is defined as the parentless radiogenic argon introduced into a mineral during crystallization or by subsequent diffusion, or occluded within fluid or melt inclusions within the mineral (McDougall and Harrison, 2000; Kelly, 2002a).

Excess argon is not characteristically different from radiogenic argon and thus it is impossible to isolate and differentiate from measured results (Villa, 1990). This problem can be partially resolved through step heating and analysing partial plateau ages (Maluski et al., 1988). Potassium-bearing minerals with excess argon generally render a 'U-shaped' spectrum during step heating. It is so called because the initial low temperature steps often have older apparent ages followed by younger ages associated with the middle steps and finally older apparent ages for the final high temperature steps (Lanphere and Dalrymple, 1976). Because the older apparent ages are interpreted to reflect excess ^{40}Ar daughter isotopes, only the age of the saddle (partial plateau) is considered in final age calculation (Maluski et al., 1988).

Certain domains of mineral grains like grain boundaries, fractures, cleavage surfaces, or inclusions, etc. have higher potential to incorporate extraneous/excess argon that contributes to older ages during step heating. In situ laser ablation can be helpful in resolving the issue of excess argon (Kelly, 2002) as it can provide the spatial control to avoid potential problematic areas of grains. In addition, comparison of ages obtained from multiple geochronologic methods can be helpful in identifying excess argon in specimens that may not yield a 'U-shaped' spectrum but yield anomalously old ages.

2.5 Closure Temperature

A critical consideration in interpreting the age of a rock or mineral from the products of radiogenic decay is the system's 'closure temperature'. The term was introduced by Dodson (1973) as representing a point in time at which a completely mobile daughter product became completely immobile. The definition of closure temperature thus implies any 'apparent' age calculated is simply the time when the mineral cooled down through the closure temperature restricting migration of radiogenic daughter material out of the system (Kelly, 2002).

Chapter 3 $^{40}Ar^*/^{39}Ar$ Thermochronology in Nepal

3.1 Overview

Both K-Ar and $^{40}Ar^*/^{39}Ar$ thermochronology have been employed in the Nepal Himalaya in an attempt to understand the low temperature evolution of the orogen with varying degree of success. In an active, hot orogen like the Himalaya the dates derived from the $^{40}Ar^*/^{39}Ar$ method are typically viewed as a cooling ages and not the crystallization age of the specimen. Although, most potassium-bearing minerals (e.g. muscovite, biotite, hornblende, K-feldspar) have been utilized for studies in the Himalaya, muscovite ages have proven the most reliable (e.g. McFarlane, 1993; Copeland et al., 1991; Herman et al., 2010; Stübner et al., 2016). In regionally metamorphosed terrains, muscovite $^{40}Ar^*/^{39}Ar$ ages typically represent the time at which specimens cooled through approximately 350 - 430 °C; its closure to radiogenic Ar diffusion out of the crystal (Huntington et al., 2006).

The abundance of muscovite $^{40}Ar^*/^{39}Ar$ dates from the Himalaya and emphasis on them for interpretations reflects both its presence as a commonly occurring mineral and apparent anomalies observed in many of the biotite ages from across the region (McFarlane, 1993; Herman et al., 2008; 2010; Stübner et al., 2016). Published biotite ages are commonly older than muscovite ages for the same locations despite having a lower theoretical closure temperature (Copeland et al., 1991; Hubbard and Harrison, 1998; Maluski et al., 1988; Macfarlane, 1993; Huntington et al., 2006; Bollinger and Janots, 2006; Herman et al., 2008; Stübner et al., 2016). This is generally regarded as reflecting an excess Ar component in the biotite (Kelly, 2002; Stübner et al., 2016) or homogenization of Ar in biotite (and not in muscovite) during incremental heating (McDougall and Harrison, 1988), implying that such biotite ages have no geological significance (Copeland et al., 1991; Herman et al., 2010). There are alternative interpretations for some of the discrepancies, however, including late muscovite (re)crystallization in fluid-rich shear zones. This may be plausible locally, as suggested by the textural relationship between the two minerals in specimens collected (e.g. Herman et al., 2010), but cannot explain the broader regional-scale pattern.

A general trend of cooling ages younging structurally down-section towards the Main Central thrust is observed in published thermochronologic data from the GHS (Hubbard and Harrison, 1989; Copeland et al., 1991; Macfarlane, 1995; Theide et al., 2005; Wobus et al., 2008). $^{40}Ar^*/^{39}Ar$ cooling ages as young as the Late Pliocene (~2–3 Ma) have been documented from within the Main Central thrust zone near the Marsyangdi valley (Edwards, 1995), and in the Langtang valley (Macfarlane, 1993). Young $^{40}Ar^*/^{39}Ar$ cooling ages such as these are variously interpreted as: 1) reflecting out-of-sequence brittle motion within the Main Central thrust zone (Macfarlane, 1993; Hodges et al., 2004); 2) recent exhumation over a mid-crustal ramp (Gansser, 1964; Cattin and Avouac, 2000; Lave and Avouac, 2001); 3) cooling related to development of a duplex in the underlying LHS (Schelling and Arita, 1991; DeCelles et al., 2001; Robinson et al., 2003; Avouac, 2003; Bollinger et al., 2004; 2006); 4) late-stage hydrothermal activity within the Main Central thrust zone (Copeland et al., 1991) in the Pliocene; or 5) simply result of increased erosion and recent exposure due to intensification of climatic factors (Theide et al., 2005; Wobus et al., 2008).

$^{40}Ar^*/^{39}Ar$ thermochronology alone is often not sufficient to understand a complex orogen like Himalaya as only information regarding the low temperature thermal history can be derived. Therefore, it is best interpreted in the context of existing structural, petrographic, metamorphic, kinematic, and geochronologic data. Below, existing $^{40}Ar^*/^{39}Ar$ data and interpretations from across the Himalaya are summarized from west to east.

3.2 North West India

Muscovite and biotite $^{40}Ar^*/^{39}Ar$ ages of ~20 Ma were reported by Walker et al. (1999) (Appendix A) from the top of the GHS in the Zanskar-Lahaul section of North Western India (Fig. 3.1). A similar 20 Ma Muscovite age was obtained from anatectic leucogranite, which, when compared with a 21 – 22 Ma U-Pb crystallization age, indicates fast cooling of the top of GHS due to rapid unroofing during displacement across the overlying South Tibetan detachment system (Walker et al., 1999). Muscovite ages obtained from the middle and lower portions of GHS in the region are slightly older at ca 22. Ma, indicating post-peak metamorphic exhumation in the Miocene.

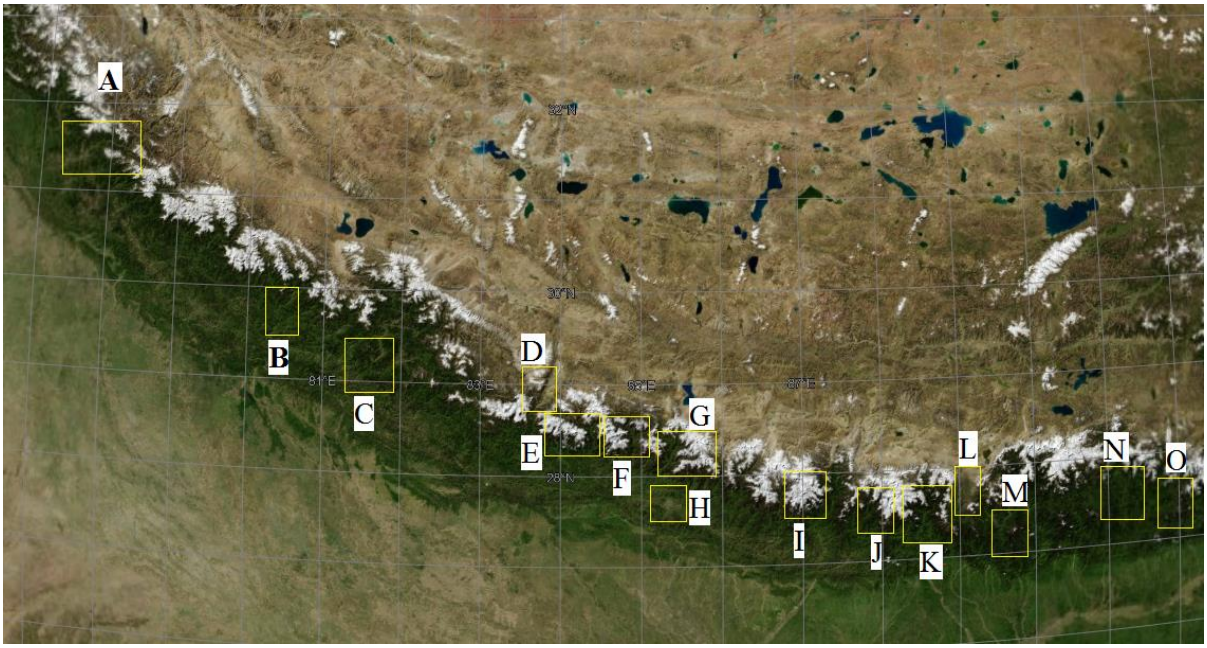

Figure 3.1. Overview of past thermochronological studies. This map (Source ESRI) shows the various sections in Himalaya where $^{40}Ar/^{39}Ar$ or K-Ar thermochronological studies have been conducted. A: Sutlej section, B: Mahakali section including Sirdang window and Askot-Chiplakot window, C: Karnali and Jumla-Surkhet section including Karnali klippe, D: Kaligandaki section, E: Annapurna section including Darondi-Marsyangdi sections, F: Manaslu section with Burhi-Gandaki section, G: Langtang section, H: Kathmandu section including Kathmandu synclinorium, I: Everest section, J: Taplejung section, K: Northern Sikkim, L: Yadong section, M: Wang Chu section, N: Kuru Chu section, O: Tashigang section.

In the Sutlej section of North Western India (Fig. 3.1) analysis of rocks from the TSS yielded muscovite ages ranging from 17 Ma to 19 Ma (Theide et al., 2005) (Appendix A) while Muscovite from the GHS ranges in age from 15 Ma to 18 Ma (Theide et al., 2005; Vannay et al., 2004). Very young muscovite ages, ca. 4.4.Ma, occur in the LHS in the valley bottom in the immediate footwall of the Main Central Thrust, which may indicate rapid uplift possibly aided by focused erosion by the Sutlej River intensified due to onset of the monsoon system (Theide et al., 2005). Slightly older Muscovite ages of up to 6 Ma near the ridges away from valley bottom further support this interpretation.

3.3 Far West Nepal

Because of its remoteness and general lack of accessibility, only a limited number of studies have been carried out in the westernmost part of Nepal (Fig. 3.1). The geology of Far West Nepal is characterized by various isolated klippen of GHS material (Fig. 1.2). These are viewed as erosional remnants of one large overthrust sheet of the GHS that has been cut through forming windows that expose the underlying LHS (Bollinger and Janots, 2006; Sakai et al., 2013).

LeFort (1987) reported K-Ar ages of GHS leucogranite bodies from West Nepal (Fig. 1.1) as well as farther west in India (Appendix A). These leucogranite K-Ar ages range from 15 to 36 Ma indicating peak temperature metamorphism and partial melting in the GHS predates at least 15 Ma.

In the Mahakali region of Far West Nepal (Fig. 3.1), LHS rocks exposed in the northern Sirdang window consistently yield $^{40}Ar^*/^{39}Ar$ ages below 12.5 Ma, while those in the Askot-Chiplakot window to the south yield ages in excess of 16 Ma reaching up to 24 Ma in the core of the window (Bollinger and Janots, 2006). Those late Miocene ages from the LHS (Bollinger et al., 2003) (Appendix A) are interpreted to reflect exhumation following cessation of movement along Main Central Thrust and southward progression of brittle movement towards the Main Boundary Thrust.

An upper GHS specimen obtained from the base of southern limb of the Karnali Klippe (Fig. 3.1) yielded a biotite plateau age of ~26 Ma (Sakai et al., 1999; 2013b). This is consistent with the leading edge of GHS cooling through biotite closure early during Miocene thrusting along the Main Central thrust. In the Jumla-Surkhet area farther north (Fig. 3.1), a two-mica garnet schist at the top of the Main Central thrust zone yields a muscovite $^{40}Ar^*/^{39}Ar$ age of ~20 Ma (Sakai et al., 1999; 2013b). That is consistent with a 16-17 Ma minimum age derived from the staircase age spectrum of muscovite obtained from the Early Miocene Dumri Formation of the LHS in the same area. The Dumri Formation exhibits inverted metamorphism in its topmost part while maintaining lithostratigraphic continuity (Sakai et al., 1999; 2013b). The inverted metamorphism is interpreted to reflect heating by overriding, hot GHS rocks partially resetting the muscovite $^{40}Ar^*/^{39}Ar$ system (Sakai et al., 2013b).

3.4 West-Central Nepal

In the Kaligandaki Valley of West-Central Nepal (Fig. 3.1), muscovite from metamorphosed rocks in the immediate hanging wall of the South Tibetan detachment system yield $^{40}Ar^*/^{39}Ar$ ages ranging from 11 - 13 Ma (Godin et al., 2001; Vannay and Hodges, 1996) (Appendix A). This may be associated with a hydrothermal alteration during late South Tibetan detachment system reactivation or subsequent Thak Khola graben normal faulting (Hurtado and Hodges, 1998; Godin et al., 2001). Muscovite $^{40}Ar^*/^{39}Ar$ ages ranging from 13 - 15 Ma in the South Tibetan detachment system footwall (Appendix A) are interpreted as uniform cooling through the muscovite cooling isotherm during exhumation without any later thermal perturbation (Godin et al., 2001, Searle and Godin, 2003). Finally, a specimen obtained from the basal portion of TSS yielded an 18 Ma $^{40}Ar^*/^{39}Ar$ muscovite age (Appendix A), which Godin et al. (2001) cautiously suggest may be the maximum age of South Tibetan detachment system movement in the region.

Coleman and Hodges (1997) obtained biotite $^{40}Ar^*/^{39}Ar$ ages ranging from 14 - 16 Ma in the GHS (Appendix A) in the immediate footwall of the South Tibetan detachment system in the Marsyangdi valley (Fig. 3.1) indicating middle Miocene cooling. A 35.28 Ma hornblende $^{40}Ar^*/^{39}Ar$ age, from a similar location in the immediate footwall of the detachment system may constrain the youngest limit of peak metamorphism prior to exhumation. In the lower

parts of the GHS in the same region, muscovite $^{40}Ar^*/^{39}Ar$ ages systematically decrease from 5.1 to 2.46 Ma structurally downwards (Huntington et al., 2006; Huntington and Hodges, 2006) (Appendix A).

Similar late Miocene to Pliocene ages were also reported from muscovite of the GHS in the Marsyangdi and Darondi valleys (Fig. 3.1) by Catlos et al. (2001) (Appendix A). These ages have interpreted as recording Pliocene thrust-sense motion in the vicinity of the Main Central thrust possibly accompanied by rapid exhumation. Alternatively, this may indicate an increase in erosion rate possibly assisted by intensification of paleoclimatic conditions as early as late Pliocene (Wobus et al., 2008). Similar young $^{40}Ar^*/^{39}Ar$ ages in the Burhi Gandaki area (Fig. 3.1) were interpreted by Copeland et al. (1991) as a manifestation of a late stage thermal perturbation caused by rising hydrothermal fluids along brittle structures above the Main Central thrust.

The minimum age of the South Tibetan detachment system in West-Central Nepal (Fig. 1.1) is interpreted to be 22 - 23 Ma (Guillot et al., 1994) as constrained by a 22.8 Ma isochron age determined for a hornblende specimen from the interpreted contact aureole of Manaslu Granite (Fig. 3.1) (Appendix A) that is mapped to crosscut the fault system. Mica from the GHS in the same region yield 17.6 - 18.5 Ma $^{40}Ar^*/^{39}Ar$ ages (Guillot et al., 1994), consistent with 16.5 - 18.4 Ma ages reported by Copeland (1990) (Appendix A). Guillot et al. (1994) interpreted this as indicative of rapid cooling through the mica closure isotherm brought about by unroofing associated with the movement along the detachment system. This interpretation, however, is contested by Searle and Godin (2003) who use U-Pb geochronology and alternate map interpretations to argue for ductile shearing along Main Central thrust before 21 Ma followed by brittle faulting along South Tibetan detachment system after 19-18 Ma post-dating the Manaslu pluton.

3.5 Central Nepal

The areas around the Kathmandu Synclinorium and the Langtang valley of Central Nepal (Fig. 3.1) are some of the most intensely studied in Nepal reflecting their relative ease of accessibility. Oligocene hornblende cooling ages (Macfarlane, 1993) (Appendix A) in the

GHS constrain the end of peak T metamorphism while late Miocene muscovite cooling ages from the same rocks (Macfarlane, 1993) (Appendix A) are interpreted to reflect cooling associated with the movement along Main Central thrust.

Similar to those in West-Central Nepal, mica cooling ages in the Langtang region (Fig. 3.1) young towards lower structural levels within the GHS (Appendix A) consistent with slow cooling in the Early Miocene that accelerated five-fold around ~10 Ma, coincident with initiation of movement along the Main Boundary Thrust (Wobus et al., 2008).

Muscovite and biotite $^{40}Ar^*/^{39}Ar$ dates from around the Kathmandu Synclinorium (Fig. 3.1) were incorporated into thermokinematic modelling by Herman et al. (2008) that revealed the validity of both duplexing and out-of-sequence thrusting models to potentially explain the kinematics of crustal shortening across the Himalaya. Early Miocene mica cooling ages obtained from crystalline rocks and associated leucogranites in the southern limb of the Kathmandu Synclinorium (Arita et al., 1997) (Appendix A) are also consistent with the distal (southern) exposures of the GHS being overthrust horizontally post early Miocene exhumation.

3.6 Eastern Nepal

In eastern Nepal (Fig. 1.1), mica (Villa, 1990) and hornblende cooling ages (Villa and Lombardo, 1986) from Greater Himalayan Sequence rocks along the Lhotse-Nup Glacier in the Everest region (Fig. 3.1) constrain the timing of leucogranite intrusion there to between 17 - 15 Ma (Appendix A). This overlaps with the ~16.5 Ma muscovite and biotite cooling ages obtained from the nearby Rongbok Granite (Hodges et al., 1998) (Appendix A) where it is interpreted to constrain the minimum age of brittle movement along the Qomolangma detachment, a section of the South Tibetan detachment system, while a ~20 Ma hornblende cooling age constrains the maximum age limit (Hodges et al., 1998).

Similar ages have been derived elsewhere in the Everest region (Fig. 3.1). Early Oligocene hornblende $^{40}Ar^*/^{39}Ar$ ages (Hubbard and Harrison, 1989; Copeland et al., 1987), Middle Miocene mica $^{40}Ar^*/^{39}Ar$ ages and comparable K-Ar dates (Krummenacher et al., 1978) are characteristic of the metapelites and leucogranites in the upper and middle portions

of the GHS (Appendix A). Mica ages young down structural section to late Miocene in the lower portion of the GHS and within the Main Central thrust zone (Hubbard and Harrison, 1989; Copeland et al., 1987; Krummenacher et al., 1978) (Appendix A).

In contrast to much of the rest of GHS muscovite ages from the Himalaya, those in the Taplejung region of Far Eastern Nepal (Fig. 3.1) young upward structurally from 13.78 to 10.98 Ma (Sakai et al., 2013) (Appendix A), while a ~9 Ma K-Ar biotite date was obtained from an even higher structural levels of GHS (Imayama et al., 2012). In the underlying LHS, $^{40}Ar^*/^{39}Ar$ muscovite ages range from ~1.6-1.7 Ga indicating that these rocks did not experience a thermal event significant enough to reset the muscovite $^{40}Ar^*/^{39}Ar$ system since the Proterozoic.

3.7 Sikkim/Bhutan

Muscovite $^{40}Ar^*/^{39}Ar$ ages obtained from leucogranites and leucosomes in the footwall of South Tibetan detachment system in Northern Sikkim (Fig. 3.1) range from 12 – 13.5 Ma (Kellett et al., 2013) (Appendix A). When paired with the youngest monazite Th-Pb ages of 14.5 from the same rocks (Kellett et al., 2013), this indicates rapid post-peak metamorphism exhumation of the GHS likely facilitated by movement along the South Tibetan detachment system.

A multi-chronometer study by Gong et al. (2011) in the Yadong section (Fig. 3.1) in Southern Tibet, east of North East Sikkim, reported a biotite $^{40}Ar^*/^{39}Ar$ age of 48.5 Ma and a hornblende $^{40}Ar^*/^{39}Ar$ age of 31.8 Ma (Gong, 2006; Gong et al., 2011) (Appendix A) in high-pressure granulite. The data was interpreted as indicating a peak metamorphism of GHS older than 48.5 Ma and a rapid uplift to mid-crustal depth by 31.8 Ma. However, the generally dubious nature of biotite $^{40}Ar^*/^{39}Ar$ age throughout the Himalaya renders the first part of the interpretation questionable. A 13.9 Ma muscovite age and ~ 11.0 - 11.5 Ma biotite ages obtained from GHS in the southern part of Yadong section was taken to be indicative of mid-late Miocene cooling/exhumation, consistent with interpretation of Kellett et al. (2013) immediately to the east.

LHS rocks in southern Sikkim and Bhutan (Figs. 3.1) have been interpreted to comprise multiple imbricate thrust sheets (McQuarrie et al., 2008; 2014; Long et al., 2011; 2012). Muscovite ages obtained from the Wang Chu section (Fig. 3.1) in Western Bhutan range from 10.6 – 11.7 Ma, with a peak at 11.5 Ma (McQuarrie et al., 2014) (Appendix A) suggesting that the GHS cooled below muscovite closure to Ar diffusion by ca. 11.5 Ma.

Farther to the east, $^{40}Ar^*/^{39}Ar$ data from the northernmost LHS thrust sheets in the Kuru Chu section (Fig. 3.1) of eastern Bhutan, in the immediate footwall of the Main Central thrust, reveal muscovite ages that increase from 8.4 Ma to 12.9 Ma from north to south, or down structural section (Long et al., 2012) (Appendix A). Muscovite ages of approximately 1.3 Ga, obtained from the southernmost portion of LHS in the vicinity of Main Boundary Thrust, are thought to reflect a detrital age, generally free of thermal perturbation (Long et al., 2012).

North of the Main Central thrust along the Tashigang section (Fig. 3.1) east of the Kuru Chu valley in Bhutan, muscovite $^{40}Ar^*/^{39}Ar$ ages range from ~11 Ma in the immediate hanging wall to ~ 14 Ma at higher structural levels (Stüwe and Foster, 2001) (Appendix A). Similarly, an 11.7 Ma muscovite age was reported by Kellett et al. (2009) in the GHS west of the Kuru Chu valley. Repetition of the 11 Ma and 14 Ma muscovite ages at higher structural levels in Tashigang section may indicate a thrust sense discontinuity within the GHS (Stüwe and Foster, 2001).

Chapter 4 Results

There have been only a handful of geochronological studies conducted in the East-Central Nepal and none in the field area for this work. The results obtained from the current study will significantly augment the body of thermochronologic data from across the orogen and will help facilitate our understanding of the thermal and late-stage kinematic evolution of the Himalaya.

All the $^{40}Ar^*/^{39}Ar$ dates in this study come from the HMC including the crystalline rocks of the Mahabharat range (Figs. 4.4; 4.5). The LHS rocks in the Main Central thrust footwall did not contain muscovite or biotite crystals large enough to extract and thus were not be dated.

4.1 Isotopic Analysis

The current study uses isolated separates of muscovite and biotite for $^{40}Ar^*/^{39}Ar$ dating. Separates of pure minerals were isolated from the rock specimen by crushing and/or hand picking under stereoscopic microscope. These were then placed in 2 mm deep wells in 18 mm diameter aluminium disks along with strategically placed flux monitors to evaluate the lateral neutron flux gradients across the disk. The flux monitor used was Fish Canyon Tuff Sanidine (28.2 Ma; Kuiper et al., 2008). The samples were then irradiated inside the core of TRIGA reactor (Fig. 2.2) at the Cadmium-Lined in-Core Irradiation Tube (CLICIT) facility of Oregon State University, US. Planar regressions were fit to the standard data to measure the neutron flux parameter, J, from the unknown. The uncertainties in J are estimated at 0.1 - 0.2% (1σ), based on Monte Carlo error analysis of the planar regressions (Best et al., 1995).

The irradiated specimens were analysed at the $^{40}Ar^*/^{39}Ar$ laboratory in the University of Manitoba, Winnipeg. Single crystals of the mineral specimen were placed in a 133 pit copper sample holder and step heated, each step of 70 seconds duration, using a Photon Machines CO_2 Fusion Diode Laser (Fig. 2.3). The vapour generated was passed through three GP-50 SAES getters (two at room temperature and one at 450 °C) for three minutes to filter out reactive gases. Pure argon gas was then passed through a multi-collector Thermo Fisher Scientific

ARGUS VI mass spectrometer (Fig. 2.3) to measure the five Ar isotopes simultaneously. Each run including laser heating, getters and mass spectrometer lasted for about 21 minutes. All the measured isotopes were corrected for extraction-line blanks, conducting one 15 minute blank run after each three step heating runs. Atmospheric $^{40}Ar/^{36}Ar$ ratio of 295.5 (Steiger and Jaëger, 1977) was used for routine measurement of mass spectrometer discrimination using air aliquots, running one 30 minute air aliquot after each three blank runs. Likewise, each run, be it step heat, blank or air run, was followed by 600 seconds delay. Corrections were also made for neutron-induced ^{40}Ar from potassium, ^{39}Ar and ^{36}Ar from calcium, and ^{36}Ar from chlorine (Roddick, 1983; Renne et al., 1998; Renne and Norman, 2001)

Isotopic results obtained from laser step heating analysis of the biotite and muscovite extracted from specimens collected across study area are presented below ordered from south to north (Figs. 4.1; 4.2; 4.3). The spectra are plotted using Isoplot 3.7 (Ludwig, 2003). A plateau age, whenever present, is reported as the preferred age. In the absence of plateau age, an integrated age is reported, which is essentially the weighted mean of all the apparent ages excluding the outliers especially in the initial and final steps. Table 4.1 summarizes the preferred ages obtained for each specimen aliquot.

KM 078

This specimen is a quartz + feldspar + muscovite ± sericite schist collected towards the base of HMC in the Mahabharat range (Figs. 4.4; 4.5). Step heating analysis of muscovite reveals a spectrum with apparent ages ranging from a minimum of 17.18 ± 0.08 Ma to a maximum 18.62 ± 0.04 Ma without defining a distinct plateau (Fig. 4.1A). Steps 3 through 11 have a mean age of 17.56 ± 0.16 Ma with an MSWD of 11.6 with 81% of ^{39}Ar released, which is taken as the preferred age.

Table 4.1. Argon ages

Specimen	Muscovite Age (Ma)	Biotite Age (Ma)
KM 078	17.78 ± 0.31	
KM 074	19.34 ± 0.18	
KM 073	18.04 ± 0.06*	19.25 ± 0.31*
KM 068	21.34 ± 0.44*	74.77 ± 0.43
KM 060	32.57 ± 0.45	
KM 054	18.92 ± 0.02*	
KM 053A	21.52 ± 0.17	67.10 ± 1.70
KM 051B	27.63 ± 0.11	167.50 ± 1.50
KM 051A	18.22 ± 0.14	
KM 031	539 ± 330	26.80 ± 1.20
KM 030	14.82 ± 0.43	
KM 25A	1190 ± 44	
KM 014		23.98 ± 0.17*
KM 013	584 ± 440	
LK 032	13.39 ± 0.05*	24.55 ± 0.26
LK 039		9.93 ± 0.45
LK 046	11.78 ± 0.21	30.34 ± 0.37
LK 048	12.00 ± 0.78	20.30 ± 0.43
LK 051		14.69 ± 0.31
LK 052		10.40 ± 0.02*
LK 055		10.24 ± 0.42
LK 059		10.67 ± 0.55

* indicates plateau ages; others are integrated ages

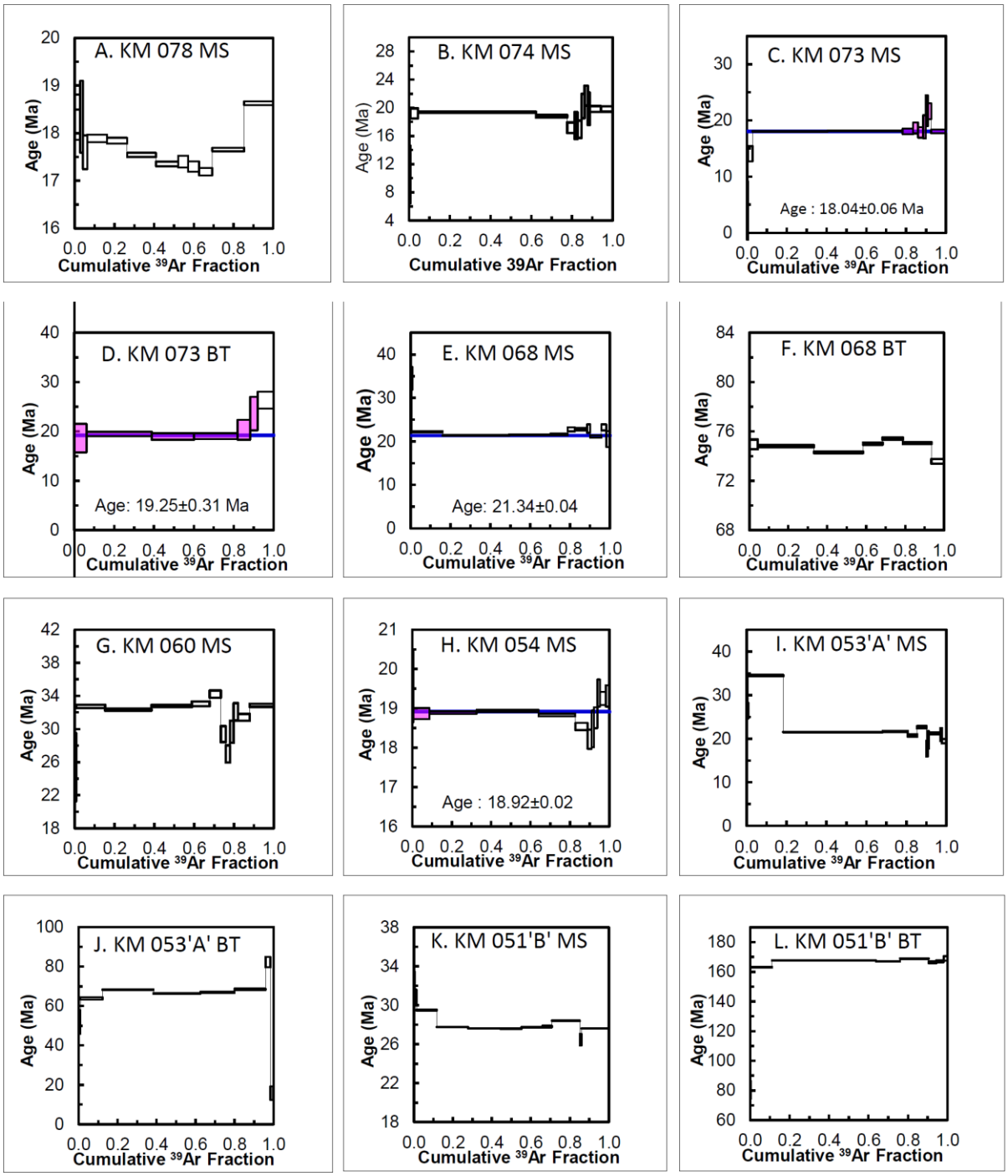

Figure 4.1. $^{40}Ar^*/^{39}Ar$ age spectra. Plateau ages are blue. Plateau steps are magenta. Box heights are 1σ.

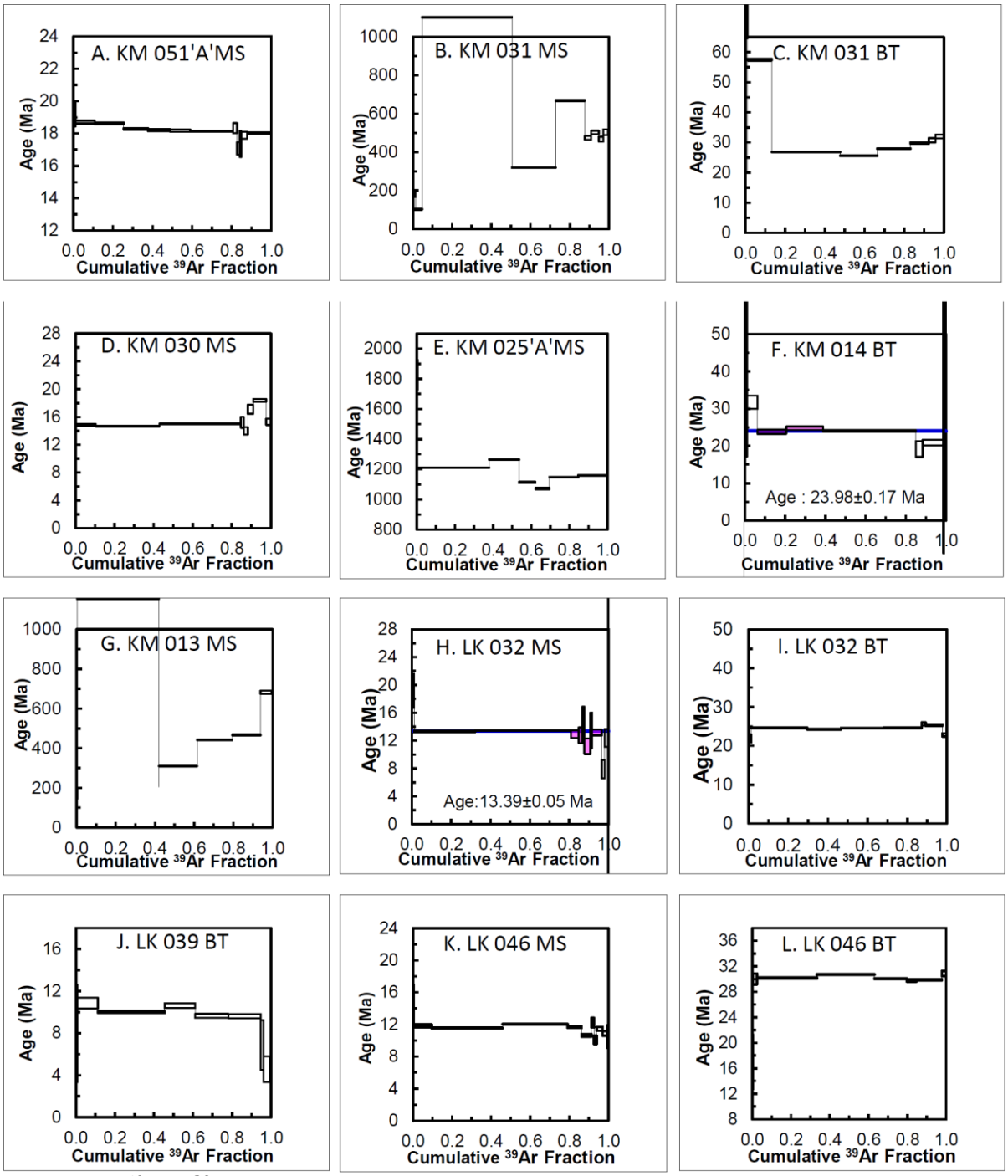

Figure 4.2. $^{40}Ar^*/^{39}Ar$ age spectra. Plateau ages are blue. Plateau steps are magenta. Box heights are 1σ.

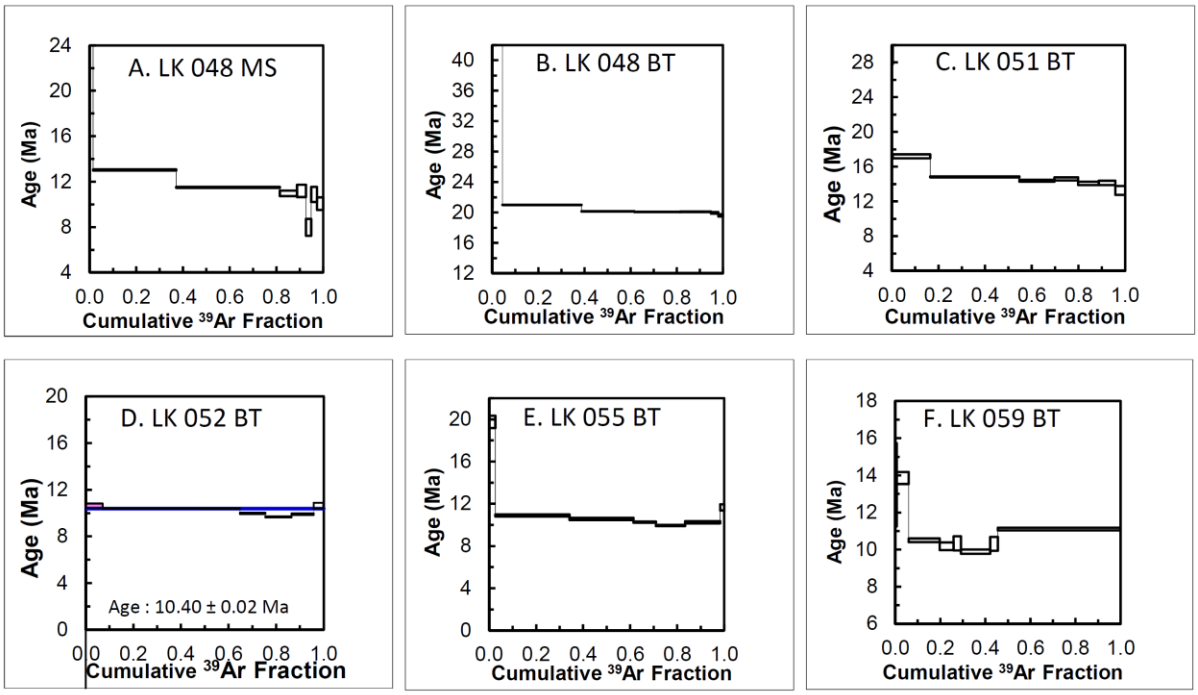

Figure 4.3. $^{40}Ar^*/^{39}Ar$ age spectra. Plateau ages are blue. Plateau steps are magenta. Box heights are 1σ.

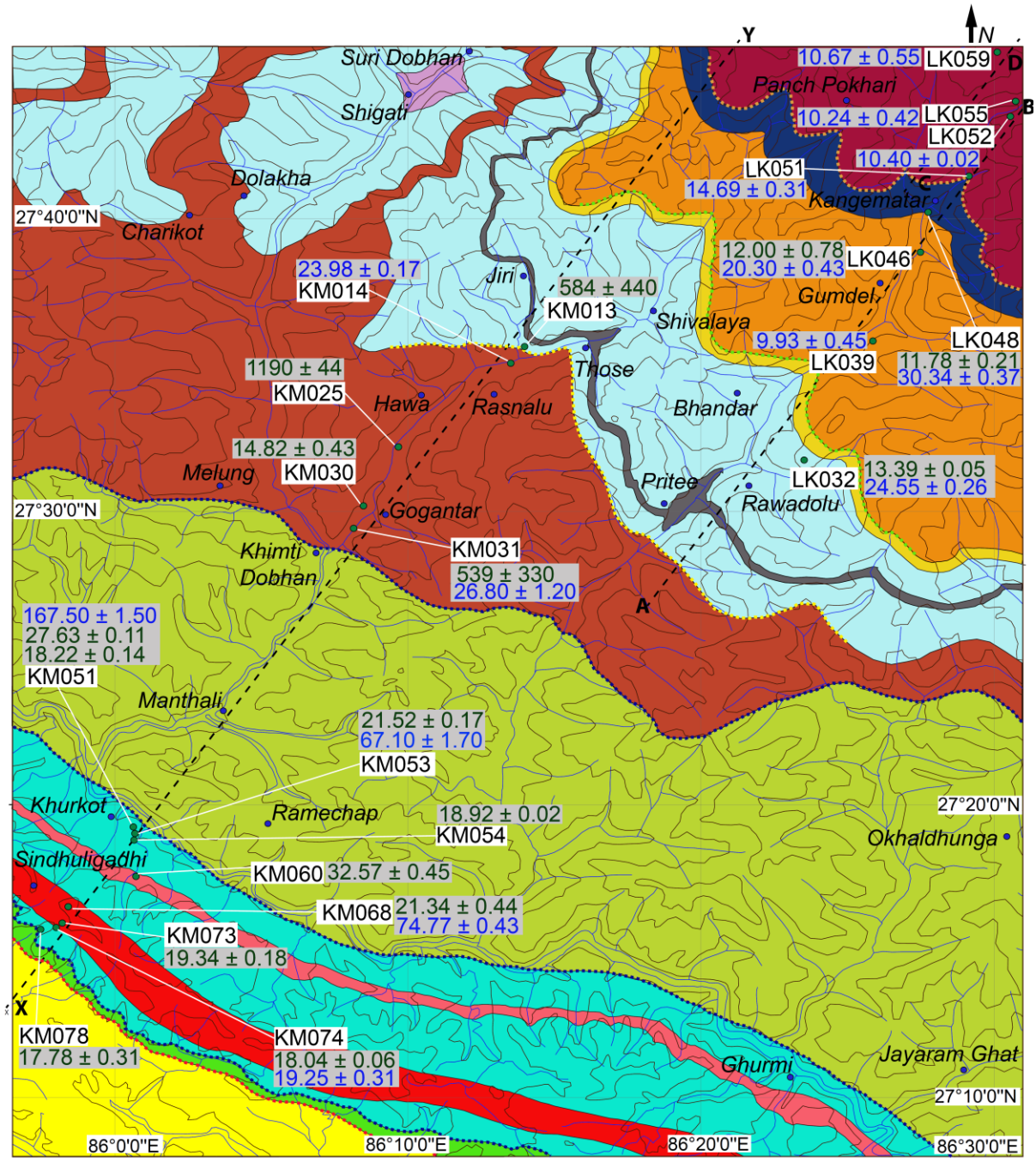

Figure 4.4. Geological Map of the study area showing $^{40}Ar^*/^{39}Ar$ age.

(Legends on next page.)

Figure 4.4 continued

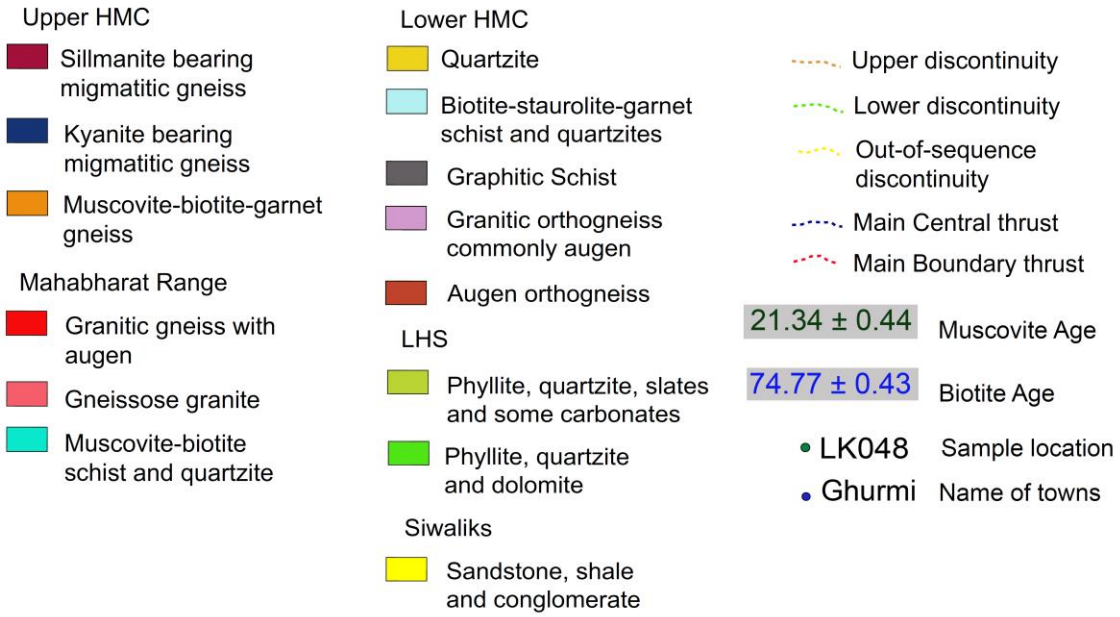

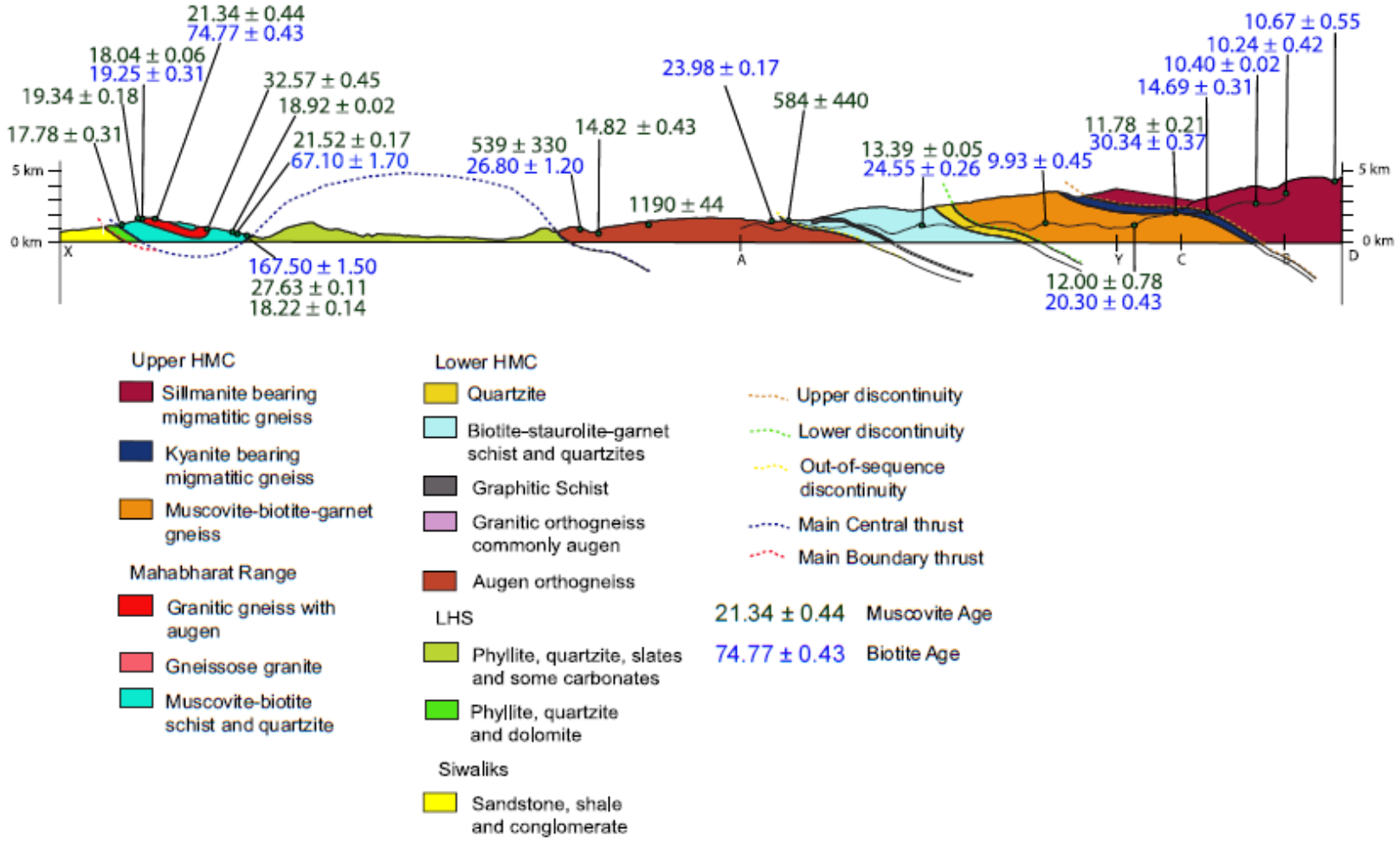

Figure 4.5. Geological cross section showing $^{40}Ar/^{39}Ar$ ages

KM 074

KM 074 is a granitic orthogneiss with a composition of quartz + K-feldspar + plagioclase + muscovite ± garnet ± biotite (Figs. 4.4; 4.5). Muscovite analysis reveals an almost flat spectrum with the third step along incorporating 58.1% of total ^{39}Ar released (Fig. 4.1B). An integrated age of 19.34 ± 0.18 Ma (MSWD = 3.1; 99.44% ^{39}Ar) is determined using all but the first step of the spectrum.

KM 073

This specimen is a biotite-rich band of orthogneiss associated with KM 074 (Figs. 4.4; 4.5). It has a composition of quartz + K-feldspar + muscovite + biotite ± tourmaline ± garnet. Muscovite analysis reveals a plateau age of 18.04 ± 0.06 Ma (MSWD = 1.12; 97.1% ^{39}Ar) from steps 3 through 11 (Fig. 4.1C). The biotite analysis from this specimen resulted in a plateau age of 19.25 ± 0.31 Ma (MSWD = 0.58; 92.1% ^{39}Ar) excluding first step (Fig. 4.1D).

KM 068

KM 068 is a granitic orthogneiss (Figs. 4.4; 4.5) that consists of quartz + K-feldspar + plagioclase + muscovite + biotite ± tourmaline. Biotite commonly occurs as intergrowths with muscovite. The muscovite analysis reveals a plateau age of 21.34 ± 0.44 Ma (MSWD = 1.4; 62.9 % ^{39}Ar) (Fig. 4.1E). An indistinguishable integrated age of 21.46 ± 0.27 is calculated by excluding the first two steps and incorporates 99.10% of ^{39}Ar released (MSWD = 8.3). Biotite analysis does not yield a plateau age (Fig. 4.1F). An integrated age of 74.77 ± 0.43 Ma (MSWD = 30) is calculated by rejecting the first step.

KM 060

This specimen is a granitic orthogneiss (Figs. 4.4; 4.5) with quartz + K-feldspar + muscovite ± biotite ± garnet. Muscovite step heating analysis yields an age spectrum without a plateau, but with a flat region in the initial steps (Fig. 4.1G). An integrated age of 32.57 ± 0.42 Ma (MSWD = 8; 99.3 % of ^{39}Ar) is calculated by excluding the first step. Steps 2 through 5 define a flat region of the spectrum that has a comparable mean age of 32.57 ± 0.45 Ma (MSWD = 3.6; 67.2% of ^{39}Ar).

KM 054

This specimen (Figs. 4.4; 4.5) is a light-coloured, muscovite-rich gneiss consisting of quartz + K-feldspar + plagioclase + muscovite ± biotite ± garnet ± tourmaline. Muscovite analysis reveals a plateau age of 18.92 ± 0.02 Ma (Fig. 41H; MSWD = 0.59; 64.3% ^{39}Ar). A comparable integrated age of 18.88 ± 0.07 (MSWD = 3.7) was calculated using all steps.

KM 053A

KM 053A (Figs. 4.4; 4.5) is a quartz + muscovite + biotite schist. Muscovite analysis reveals a complex spectrum with the apparent ages flattening out in the middle portion (Fig. 4.1I). Steps 4 through 7 have a mean age of 21.53 ± 0.29 Ma (MSWD = 11.0) with 71.6% ^{39}Ar released. An integrated age of 21.52 ± 0.17 Ma (MSWD = 7.4; 81.63% ^{39}Ar) is defined using steps 4 through 12. Biotite analysis also does not result in a plateau age (Fig. 4.1J). An integrated age of 67.1 ± 1.7 Ma is derived from steps 2 through 6, which includes 95.16% of ^{39}Ar released, but has an MSWD = 182.

KM 051B

This specimen was sampled from biotite rich orthogneiss (Figs. 4.4; 4.5) with a composition of quartz + feldspar + biotite + muscovite ± tourmaline. The biotite appears to be partially intergrowth with the muscovite. Though muscovite analysis does not produce a well-defined plateau, steps 5 through 9 form a saddle shaped region covering much of the first two thirds of the spectrum (Fig. 4.1K). These steps have a mean age of 27.63 ± 0.11 Ma with an MSWD = 5.6 including 59.2% of ^{39}Ar released. This is comparable to the 27.82 ± 0.38 Ma integrated age (MSWD = 147) calculated ignoring the first three steps and representing 98.72% of ^{39}Ar released.

Analysis of biotite from KM 051B results in an essentially flat spectra, but no plateau age (Fig. 4.1L). Steps 2 through 8, covering 99.77% of ^{39}Ar released, are used to calculate an integrated age of 167.20 ± 1.20 Ma (MSWD = 49). If steps 3 through 5, which represent the flat central portion of the spectrum, are used they yield a comparable mean age of 167.50 ± 1.50 Ma (MSWD = 21; 79.6% ^{39}Ar).

KM 051A

KM 051A is from a light coloured muscovite-rich part of the orthogneiss at the same location as the previous specimen (Figs. 4.4; 4.5). It includes quartz + K-feldspar + plagioclase + muscovite ± biotite ± tourmaline. The muscovite can be separated into a coarser grained older population and a finer grained younger population that defines the foliation plane. The older generation muscovite seems to have been deformed during a later deformation event. Step heating reveals a younging age spectrum towards higher temperature steps (Fig. 4.2A). The integrated age using all steps is 18.22 ± 0.14 Ma (MSWD = 10.3).

KM031

This specimen is a quartz + K-feldspar + plagioclase + muscovite + biotite orthogneiss (Figs. 4.4; 4.5). Like the previous specimen it contains two generations of muscovite, with an earlier coarse grain population variably replaced by later, finer grains (Appendix B). The second generation muscovite are aligned with the foliation plane. Step heating of the coarse grained muscovite reveals a complex spectrum with no plateau (Fig. 4.2B) and apparent age steps ranging from 1090.17 ± 1.66 Ma to 98.73 ± 2.63 Ma. In contrast, biotite, which may be the product of recrystallization of older generation biotite (Appendix B) reveals a saddle shaped spectra with no resolvable plateau age (Fig. 4.2C). Saddle steps 3 through 5 have a weighted mean age of 26.60 ± 2.20 Ma (MSWD = 81; 70.06% ^{39}Ar). An integrated age for the specimen, calculated by rejecting first two steps, is 26.8 ± 1.2 Ma (MSWD = 75; 86.74% ^{39}Ar).

KM030

This specimen is from a leucogranite body that intrudes the Melung orthogneiss (Figs. 4.4; 4.5). It has a mineral composition quartz + feldspars + muscovite + tourmaline. Muscovite step heating analysis yields an age spectrum that is generally flat, but does not define a plateau age (Fig. 4.2D). Steps 2 through 4, which include 84.48% of ^{39}Ar released have a weighted mean age of 14.82 ± 0.43 Ma (MSWD = 18). A comparable integrated age of 14.88 ± 0.42 Ma (MSWD = 58), is calculated excluding the first step and including 99.78% of ^{39}Ar released.

KM 025A

KM 025A is also from a leucogranite intruded into the orthogneiss (Figs. 4.4; 4.5). The mineral composition is quartz + K-feldspar + muscovite; K-feldspar shows minor sericitization. Two generations of muscovite are observable with the older generation being replaced by the later generation. Step heating of muscovite, possibly older generation grains, reveals ages ranging from 1066.33 ± 4.50 Ma to 1825.28 ± 102.65 with no plateau (Fig. 4.2E). An integrated age of 1190 ± 44 Ma (MSWD = 467) is calculated using all steps.

KM 014

This orthogneiss specimen (Figs. 4.4; 4.5) has a mineral assemblage including quartz + plagioclase + K-feldspar + muscovite + biotite ± garnet. Biotite seems to have recrystallized from older generation muscovite. Upon step heating, biotite reveals a plateau age of 23.98 ± 0.17 Ma with MSWD of 1.09 (Fig. 4.2F). The plateau includes steps 3 through 5 and 78.86% of ^{39}Ar released.

KM 013

KM 013 is a quartz-dominated schist (Figs. 4.4; 4.5) that contains more than one generation of muscovite. The coarser grained older generation muscovite grains show evidence of deformation while the finer grained younger generation muscovite and biotite grains are aligned with the foliation plane. Upon laser step heating, the coarser grained (older generation) muscovite revealed a staircase-type age spectrum (Fig. 4.2G) with maximum 1247.20 ± 1.88 Ma and minimum 306.74 ±1.42 apparent ages.

LK 032

This specimen is a garnet-bearing, micaceous schist (Figs. 4.4; 4.5) with composition of quartz + plagioclase + biotite + muscovite + garnet. Muscovite step heating analysis reveals a plateau age of 13.39 ± 0.05 Ma (Fig. 4.2H) with an MSWD of 0.96, covering 95.46% of ^{39}Ar released. A comparable integrated age, excluding the first and final steps, of 13.38 ± 0.17 Ma, MSWD = 2.8, is calculated covering 98.68% of ^{39}Ar released. Biotite analysis reveals an essentially flat spectrum, but no plateau age (Fig. 4.2I). An integrated age of 24.59 ± 0.24 Ma (MSWD = 17; 99.94% ^{39}Ar) was calculated excluding the first step. For steps 3 through 6,

which include 86% of ^{39}Ar released, and form the flattest part of the spectrum have a mean age of 24.55 ± 0.26 Ma with an MSWD of 10.6.

LK 039

LK 039 is a garnet bearing schistose paragneiss (Figs. 4.4; 4.5) composed of quartz + feldspar + biotite + muscovite ± garnet. Biotite analysis reveals a spectrum that is almost flat, but cannot be resolved as a plateau (Fig. 4.2J). A mean age of 9.93 ± 0.45 (MSWD = 4.4) was calculated using steps 2 through 6 including 94.34% of ^{39}Ar released.

LK 046

LK 046 is a garnet bearing quartz + muscovite + biotite schistose gneiss (Figs. 4.4; 4.5). Muscovite step heating analysis results in age steps ranging from 10.48 ± 1.48 Ma to 14.58 ± 2.38 Ma with no defined plateau (Fig. 4.2K). An integrated age of 11.78 ± 0.21 Ma (MSWD = 28; 99.59% of ^{39}Ar released) is calculated excluding the first two steps. Biotite analysis also results in a relatively flat spectrum without a resolvable plateau age (Fig. 4.2L). An integrated age of 30.34 ± 0.37 Ma (MSWD = 20) was calculated from all but the first step including 99.79% of ^{39}Ar released.

LK 048

This specimen is a kyanite bearing schistose paragneiss (Figs. 4.4; 4.5) comprising muscovite + biotite + quartz + plagioclase + perthite + feldspar + garnet + kyanite. Muscovite step heating analysis results in a descending ladder-like age spectrum ranging from a maximum of 33.02 ± 1.25 Ma to a minimum of 7.98 ± 0.74 Ma age (Fig. 4.3A). An integrated age of 12.00 ± 0.78 Ma (MSWD = 85; 98.50% ^{39}Ar) is calculated for all but the first step. Biotite analyses from this specimen yield an older integrated age of 20.30 ± 0.43 Ma (MSWD = 238; 95.58 % ^{39}Ar) excluding the first two steps (Fig. 4.3B).

LK 051

LK 051 is a sillimanite bearing migmatitic gneiss (Figs. 4.4; 4.5) with mineral composition of quartz + plagioclase + sillimanite + biotite ± muscovite ± garnet. Biotite analysis yields a descending ladder-shaped spectrum lacking a plateau (Fig. 4.3C). The

maximum apparent age is 33.66 ± 5.85 Ma while the minimum is 13.28 ± 0.51 Ma. An integrated age of 14.69 ± 0.31 Ma (MSWD = 7.1; 83.51% ^{39}Ar) is calculated for all but the first two steps.

LK 052

This specimen is from a sillimanite bearing migmatitic gneiss (Figs. 4.4; 4.5) comprising sillimanite + biotite + muscovite + quartz. Biotite analysis reveals a plateau age of 10.40 ± 0.02 Ma (MSWD 0.85; 64.8% ^{39}Ar) between steps 2 through 5 (Fig. 4.3D). A comparable integrated age of 10.28 ± 0.24 Ma covering 99.89% of total ^{39}Ar released has an MSWD of 37.

LK 055

LK 055 is a sillimanite bearing migmatitic gneiss (Figs. 4.4; 4.5) made up of sillimanite + quartz + plagioclase + biotite + muscovite + garnet. Biotite step heating results in a "U-shaped" spectrum (Fig. 4.3E) with no plateau age. The steps 3 through 7, which form the saddle, have a mean age of 10.24 ± 0.42 Ma (MSWD = 22; 95.66% ^{39}Ar). An almost identical integrated age of 10.25 ± 0.39 Ma (MSWD = 22) is calculated from all but the first two steps and includes 97.40% of total ^{39}Ar released.

LK 059

LK 059 is also a sillimanite bearing migmatitic gneiss (Figs. 4.4; 4.5) composed of quartz + feldspar + muscovite + biotite + garnet + sillimanite. Biotite step heating analysis failed to define any plateau, with the final step alone accounting for almost 55% ^{39}Ar release (Fig. 4.3F). An integrated age of 10.67 ± 0.55 Ma (MSWD = 20; 94.05% ^{39}Ar) is calculated for all except the first two steps.

Chapter 5 Excess Argon

5.1 The Himalayan Biotite Problem

One insight that can be gained from a cursory look at the dates obtained in this study is that those extracted from biotite are commonly older than those obtained from muscovite from the same specimen even though biotite has a lower theoretical closure temperature than muscovite (Table 4.1). This same pattern has been noted across the Himalaya (see: Copeland et al., 1991; Hubbard and Harrison, 1998; Maluski et al., 1988; Macfarlane, 1993; Huntington et al., 2006; Bollinger and Janots, 2006; Herman et al., 2008; Stübner et al., 2016). This phenomenon may be attributed to the vulnerability of biotite to problems of excess argon, perhaps due to its inherent properties like composition and crystal chemistry that can have effect on diffusion behaviour of the mineral grain (Treloar et al., 2000). Moreover, since biotite has a lower closure temperature compared to other potassium bearing minerals it remains open to diffusion of argon for a longer time, thus prolonging the window for potential excess argon accumulation during cooling brought about by exhumation.

5.2 Diffusion of Argon in mica

The diffusion behaviour of argon in a mineral has a critical fore-bearing in $^{40}Ar^{*}/^{39}Ar$ geochronology (Hames and Bowring, 1994). It is also key to understanding the model diffusional geometry that is important in the measurement of effective diffusion dimension, activation energy and diffusion coefficient, thus permitting estimation of closure temperature (Hames and Bowring, 1994). The diffusion or diffusion-related properties of minerals can be explained in simplest form through considerations of crystal geometry and bonding theory (Dowty, 1989). Dowty (1989) showed that diffusion was strongly influenced by crystal-chemical factors. He suggested that the amount of open space in the crystal structure is an important factor in diffusion through a given structure.

Using phlogopite (more stable under higher temperature than other mica species) under hydrothermal conditions, Giletti (1974) was able to demonstrate that there is a preferential transport of argon parallel to the basal cleavage. This was confirmed by later laser spot analyses of single mica grains (Hames and Bowring, 1994; Kelly, 2002a). The pronounced diffusion

anisotropy for O and Ar in mica is believed to be rooted in crystal chemistry (Grove and Harrison, 1996; Dahl, 1996a). The crystal structure of mica consists of parallel 2:1 layers (T–O–T) sheets alternating with layers of large alkali cations (Dahl, 1996a). Because of its large size, ^{40}Ar* confined within homogeneous mica is likely to be confined to vacant interlayer sites between the comparatively closer packed 2:1 layer units (Grove and Harrison, 1996). This, used in conjunction with an ionic porosity model, predicts significantly higher diffusivities in the interlayer region.

Furthermore, biotite exhibits more abundant and relatively spacious interlayers with corresponding large cation sites compared to coexisting muscovite (Dahl, 1996a). This further implies that biotite possesses longer K–O spacing, higher value of interlayer porosity (Z) and generally weaker interlayer bonding. Therefore biotite can lose ^{40}Ar*, or gain excess Ar, more readily than coexisting muscovite, despite exposure of both minerals to uniform metamorphic conditions. Therefore, metamorphic biotite grains typically yield either somewhat younger cooling age (compared to muscovite) or anomalously old apparent ages (McDougall and Harrison, 1998; Dahl, 1996a).

These issues can be further exacerbated by changes in mineral chemistry. Data on diffusivities (D) of O and Ar indicate differences in K–O bond length according to composition. The link between composition and the isotopic loss process implies that radiometric ages of coexisting micas can vary according to composition (controlled by K–O bond strength), provided all other factors are equal (Dahl, 1996a). Increasing Fe or Mg content, specifically the Mg/Fe ratio, in mica has been shown to lead to greater retentivity of ^{40}Ar* in both muscovite (Scaillet et al., 1992) and biotite (Harrison, 1985). This phenomena has been cited as giving rise to older apparent ages in high-Mg muscovite compared to coexisting intermediate-Mg muscovite (Scaillet et al., 1992). Grove and Harrison (1996), however, expressed doubts over the influence of Mg or Fe content alone over ^{40}Ar* retentivity in mica, suggesting a possible correlation with halogen content, especially F, with ^{40}Ar* retentivity. A term ‘halogen ratio’ defined as F/(F+OH+CL) can be used as a proxy for combined effect of total halogen content and it is positively correlated with ^{40}Ar* retentivity (Grove and Harrison, 1996).

5.3 Mica Chemical Composition

Electron microprobe analyses were carried out on six Mahabharat specimens (KM 078, KM 074, KM 073, KM 068, KM 060, KM 051A) collected near the Sindhuligadhi area (Figs. 4.4; 4.5) to test for the potential correlation between mineral chemistry and excess argon. These analyses were performed at the University of Manitoba, Winnipeg laboratory using a Cameca SX50 electron microprobe. Operating conditions were 15 keV accelerating voltage, 20 nA sample current and ~10 µm beam size. Representative results from microprobe analyses are listed in Table 5.1 (Muscovite) and Table 5.2 (Biotite) along with their $^{40}Ar^*/^{39}Ar$ age.

Only slight variation in composition was recorded in muscovite from all the six specimens (Table 5.1) except for very high BaO content in KM 068, KM 073 and KM 074. Total FeO content hovered between 3.14 and 3.93 in most cases, with exceptions noted for a maximum of around 4.75 in specimen KM 060, and a minimum of 1.88 in KM 074. No appreciable change in total MgO content was observed in most specimens, staying between 1.05 and 1.52, in all except specimen KM 074 where it dropped to 0.20-0.25.

The only appreciable variation in the Mg/(Mg+Fe) ratio was observed in the specimen KM 074. The low value for Mg/(Mg+Fe) ratio in KM 074 may indicate decrease in potential $^{40}Ar^*$ retentivity in muscovite of this particular specimen (Scaillet et al, 1992). The typical result should be a younger age compared to adjacent specimen contrary to the current study where it is older.

Halogen content was very low in all specimens with most variation observed in the F content. Following Grove and Harrison (1996), the halogen ratio F/(F+OH+Cl) was calculated assuming that F+OH+Cl = 2. The halogen ratio was considerably higher in KM 060 and was accompanied by corresponding increase in total F content possibly indicating high $^{40}Ar^*$ retentivity (Grove and Harrison, 1996). This coupled elevation of halogen ratio and total F content is also evident in specimen KM 073, which showed second highest value for both (Grove and Harrison, 1996).

Table 5.1. Electron Microprobe Analysis of Muscovite (representative data)

Oxides	**KM 051A**		**KM 054**		**KM 060**		**KM 068**	**KM 073**	**KM 074**	
SiO_2	46.49	46.21	45.84	45.34	46.26	46.71	46.34	46.22	45.75	45.89
TiO_2	0.51	1.22	0.54	0.54	0.78	0.71	1.59	0.76	0.60	0.59
Al_2O_3	31.28	30.07	33.00	32.13	29.06	29.39	30.47	30.97	35.15	34.84
Cr_2O_3	0.00	0.00	0.00	0.00	0.00	0.00	0.00	0.00	0.00	0.00
FeO(total)	3.38	3.93	3.38	3.15	4.76	4.73	3.66	3.89	1.88	1.88
MnO	0.04	0.01	0.04	0.04	0.16	0.13	0.02	0.05	0.06	0.08
MgO	1.21	1.34	1.21	1.05	1.36	1.33	1.52	1.26	0.20	0.25
CaO	0.02	0.00	0.02	0.02	0.02	0.03	0.00	0.00	0.00	0.01
BaO	0.08	0.03	0.08	0.00	0.07	0.02	10.65	10.46	10.65	10.23
Na_2O	0.30	0.34	0.30	0.29	0.50	0.47	0.20	0.03	0.08	0.00
K_2O	9.75	10.78	9.75	9.15	9.89	10.19	0.38	0.52	0.54	0.72
F	0.38	0.32	0.38	0.15	1.39	1.38	0.21	0.86	0.33	0.32
Cl	0.03	0.00	0.03	0.01	0.03	0.01	0.00	0.01	0.00	0.01
TOTAL	93.47	94.25	94.57	91.87	94.28	95.10	95.04	95.03	95.24	94.82
†Mg/(Mg+Fe)	0.39	0.38	0.39	0.37	0.34	0.33	0.43	0.37	0.16	0.19
†F/(F+OH+Cl)	0.04	0.03	0.04	0.02	0.15	0.15	0.02	0.09	0.04	0.03
$^{40}Ar/^{39}Ar$ Age	**18.22 ± 0.14**		**18.92 ± 0.02***		**32.57 ± 0.45**		**21.34 ± 0.44***	**18.04 ± 0.06**	**19.34 ± 0.18***	

Oxides reported in Wt%

† indicates atomic ratios reported

* indicates plateau ages; others are integrated ages

Table 5.2. Electron Microprobe Analysis of Biotite (representative data)

Oxides	**KM 073**		**KM 068**	
SiO_2	35.00	35.28	35.61	35.64
TiO_2	3.38	3.09	3.41	3.11
Al_2O_3	17.72	18.21	16.39	16.34
Cr_2O_3	0.00	0.00	0.00	0.00
FeO(total)	25.23	24.89	21.25	20.93
MnO	0.46	0.40	0.43	0.41
MgO	3.82	3.71	8.55	8.97
CaO	0.01	0.01	0.02	0.02
BaO	9.41	9.41	9.49	9.56
Na_2O	0.00	0.00	0.11	0.07
K_2O	0.05	0.03	0.08	0.09
F	1.45	1.32	0.41	0.63
Cl	0.08	0.08	0.10	0.10
TOTAL	96.61	96.43	95.85	95.87
†Mg/(Mg+Fe)	0.21	0.21	0.42	0.43
†F/(F+OH+Cl)	0.18	0.17	0.05	0.08
$^{40}Ar/^{39}Ar$ Age	**19.25 ± 0.31***		**74.77 ± 0.43**	

Oxides reported in Wt%

† indicates atomic ratios reported

* indicates plateau ages; others are integrated age

Based on the above, it can be inferred that specimen KM 060, which has the highest total F content and accompanied halogen ratio, should be the most $^{40}Ar^*$ retentive. It has the oldest 'Himalayan' muscovite age 32.57 ± 0.45 Ma out of those analysed, which is consistent with the findings of Grove and Harrison (1996). Meanwhile, specimen KM 068, despite having one of the lowest halogen ratios, is the second oldest specimen. It does, however, have the highest MgO content as well as Mg/(Mg+Fe) ratio, thus indicating potentially high retentivity of $^{40}Ar^*$ consistent with the interpretations of Scaillet et al. (1992).

The two adjacent specimens, KM 073 and KM 074, however, defy both Grove and Harrison (1996) and Scaillet et al. (1992). KM 073 has higher MgO and F content and also a higher Mg/(Mg+Fe) and halogen ratio compared KM 074. In theory, this should mean that KM 073 would be more retentive of argon (Scaillet et al., 1992; Grove and Harrison, 1996) and thus yield older dates than KM 074, which is the inverse to that observed (Table 5.1). The older age of KM 074 may be indicative of increased argon diffusivity of the specimen making it more prone to accumulation of excess argon resulting in an older apparent age.

Microprobe analysis of biotite was only conducted in specimens KM 068 and KM 073 (Table 5.2). Both the specimen had a very high BaO content. While the two specimens did not show appreciable difference in total FeO content, the MgO content was markedly different. The total Mg/(Mg+Fe) ratio in KM 073 was in the low-Mg composition (Scaillet et al., 1992) at 0.21, while in KM 068 it almost reached intermediate-Mg composition (Scaillet et al., 1992) at 0.43. The F content along with the halogen ratio F/(F+OH+Cl), however, exhibited an opposite trend with a higher value in KM 073 than in KM 068 indicating that KM 073 should be more retentive or less diffusive of argon (Grove and Harrison, 1996). As with the contrasting muscovite ages discussed, the younger biotite age of KM 073 relative to KM 068 may be explained in terms of its reduced susceptibility to incorporating excess argon (Grove and Harrison, 1996). Because of biotite's overall increased diffusivity relative to muscovite, it could still be more prone to excess argon incorporation as reflected in the biotite ages from both specimens being older than their respective muscovite ages.

Chapter 6 Discussion

The ages obtained from the $^{40}Ar^*/^{39}Ar$ analyses are discussed below according to their geographic region and structural position (Fig. 6.1).

6.1.1 The Mahabharat Range

The Mahabharat crystallines in the southern part of the study area occupy the synclinal core of the Mahabharat range (Figs. 4.4; 4.5). Most of the ages obtained from the Mahabharat range are spread between ca. 17 Ma and 21 Ma (Fig. 6.1). These are consistent with monazite age data that indicate the Mahabharat rocks experienced peak metamorphism during late Eocene to early Oligocene and retrograde cooling during early to middle Miocene (Larson et al., 2016), much like the rest of HMC.

Specimen KM 078 comes from the basal portion of the south limb of the syncline and has a muscovite age of 17.56 ± 0.16 Ma (Fig. 6.1). This is similar to, but slightly younger than those from structurally higher specimens KM 074 (19.34 ± 0.18 Ma) and KM 073 (18.04 ± 0.06 Ma) (Fig. 6.1). The biotite age (19.25 ± 0.3 Ma) extracted from KM 073 is older than the muscovite age from the same specimen (Fig. 6.1; Table 4.1) despite having a lower theoretical closure temperature (grain size is the same). It is therefore discarded as suspect of being affected by excess argon (e.g. Copeland et al., 1991; Hubbard and Harrison, 1998; Maluski et al., 1988; Macfarlane, 1993; Huntington et al., 2006; Bollinger and Janots, 2006; Herman et al., 2008). Specimen KM 068 was sampled near the top of the Mahabharat range and returns a muscovite plateau age of 21.34 ± 0.04 Ma (Fig. 6.1). An old biotite age of 74.78 ± 0.43 Ma from the same specimen again does not make geologic sense and as such is discarded (Copeland et al., 1991; Hubbard and Harrison, 1998; Maluski et al., 1988; Macfarlane, 1993; Huntington et al., 2006; Bollinger and Janots, 2006; Herman et al., 2008).

On the northern limb of the Mahabharat syncline KM 060 records a 32.57 ± 0.42 Ma muscovite age (Fig. 6.1; Table 4.1). This age is significantly older than the monazite crystallization age obtained for Mahabharat rocks (Larson et al., 2016), which is not geologically feasible and as such is interpreted to reflect the incorporation of extraneous argon.

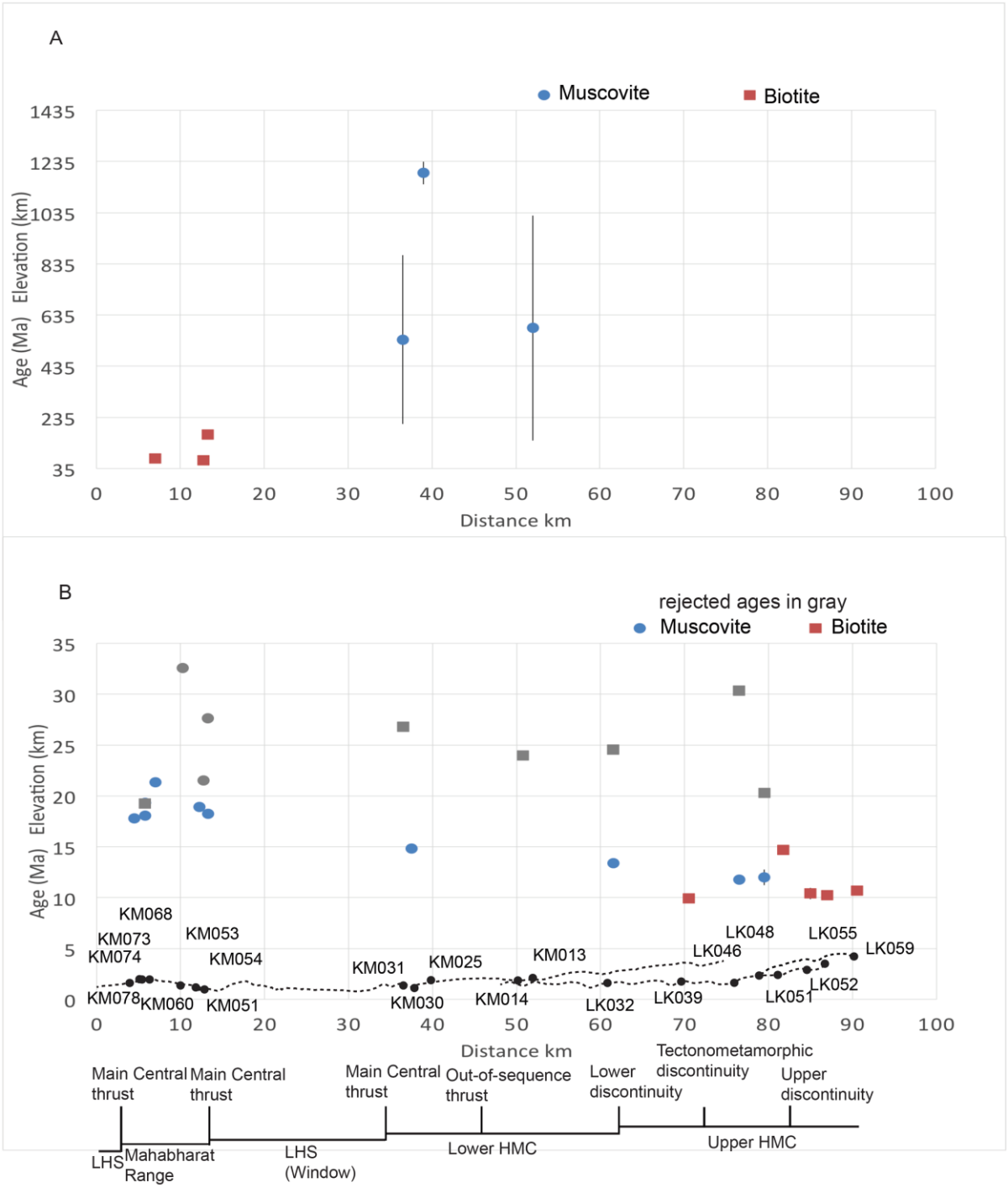

Figure 6.1. Spatial distribution of $^{40}Ar/^{39}Ar$ ages. A. Non-Himalayan (>55 Ma) ages. B. Himalayan (<55 Ma) ages. Spatial position of specimens is shown along a topographic profile (dashed).

KM 054 has a similar composition as KM 074, but is positioned just lower structurally. It yielded a muscovite plateau age of 18.92 ± 0.02 Ma (Fig 6.1). Farther down structural section muscovite from specimen KM053A is dated at 21.52 ± 0.17 Ma (Fig 6.1; Table 4.1) while biotite from the same rock gives an older age of 67.1 ± 1.7 Ma (Fig 6.1; Table 4.1). The older biotite age is interpreted to reflect excess argon and is discarded. Specimens KM 051A and B are from the lowest structural level on the northern limb of the Mahabharat syncline (Fig. 6.1). Biotite from KM 051B are significantly older (167.2 ± 1.20 Ma) than muscovite age of 27.63 ± 0.11 Ma (Fig 6.1; Table 4.1) and are discarded as geologically meaningless. The muscovite age from KM 051B is itself older than that measured in coarser-grained KM 051A muscovite of 18.22 ± 0.14 Ma (Fig 6.1; Table 4.1) from the same location. It is therefore also discarded as the presence of excess argon in biotite of the same rock indicates it may also have accumulated excess parentless material.

6.1.2 The Lower HMC

With the exception of KM 030, muscovite ages from Lower HMC specimens are much older than the initiation of the Himalaya (Fig. 6.1). Specimen KM 031 was taken from an augen orthogneiss at the lowest structural levels (Figs. 4.4; 4.5; 6.1; Table 4.1) of the Lower HMC sampled. Muscovite examined from the specimen do not yield an interpretable age, but individual steps are no younger than 98.73 ± 2.63 Ma. Similarly, KM 025 and KM 013 are both characterized by spectra with steps that do not fall below ca. 1066.33 ± 4.50 Ma and 306.74 ±1.42 respectively. Specimen KM 030, however, has a muscovite age with plausible geological significance. The 14.82 ± 0.43 Ma integrated age (Fig. 6.1) could either represent cooling through muscovite closure during exhumation or the magmatic age of the leucogranite.

LK 032, located at the highest structural level of Lower HMC, has a muscovite age of 13.38 ± 0.17 Ma and a biotite age that is significantly older at 24.59 ± 0.24 Ma (Fig. 6.1; Table 4.1). The biotite age is therefore considered to reflect excess argon.

In contrast to the muscovite ages in the lower HMC, the biotite ages from similar structural levels appear to be potentially more geologically plausible (Fig 6.1). Specimens KM 031 and KM 014, were both sampled from outcrops of Melung augen orthogneiss representing

its lowest and highest structural levels (Fig. 6.1). Both have late Oligocene biotite ages (KM 031, 26.60 ± 2.20 Ma; KM 014, 23.98 ± 0.17 Ma), however, published geochronological data in adjacent areas show a younger crystallization and muscovite cooling ages for rocks of similar composition and structural level (Larson et al., 2016). Thus, these dates are interpreted to reflect excess Ar.

6.1.3 The Upper HMC

The $^{40}Ar^*/^{39}Ar$ spectra from the Upper part of HMC yield ages that tend to be younger than those obtained from both the Mahabharat range and the Lower HMC (Fig. 6.1). A general northward younging trend is defined by the ages obtained (Fig. 6.1). As in the other areas examined, biotite ages are consistently older than muscovite ages from the same specimen (Fig. 6.1).

LK 039 is the southernmost and structurally lowest specimen of the Upper HMC (Fig. 6.1). It is located structurally above and to the north of LK 032 (Fig. 6.1). It yields a biotite age of 9.93 ± 0.45 Ma that appears to be unaffected by problems with its argon systematics and is, therefore, interpreted to reflect the time when this specimen cooled through biotite closure to argon diffusion.

The next higher specimen up structural section is LK 046 (Fig. 6.1), which yields a muscovite age of 11.78 ± 0.21 Ma (Table 4.1). This is indistinguishable from the muscovite age extracted from LK 048 of 12.00 ± 0.78 Ma, (Fig. 6.1), situated slightly higher up in structural level and elevation. The biotite ages older than muscovite ages in the same specimen are noted in both LK 046 and LK 048 (Fig. 6.1) wherein it is also interpreted to reflect excess argon. Published monazite age data (From et al., 2014) also support these inferences as the biotite age from LK 046 was older than its crystallization age obtained from monazite core age while in LK 048 the two ages were almost identical.

In the northernmost part of the study area (Fig. 6.1), which represents the highest structural position examined and contains the highest metamorphic grades sampled, biotite investigated is all middle Miocene in age (Fig. 6.1). It was not possible to extract datable

muscovite grains from these specimens. Specimen LK 051 yields the oldest age at 14.69 ± 0.31 Ma (Fig. 6.1; Table 4.1), while LK 052, 055, and 059 all yield ages within error at ca. 10.5 Ma (Figs. 5.1, 5.2, 5.3, Table 4.1). All these biotite ages are consistent with published monazite U-Th/Pb ages that indicate peak metamorphic conditions in late Oligocene to early Miocene followed by a retrograde path in the middle Miocene (From et al., 2014).

6.2 Cooling History and Exhumation of the of the Khimti-Tamakoshi-Sindhuligadhi Region

The Mahabharat crystallines have been correlated with similar or higher grade metamorphic rocks of the HMC (Schelling, 1992; Larson et al., 2016). The $^{40}Ar^*/^{39}Ar$ ages derived from the Mahabharat sequence range from ~17 Ma in KM 078 at the basal portion to ~21.42 Ma in KM 068 at the top with KM 073 in between at ~18 Ma (Fig. 6.1). This relationship indicates that the Mahabharat crystallines were cooling through the muscovite closure temperature for Ar diffusion in the early Miocene with higher structural levels cooling ca. 21 Ma, the middle portion following ca. 19 Ma, and the basal portion ca. 17 Ma. This is consistent with top-down erosion-driven cooling of the Mahabharat. These ages are significantly older than the rest of the HMC in the study area (Fig. 6.1), consistent with the Mahabharat rocks being part of the leading edge of the HMC that exhumed and cooled ahead of the more hinterland-ward portions.

The Main Central thrust mapped across the study area (Figs. 4.4; 4.5) forms the lower boundary of the Mahabharat range and is interpreted to have stacked the Mahabharat rocks over the LHS in the footwall. The early Miocene cooling ages from the hanging wall indicates movement was ongoing by the early Miocene, compatible with the activity of Main Central thrust throughout most of Himalaya coeval with the South Tibetan detachment system (Godin et al., 2006).

The Mahabharat range currently exists as a partial klippe separated from the distal portions of the extruding mid-crust by an erosional window that exposes the low grade metasedimentary rocks of the underlying LHS rocks (Fig. 4.5). Attempts to date these rocks failed due to absence of suitable datable material. It is, therefore, interpreted that these rocks

did not experience heating and burial prior to exhumation significant enough or for long enough to drive new mineral growth.

Step heating analysis of lower HMC specimens mostly yielded ages deemed meaningless. The maximum age fractions obtained from lower HMC muscovite (Figs. 4.1) are commonly more than 1 Ga, consistent with a Proterozoic protolith, likely of LHS affinity (Searle et al., 2008). The ages are generally younger than the established ca. 1.8 Ga age of lower LHS rocks (DeCelles et al., 2000; Kohn et al., 2010; Martin et al., 2011; Sakai et al., 2013, Larson et al., 2016), indicating an incomplete or partial resetting of the ^{40}Ar-^{39}Ar system. The 14.82 ± 0.43 (Fig. 6.1; Table 4.1) Ma muscovite age obtained from specimen KM 030, a leucogranite intrusion within the augen orthogneiss unit of lower HMC (Figs. 4.4; 4.5), provides an important timing constraint indicating that the Melung augen orthogneiss hosting the leucogranite in the lower HMC moved through muscovite closure no later than middle Miocene.

The Lower HMC orthogneiss is structurally below low grade metasedimentary rocks of LHS affinity with significantly younger cooling ages. The 13.38 ± 0.17 Ma muscovite age obtained from the highest structural level of the Lower HMC is significantly younger than that of the underlying Melung augen orthogneiss thus could indicate the presence of an out-of-sequence thrust sense discontinuity between the two disparate units of the Lower HMC (e.g. Larson et al., 2016).

The boundary between lower and upper HMC is marked by an observable change in lithology and metamorphic grade whereby paragneiss of garnet to sillimanite grade overlie schists of up to garnet or staurolite grade. This is accompanied by an appreciable break in the ^{40}Ar*/^{39}Ar ages (Fig. 6.1) between the two suites of rocks. The rocks structurally above this lithotectonic discontinuity have muscovite ages that range from 12 - 14 Ma, while biotite ages are more consistent ranging between 9 and 11 Ma (Fig. 6.1). This demonstrates that the Upper HMC cooled through the muscovite closure during the latter part of middle Miocene and through the biotite closure temperature in the early parts of late Miocene. All these cooling ages are significantly younger than those both in the Mahabharat Range and the Lower HMC

indicating a later exhumation of deeper seated material contrary to simple forward prograding wedge models that calls for younging cooling ages towards the foreland.

The higher structural levels of the HMC exhibit late Miocene cooling/exhumation significantly younger than the rocks of lower structural levels towards south. This is consistent with the presence of multiple thrusts (sometimes cryptic) across the HMC facilitating extrusion of the rocks in pulses (e.g. Carosi et al. 2010; Montomoli et al., 2013; 2015; Larson et al., 2013; 2015; 2016; Larson and Cottle, 2014; Cottle et al. 2015). Such discontinuities have been identified in the HMC within the study area as well as in studies of adjacent areas (Larson et al., 2013; 2016; From et al., 2014; Shrestha et al., In Press). The sharp decrease in cooling age between specimen LK 032 and the structurally higher specimens LK 039, LK 046, LK 048 (Figs. 4.4; 4.5; 6.1) coincides with the structural level of an out-of-sequence thrust identified in the adjacent Tamakoshi valley (Larson et al., 2016). In addition, From et al. (2014) and Shrestha et al. (In Press) identified a "tectonomorphic discontinuity" in the study area between specimens LK 039 and LK 046, however, the discontinuity was likely active at temperatures of ~ 650 °C (From et al., 2014; Shrestha et al. In Press) and therefore could not be verified based on the relationship between cooling ages of the two specimens.

The three specimens LK 052, LK 055 and LK 059 that represent the structurally highest positions in the study area have significantly younger cooling ages that the structurally lower specimen, LK 051 (Fig. 6.1). This break in cooling age coincides with the "upper discontinuity" in the adjacent Upper Tamakoshi area (Larson and Cottle, 2014) indicating it may have remained active, or been reactivated, at lower temperatures than originally suggested.

6.3 Kinematic Model

A kinematic model for the evolution of the study area is presented in Fig. 6.2. It is consistent with the data presented in this thesis as well as published data from nearby regions (e.g. Larson et al., 2013; 2016; From et al., 2014; From and Larson, 2014; Larson and Cottle, 2014, Larson et al., 2016). Published geochronology data indicate that the crystalline rocks of Mahabharat range, located towards the foreland experienced prograde metamorphism before

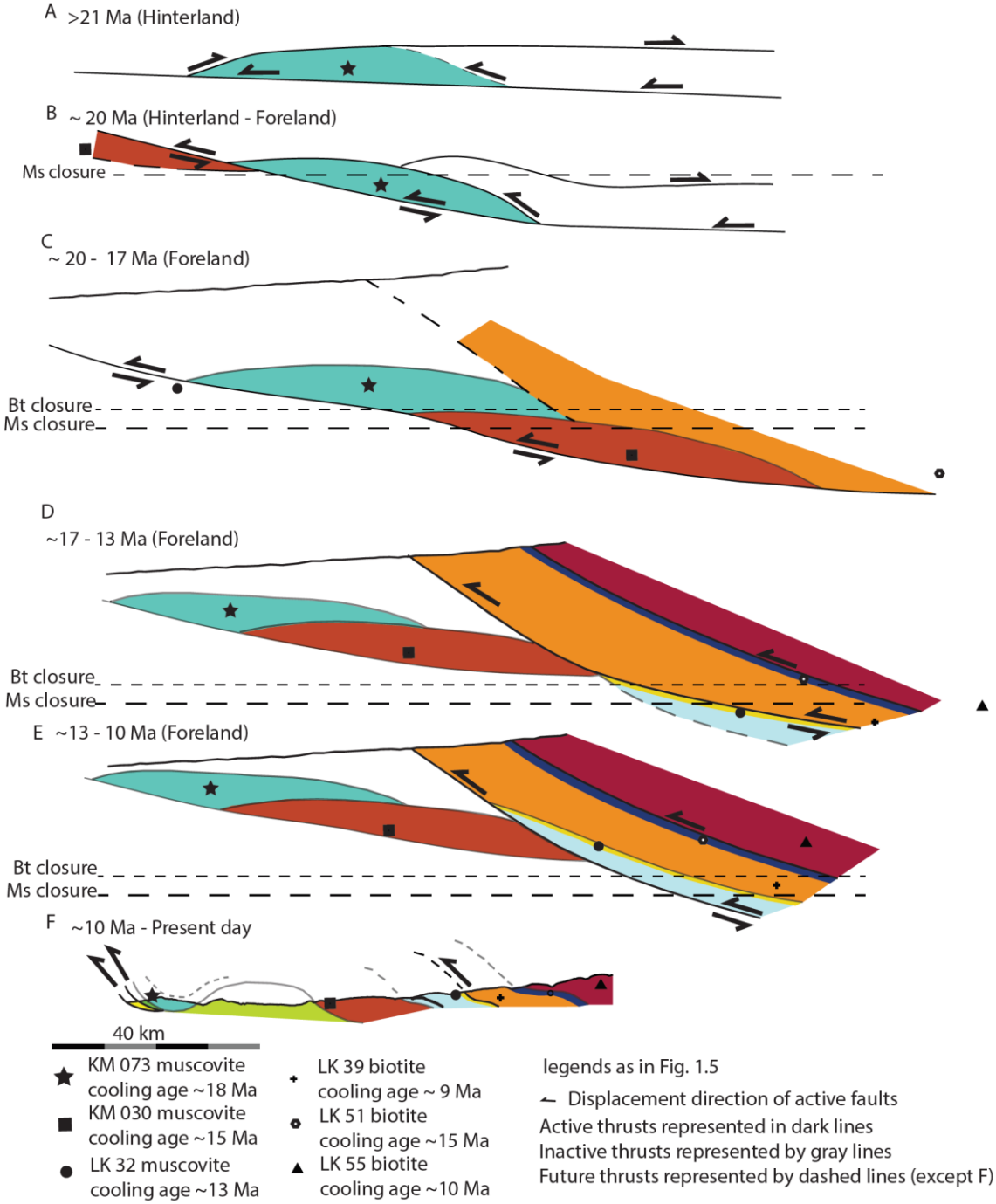

Figure 6.2. Schematic kinematic model of evolution of study area.

late Oligocene (Fig. 6.2A), coeval with the high-grade rocks of the upper HMC farther north (Larson et al., 2013; 2016; From et al., 2014; Larson and Cottle, 2014). The late Oligocene to early Miocene retrograde metamorphism (Larson et al., 2016) and the early Miocene cooling indicate that the Mahabharat range began exhuming in early Miocene time facilitated by the movement along Main Central thrust and concomitant erosion consistent with the observed top-down cooling pattern (Fig. 6.2B, C).

At the same time in the early Miocene, rocks of the lower HMC are interpreted to be buried in the under-thrusting Indian plate (Fig. 6.2B). The Paleoproterozoic Melung augen orthogneiss was buried deep enough and for long enough to partially reset its ^{40}Ar systemics and then incorporated in the hanging wall through underplating (Larson et al., 2016) and exhumed (Fig. 6.2C). A ca. 14 Ma muscovite age obtained in from the orthogneiss in the adjacent Tamakoshi valley (Larson et al., 2016) records peak metamorphism/burial and initiation of exhumation pre- middle Miocene (Fig. 6.2C). The ca. 15 Ma cooling age obtained from a leucogranite intrusion within the same orthogneiss unit in the present study area is consistent with that interpretation indicating that it was exhumed through the muscovite closure temperature along with its host rocks during the middle Miocene (Fig. 6.2D).

The Melung augen orthogneiss unit is structurally overlain by biotite-garnet schist of LHS affinity in the lower HMC with younger, ca. 13 Ma (LK 032), cooling ages. A similar juxtaposition has been explained in the adjacent Tamakoshi region as reflecting burial and subsequent out-of-sequence thrusting of footwall material over the orthogneiss (Fig. 6.2D; Larson et al., 2016).

The lower HMC is separated from the higher-grade rocks of the upper HMC by a prominent tectonometamorphic discontinuity (From et al., 2014; Shrestha et al. In Press). Published geochronology data (From et al., 2014; Larson et al., 2013; 2016) indicate that the upper HMC experienced peak metamorphism during late Oligocene to early Miocene and retrograde cooling during middle Miocene, indicating initiation of exhumation in the middle Miocene that cooled through the mica closure in the later part of Miocene (Fig. 6.2D, E).

Specimen LK 039, at the lowest structural levels of the upper HMC, cooled through biotite closure at ca. 9 Ma. This sharp drop in cooling age compared to the underlying lower HMC rocks may indicate thrust sense motion along the tectonometamorphic discontinuity separating the two units, possibly active between middle to late Miocene (Fig. 6.2D, E).

Finally, specimens LK 052, LK 055 and LK 059, the highest structural levels sampled in this study, have younger cooling ages than the underlying LK 046, LK 048 and LK 051. This indicates to a juxtaposition of rock packages along a thrust sense discontinuity with coeval erosion at ca. 12 Ma (Fig. 6. 2D, E). Subsequent erosion aided in the exhumation of these midcrustal rocks to the surface with the development of Lesser Himalayan duplex at depth (McQuarrie et al., 2014; Robinson et al., 2008).

6.4 Tectonic Implications

The presence of multiple late, thrust structure internal to the HMC has important implication on our understanding its kinematic evolution. This demonstrates convergence accommodation in Himalaya took place not only through foreland-ward propagation of thrusts as predicted by the critical/wedge tapering models in the shallow foreland (Kohn, 2008; Robinson et al., 2006), but also that this type of deformation overprinted earlier midcrustal deformation recorded in the deeper hinterland and juxtaposed rocks internally within the HMC.

It is estimated that 900 – 1200 km out of up to 2900 ± 900 km of north-south convergence since the initial collision of Indian and Eurasian tectonic plates has been absorbed in the Himalaya (Besse et al, 1984; Patriat and Achache, 1984; Schelling and Arita, 1991; Hauck et al., 1998; Yin and Harrison, 2000; DeCelles et al., 2001; 2002; Robinson et al., 2006; Yin, 2006; 2009; Khanal et al., 2013) based on paleomagnetic reconstruction, balanced cross-sections, seismic reflection profile and displacement estimates. The presence of multiple thrust structures within the HMC as outlined in this study can account for some of the remaining portion of convergence that has been attributed to shortening within the Tibetan plateau farther north (Besse et al, 1984; Patriat and Achache, 1984; Hauck et al., 1998; Yin and Harrison, 2000; Yin, 2006; 2009).

In addition, the results of the present study, thrusting at temperatures below Ar closure in mica in previously pervasively ductilely deformed, midcrustal rocks (From and Larson, 2014), are consistent with these rocks recording the transition from deep hinterland style deformation to shallow foreland style deformation predicted in some models for the evolution of the orogen (e.g. Larson et al. 2010; Larson et al. 2013; Larson and Cottle, 2014; Cottle et al. 2015). Finally, the stacking of discrete thrust sheets within the HMC could have significantly changed the geometry of both the internal and bounding structures, including the South Tibetan detachment system, which is looked at as an extensional fault at least partially due to its present dip to the north in inferred movement sense. If the fault had originally dipped to the south with later modification it could instead be interpreted as a thrust system, which would require a complete reworking of current orogenic models.

Chapter 7 Conclusions and Future Work

7.1 Conclusions

The present study provides insight into the evolution of the exhumed Himalayan mid-crust in the east central Nepal. The results of $40^{Ar}*/^{39}Ar$ thermochronology analysis of muscovite indicate that exhumation of Mahabharat rocks started in the middle Miocene ahead of the rest of HMC. This is compatible with observations across the Himalaya where the similar rocks occur as partial klippe or nappes in front of the Main Himalaya.

The $^{40}Ar*/^{39}Ar$ thermochronology data from the Lower HMC is characterized by ages much older than initiation of Himalayan orogeny (Patriat and Achache, 1984; Yin and Harrison, 2000; Hu et al., 2016), but well short of the Paleoproterozoic age of its protolith sourced from Indian craton (DeCelles et al., 2000; Kohn et al., 2010; Martin et al., 2011; Sakai et al., 2013). This apparent partial thermal resetting of the ^{40}Ar ages in lower HMC indicates the unit experienced elevated temperatures due to burial, but not high enough or long enough to completely reset its Ar systemics.

All the upper HMC ages are significantly younger than those both in the Mahabharat Range and the Lower HMC indicating later exhumation of deeper seated materials along a thrust present at the base of upper HMC contrary to the predictions of a simple forward prograding wedge model that calls for ages younging towards structurally lower parts. Breaks in the sequence of mica $^{40}Ar*/^{39}Ar$ ages internal to the HMC, however, may indicate the presence of multiple discontinuities within the HMC, consistent with observations made in other transects of the Himalaya (e.g. Carosi et al. 2010; Montomoli et al., 2013; 15; Larson et al., 2013; 2015; 2016; Larson and Cottle, 2014; Cottle et al. 2015).

Most biotite ages in the study area are affected by excess argon and are thus older than muscovite ages from the same specimen similar to other sections of Himalaya (eg. Copeland et al., 1991; Hubbard and Harrison, 1998; Maluski et al., 1988; Macfarlane, 1993; Huntington et al., 2006; Bollinger and Janots, 2006; Herman et al., 2008).

7.2 Future Work

LHS rocks in the study area did not yield muscovite or biotite crystals suitable for $^{40}Ar^{*}/^{39}Ar$ analysis. Thermochronological analysis using U-Th/He analysis or fission track dating could be used in these rocks to work out the low temperature evolution history of these rocks below Ar closure temperatures to further elucidate the development of the present-day structure.

Most biotite dates from the current study were affected by excess argon. The robustness of the muscovite ages could be ascertained by comparing with Rb-Sr analysis of mica from the same rock. In addition, most of the lower HMC specimen contain multiple generations of muscovite and biotite. These populations could be analyzed and dated separated by using in-situ dating techniques to see if they record different histories.

References

Allegre, C.O., Courtillot, V., Tapponnier, P., Hirn, A., Mattauer, M., Coulon, C., Jaeger, J.J., Achache, J., Schärer, U., Marcoux, J. and Burg, J.P., 1984. Structure and evolution of the Himalaya–Tibet orogenic belt. *Nature* **307**, 17 – 22, doi:10.1038/307017a0.

Arita, K., 1983. Origin of the inverted metamorphism of the Lower Himalayas, central Nepal. *Tectonophysics*, **95**, 43-60, doi : 10.1016/0040-1951(83)90258-5.

Arita, K., Dallmeyer, R.D. and Takasu, A., 1997. Tectonothermal evolution of the Lesser Himalaya, Nepal: Constraints from 40Ar/39Ar ages from the Kathmandu Nappe. *Island Arc*, **6**, 372-385, doi: 10.1111/j.1440-1738.1997.tb00047.x.

Avouac, J.P., 2003. Mountain building, erosion, and the seismic cycle in the Nepal Himalaya. *Advances in geophysics*, **46**, 1-80, doi: 10.1016/S0065-2687(03)46001-9.

Besse, J., Courtillot, V., Pozzi, J.P., Westphal, M., Zhou, Y.X., 1984. Paleomagnetic estimates of crustal shortening in the Himalayan thrusts and Zangbo suture. *Nature*, **311**, 621-626, doi: 10.1038/311621a0.

Beaumont, C., Jamieson, R.A., 2010. Himalaya-Tibetan Orogeny: Channel Flow versus (Critical) Wedge Models, a False Dichotomy? *USGS Open-File Report 2010-1099*. http://pubs.usgs.gov/of/2010/1099/beaumont/.

Beaumont, C., Jamieson, R.A., Nguyen, M.H., & Lee, B., 2001. Himalayan tectonics explained by extrusion of a low-viscosity crustal channel coupled to focused surface denudation. *Nature*, **414**, 738-742, doi:10.1038/4147381.

Beaumont, C., Jamieson, R.A., Nguyen, M.H., Medvedev, S., 2004. Crustal channel flows: Numerical models with applications to the tectonics of the Himalayan-Tibetan orogen. *Journal of Geophysical Research*, **109**, 1-29, doi: 10.1029/2003JB002809.

Best, M.G., Christiansen, E.H., Deino, A.L., Grommé, C.S., & Tingey, D.G., 1995. Correlation and emplacement of a large, zoned, discontinuously exposed ash flow sheet; the 40Ar/39Ar chronology, paleomagnetism, and petrology of the Pahrangat Formation, Nevada. *Journal of Geophysical Research*, **100**, 24593-24609, doi: 10.1029/95JB01690.

Bollinger, L. and Janots, E., 2006. Evidence for Mio-Pliocene retrograde monazite in the Lesser Himalaya, far western Nepal. *European Journal of Mineralogy*, **18**, 289-297, doi: 10.1127/0935-1221/2006/0018-0289.

Bollinger, L., Avouac, J.P., Beyssac, O., Catlos, E.J., Harrison, T.M., Grove, M., Goffe, B., and Sapkota, S., 2004. Thermal structure and exhumation history of the Lesser Himalaya in Central Nepal, *Tectonics*, **23**, 1-19. doi:10.1029/2003TC001564.

Bollinger, L., Henry, P., & Avouac, J.P., 2006. Mountain building in the Nepal Himalaya: Thermal and kinematic model. *Earth and Planetary Science Letters*, **244**, 58-71, doi: 10.1016/j.epsl.2006.01.045.

Buckingham H.M., 2015. Evolution and late stage deformation of the Himalayan Metamorphic Core, Kanchenjunga region, Eastern Nepal, Masters Thesis, UBC Okanagan.

Burchfiel, B.C., Zhiliang, C., Hodges, K.V., Yuping, L., Royden, L.H., Changrong, D. and Jiene, X., 1992. The South Tibetan detachment system, Himalayan orogen: Extension contemporaneous with and parallel to shortening in a collisional mountain belt. *Geological Society of America Special Papers*, **269**, 1-41. doi: 10.1130/SPE269-p1.

Burg, J.P., Brunel, M., Gapais, D., Chen, G.M. and Liu, G.H., 1984. Deformation of leucogranites of the crystalline Main Central Sheet in southern Tibet (China). *Journal of Structural Geology*, **6**, 535-542, doi: 10.1016/0191-8141(84)90063-4.

Camacho, A., personal communication, 2015. University of Manitoba, Winnipeg, Manitoba.

Carosi, R., Montomoli, C., Rubatto, D. and Visonà, D., 2010. Late Oligocene high-temperature shear zones in the core of the Higher Himalayan Crystallines (Lower Dolpo, western Nepal). *Tectonics*, **29**. doi: 10.1029/2008TC002400.

Catlos, E.J., Harrison, T.M., Kohn, M.J., Grove, M., Ryerson, F.J., Manning, C.E. and Upreti, B.N., 2001. Geochronologic and thermobarometric constraints on the evolution of the Main Central Thrust, central Nepal Himalaya. *Journal of Geophysical Research: Solid Earth*, **106**, 16177-16204, doi: 10.1029/2000JB900375.

Cattin, R. and Avouac, J.P., 2000. Modeling mountain building and the seismic cycle in the Himalaya of Nepal. *Journal of Geophysical Research: Solid Earth*, **105**, 13389-13407, doi: 10.1029/2000JB900032.

Coleman, M.E. and Hodges, K.V., 1998. Contrasting Oligocene and Miocene thermal histories from the hanging wall and footwall of the South Tibetan detachment in the central Himalaya from 40Ar/39Ar thermochronology, Marsyandi Valley, central Nepal. *Tectonics*, **17**, 726-740, doi: 10.1029/98TC02777.

Copeland, P., Harrison, T.M., Parrish, R., Burchfiel, B.C., Hodges, K. and Kidd, W.S.F., 1987. Constraints on the age of normal faulting, north face of Mt. Everest: Implications for Oligo-Miocene uplift. *Eos Trans. AGU*, **68**, 1444.

Copeland, P., Harrison, T.M. and Le Fort, P., 1990. Age and cooling history of the Manaslu granite: implications for Himalayan tectonics. *Journal of Volcanology and Geothermal Research*, **44**, 33-50, doi: 10.1016/0377-0273(90)90010-D.

Copeland, P., Harrison, T.M., Hodges, K.V., Maruéjol, P., Le Fort, P. and Pecher, A., 1991. An early Pliocene thermal disturbance of the Main Central Thrust, central Nepal:

Implications for Himalayan tectonics. *Journal of Geophysical Research: Solid Earth*, **96**, 8475-8500, doi: 10.1029/91JB00178.

Cottle, J.M., Larson, K.P. and Kellett, D.A., 2015. How does the mid-crust accommodate deformation in large, hot collisional orogens? A review of recent research in the Himalayan orogen. *Journal of Structural Geology*, **78**, 119-133, doi: 10.1016/j.epsl.2015.07.070

Dahl, P.S., 1996. The crystal-chemical basis for Ar retention in micas: inferences from interlayer partitioning and implications for geochronology. *Contributions to Mineralogy and Petrology*, **123**, 22-39, doi: 10.1007/s004100050141

DeCelles, P.G., Gehrels, G.E., Quade, J., LaReau, B. and Spurlin, M., 2000. Tectonic implications of U-Pb zircon ages of the Himalayan orogenic belt in Nepal. *Science*, **288**, 497-499, doi: 10.1126/science.288.5465.497.

DeCelles, P.G., Robinson, D.M., Quade, J., Ojha, T.P., Garzione, C.N., Copeland, P. and Upreti, B.N., 2001. Stratigraphy, structure, and tectonic evolution of the Himalayan fold-thrust belt in western Nepal. *Tectonics*, **20**, 487-509, doi: 10.1029/2000TC001226.

DeCelles, P.G., Robinson, D.M. and Zandt, G., 2002. Implications of shortening in the Himalayan fold-thrust belt for uplift of the Tibetan Plateau. *Tectonics*, **21**(6), 12-1-12-25, doi: 10.1029/2001TC001322.

DeCelles, P.G., Gehrels, G.E., Najman, Y., Martin, A.J., Carter, A. and Garzanti, E., 2004. Detrital geochronology and geochemistry of Cretaceous–Early Miocene strata of Nepal: implications for timing and diachroneity of initial Himalayan orogenesis. *Earth and Planetary Science Letters*, **227**, 313-330, doi: 10.1016/j.epsl.2004.08.019.

Dodson, M.H., 1973. Closure temperature in cooling geochronological and petrological systems. *Contributions to Mineralogy and Petrology*, **40**, 259-274, doi: 10.1007/BF00373790

Dowty, E., 1980. Crystal-chemical factors affecting the mobility of ions in minerals. *Am Mineral*, **65**, 174-182.

Edwards, R.M., 1995. 40Ar/39Ar geochronology of the Main Central Thrust (MCT) region: Evidence for late Miocene to Pliocene disturbances along the MCT, Marsyangdi River valley, west-central Nepal Himalaya. *J. Nepal Geol. Soc*, **10**, 41-46.

Faure, G. and Mensing, T.M., 2005. Isotopes. *Principles and applications*.

From, R. and Larson, K., 2014. Tectonostratigraphy, deformation, and metamorphism of the Himalayan mid-crust exposed in the Likhu Khola region, east-central Nepal. *Geosphere*, **10**, 292-307, doi: 10.1130/GES00938.1.

From, R., Larson, K. and Cottle, J.M., 2014. Metamorphism and geochronology of the exhumed Himalayan midcrust, Likhu Khola region, east-central Nepal: Recognition of a tectonometamorphic discontinuity. *Lithosphere*, **6**, 361-376, doi: 10.1130/L381.1.

Gansser, A., 1964. Geology of the Himalayas. Interscience Publishers London, New York, Sydney, p. 289.

Gansser, A., 1981. The geodynamic history of the Himalaya. *Zagros Hindu Kush Himalaya Geodynamic Evolution*, 111-121, doi: 10.1029/GD003p0111.

Garzanti, E., Casnedi, R. and Jadoul, F., 1986. Sedimentary evidence of a Cambro-Ordovician orogenic event in the northwestern Himalaya. *Sedimentary Geology*, **48**, 237-265, doi: 10.1016/0037-0738(86)90032-1.

Giletti, B.J., 1974. Studies in diffusion I: argon in phlogopite mica. In *Geochemical transport and kinetics*, **634**, 107-115. Carnegie Institute of Washington.

Godin, L., Parrish, R.R., Brown, R.L. and Hodges, K.V., 2001. Crustal thickening leading to exhumation of the Himalayan metamorphic core of central Nepal: Insight from U-Pb geochronology and 40Ar/39Ar thermochronology. *Tectonics*, **20**, 729-747, doi: 10.1029/2000TC001204.

Godin, L., Grujic, D., Law, R.D., Searle, M.P., 2006. Channel flow, ductile extrusion and exhumation in continental collision zones: An introduction. *Geological Society Special Publication*, **268**, 1-23.

Gong, J., Ji, J., Han, B., Chen, J., Sun, D., Li, B., Zhou, J., Tu, J., & Zhong, D., 2011. Early subduction-exhumation and late channel flow of the Greater Himalayan Sequence: implications from the Yadong section in the eastern Himalaya. *International Geology Review*, **54**, 1184-1202. doi:10.1080/00206814.2011.626604.

Grove, M. and Harrison, T.M., 1996. 40Ar* diffusion in Fe-rich biotite. *American Mineralogist*, ***81***, 940-951, doi: 10.2138/am-1996-7-816.

Guillot, S., Hodges, K., Le Fort, P. and Pêcher, A., 1994. New constraints on the age of the Manaslu leucogranite: Evidence for episodic tectonic denudation in the central Himalayas. *Geology*, **22**, 559-562, doi: 10.1130/0091-7613

Hames, W.E. and Bowring, S.A., 1994. An empirical evaluation of the argon diffusion geometry in muscovite. *Earth and Planetary Science Letters*, **124**, 161-169., doi: 10.1016/0012-821X(94)00079-4.

Harrison, T.M., Duncan, I. and McDougall, I., 1985. Diffusion of 40Ar in biotite: temperature, pressure and compositional effects. *Geochimica et Cosmochimica Acta*, **49**, 2461-2468, doi:10.1016/0016-7037(85)90246-7.

Hauck, M.L., Nelson, K.D., Brown, L.D., Zhao, W. and Ross, A.R., 1998. Crustal structure of the Himalayan orogen at∼ 90 east longitude from Project INDEPTH deep reflection profiles. *Tectonics*, **17**, 481-500, doi: 10.1029/98TC01314.

He, D., Webb, A.A.G., Larson, K.P., Martin, A.J. and Schmitt, A.K., 2015. Extrusion vs. duplexing models of Himalayan mountain building 3: Duplexing dominates from the Oligocene to present. *International Geology Review*, **57**, 1-27, doi: 10.1080/00206814.2014.986669.

Heim, A., Gansser. A., 1939.—Central Himalaya—Geological observation of the Swiss expedition, 1936. *Memoire, Societe Helvetique Science Naturelle*, **73**, 1–245.

Herman, F., Copeland, P., Avouac, J.P., Bollinger, L., Mahéo, G., Le Fort, P., Rai, S.M., Foster, D., Pêcher, A., Stüwe, K. and Henry, P., 2010. Exhumation, crustal deformation, and thermal structure of the Nepal Himalaya derived from the inversion of thermochronological and thermobarometric data and modeling of the topography. *Journal of Geophysical Research*, **115**, 1-38, doi:10.1029/2008JB006126.

Hodges, K.V., 2000. Tectonics of the Himalaya and Southern Tibet from two perspectives. *Geological Society of America*, **112**, 324-350, doi: 10.1130/0016-7606(2000)112<324:TOTHAS>2.0.CO;2

Hodges, K.V., 2006. A synthesis of the Channel Flow-Extrusion hypothesis as developed for the Himalayan-Tibetan orogenic system. *Geological Society, London, Special Publications*, **268**, 71-90.

Hodges, K.V., Bowring, S., Davidek, K., Hawkins, D. and Krol, M., 1998. Evidence for rapid displacement on Himalayan normal faults and the importance of tectonic denudation in the evolution of mountain ranges. *Geology*, **26**, 483–486, doi:10.1130/0091-7613(1998)026<0483:EFR- DOH>2.3.CO;2.

Hodges, K.V., Wobus, C., Ruhl, K., Schildgen, T. and Whipple, K., 2004. Quaternary deformation, river steepening, and heavy precipitation at the front of the Higher Himalayan ranges. *Earth and Planetary science letters*, *220*(3), pp.379-389, doi: 10.1016/S0012-821X(04)00063-9.

Hu, X., Wang, J., BouDagher-Fadel, M., Garzanti, E. and An, W., 2016. New insights into the timing of the India–Asia collision from the Paleogene Quxia and Jialazi formations of the Xigaze forearc basin, South Tibet. *Gondwana Research*, **32**, 76-92, doi: 10.1016/j.gr.2015.02.007.

Hubbard, M.S. and Harrison, T.M., 1989. 40Ar/39Ar Age constraints in deformation and metamorphism in the Main Central Thrust zone and Tibetan slab, eastern Nepal Himalaya. *Tectonics*, **8**, 865-880.

Huntington, K.W. and Hodges, K.V., 2006. A comparative study of detrital mineral and bedrock age-elevation methods for estimating erosion rates. *Journal of Geophysical Research: Earth Surface*, **111**, doi: 10.1029/2005JF000454.

Huntington, K.W., Blythe, A.E. and Hodges, K.V., 2006. Climate change and Late Pliocene acceleration of erosion in the Himalaya. *Earth and Planetary Science Letters*, **252**,107-118, doi: 10.1016/j.epsl.2006.09.031.

Hurtado, J.M., Hodges, K.V. and Whipple, K.X., 2001. Neotectonics of the Thakkhola graben and implications for recent activity on the South Tibetan fault system in the central Nepal Himalaya. *Geological Society of America Bulletin*, **113**, 222-240, doi: 10.1130/0016-7606(2001)113<0222:NOTTGA>2.0.CO;2.

Hurtado, J.M., and Hodges, K.V., 1998, The South Tibetan system in the Kali Gandaki Valley, Annapurna Himalaya, north central Nepal: A synthesis of structural geology and neotectonics. *Geological Society of America Abstracts with Programs*, **30**, p. 116–117.

Imayama, T., Takeshita, T., Yi, K., Cho, D.L., Kitajima, K., Tsutsumi, Y., Kayama, M., Nishido, H., Okumura, T., Yagi, K. and Itaya, T., 2012. Two-stage partial melting and contrasting cooling history within the Higher Himalayan Crystalline Sequence in the far-eastern Nepal Himalaya. *Lithos*, **134**, 1-22, doi: 10.1016/j.lithos.2011.12.004.

Ishida, T., 1969. Petrography and structure of the area between the Dudh Kosi and the Tamba Kosi, east Nepal. *Journal of the Geological Society of Japan*, **75**, 115-125.

Kellett, D.A., Grujic, D. and Erdmann, S., 2009. Miocene structural reorganization of the South Tibetan detachment, eastern Himalaya: Implications for continental collision. *Lithosphere*, **1**, 259-281, doi: 10.1130/L56.1

Kellet, D.A., Grujic, D., Coutand, I., Cottle, J. and Mukul, M., 2013. The South Tibetan detachment system facilitates ultra rapid cooling of granulite-facies rocks in Sikkim Himalaya. *Tectonics*, **32**, 1-28, doi:10.1002/tect.20014.

Kelley, S., 2002a. Excess argon in K-Ar and Ar-Ar geochronology. *Chemical Geology*, **188**, 1-22, doi: 10.1016/S0009-2541(02)00064-5.

Kelley, S., 2002b. K-Ar and Ar-Ar dating. *Reviews in Mineralogy and Geochemistry*, **47**, 785-818, doi: 10.2138/rmg.2002.47.17.

Khanal, S., Robinson D.M, 2013. Upper crustal shortening and forward modeling of the Himalayan thrust belt along the Budhi-Gandaki River, central Nepal. *International Journal of Earth Sciences*, 102, 1871-1891, doi: 10.1007/s/00531-013-0889-1.

Kohn, M.J., 2008. P-T-t data from central Nepal support critical taper and repudiate large-scale channel flow of the Greater Himalayan Sequence, *Geol. Soc. Am. Bull.*, **120**, 259–273, doi:10.1130/B26252.1.

Kohn, M.J., Paul, S.K. and Corrie, S.L., 2010. The lower Lesser Himalayan sequence: A Paleoproterozoic arc on the northern margin of the Indian plate. *Geological Society of America Bulletin*, **122**, 323-335, doi: 10.1130/B26587.1.

Krummenacher, D., Basett, A.M., Kingery, F.A., & Layne, H.F., 1978. Petrology, Metamorphism and K/Ar Age Determinations in Eastern Nepal. Tectonic Geology of the Himalaya: Saklani, P.S. (Ed). 151-166.

Kuiper, K.F., Deino, A., Hilgen, F.J., Krijgsman, W., Renne, P.R. and Wijbrans, J.R., 2008. Synchronizing rock clocks of Earth history. *Science*, **320**, 500-504, doi: 10.1126/science.1154339

Lanphere, M.A. and Dalrymple, G.B., 1976. Identification of excess 40Ar by the 40Ar/39Ar age spectrum technique. *Earth and Planetary Science Letters*, **32**, 141-148.

Larson, K.P., & Cottle, J.M., 2014. Midcrustal Discontinuities and the Assembly of the Himalayan mid-crust. *Tectonics*, **33**, 718-740, doi: 10.1002/2013TC003452.

Larson, K.P., Godin, L., Davis, W.J. and Davis, D.W., 2010a. Out-of-sequence deformation and expansion of the Himalayan orogenic wedge: insight from the Changgo culmination, south central Tibet. *Tectonics*, **29**, 1-30, doi:10.1029/2008TC002393.

Larson, K.P., Godin, L. and Price, R.A. 2010b. Relationships between displacement and distortion in orogens: Linking the Himalayan foreland and hinterland in central Nepal. *Geological Society of America Bulletin*, **122**, 1116-1134, doi:10.1130/B30073.1.

Larson, K.P., Gervais, F. and Kellett, D.A., 2013. A P-T-t-D discontinuity in east-central Nepal: Implications for the evolution of the Himalayan mid-crust: *Lithos*, **179**, 275–292, doi: 10.1016/j.lithos.2013.08.012.

Larson, K.P., Ambrose, T.K., Webb, A.A.G., Cottle, J.M. and Shrestha, S., 2015. Reconciling Himalayan midcrustal discontinuities: the Main Central thrust system. *Earth and Planetary Science Letters*, **429**, 139-146, doi: 10.1016/j.epsl.2015.07.070.

Larson, K.P., Kellett, D.A., Cottle, J.M., King, J., Lederer, G. and Rai, S.M., 2016. Anatexis, cooling, and kinematics during orogenesis: Miocene development of the Himalayan metamorphic core, east-central Nepal. Geosphere, 12, 1–19, doi:10.1130/GES01293.1.

Lavé, J. and Avouac, J.P., 2001. Fluvial incision and tectonic uplift across the Himalayas of central Nepal. *Journal of Geophysical Research: Solid Earth*, **106**, .26561-26591, doi: 10.1029/2001JB000359.

Le Fort, P., 1975. Himalayas: the collided range. Present knowledge of the continental arc. *American Journal of Science*, **275**, 1-44.

Le Fort, P., Cuney, M., Deniel, C., France-Lanord, C., Sheppard, S.M.F., Upreti, B.N. and Vidal, P.H., 1987. Crustal generation of the Himalayan leucogranites. *Tectonophysics*, **134**, 39-57, doi: 10.1016/0040-1951(87)90248-4.

Long, S.P., McQuarrie, N., Tobgay, T., Rose, C., Gehrels, G., and Grujic, D., 2011. Tectonostratigraphy of the Lesser Himalaya of Bhutan: Implications for the along-strike stratigraphic continuity of the northern Indian margin. *GSA Bulletin*, *123*, 1406–1426, doi: 10.1130/B30202.1.

Long, S.P., McQuarrie, N., Tobgay, T., Coutand, I., Cooper, F.J., Reiners, P.W., Wartho, J.A. and Hodges, K.V., 2012. Variable shortening rates in the eastern Himalayan thrust belt, Bhutan: Insights from multiple thermochronologic and geochronologic data sets tied to kinematic reconstructions. *Tectonics*, **31**, doi: 10.1029/2012TC003.

Ludwig, K.R., 2012. User's manual for Isoplot version 3.75: a geochronological toolkit for Microsoft *Excel. Berkley Geochronological Center Special Publication*, **5**.

Macfarlane, A.M., 1993. Chronology of tectonic events in the crystalline core of the Himalaya, Langtang National Park, central Nepal. *Tectonics*, **12**, 1004-1025, doi: 10.1029/93TC00916.

Macfarlane, A.M., 1995. An evaluation of the inverted metamorphic gradient at Langtang National Park, central Nepal Himalaya. *Journal of metamorphic Geology*, **13**, 595-612, doi: 10.1111/j.1525-1314.1995.tb00245.x.

Maluski, H., Matte, P. and Brunel, M., 1988. Argon 39-Argon 40 dating of metamorphic and plutonic events in the north and high Himalaya belts (southern Tibet-China). *Tectonics*, **7**, 299-326, doi: 10.1029/TC007i002p00299.

Martin, A.J., Burgy, K.D., Kaufman, A.J. and Gehrels, G.E., 2011. Stratigraphic and tectonic implications of field and isotopic constraints on depositional ages of Proterozoic Lesser Himalayan rocks in central Nepal. *Precambrian Research*, **185**, 1-17, doi: 10.1016/j.precamres.2010.11.003.

McDougall, I. and Harrison, T.M., 1999. Geochronology and Thermochronology by the 40Ar/39Ar method, 2E. Oxford, Oxford University Press.

McQuarrie, N., Robinson, D., Long, S., Tobgay, T., Grujic, D., Gehrels, G. and Ducea, M., 2008. Preliminary stratigraphic and structural architecture of Bhutan: Implications for the along strike architecture of the Himalayan system. *Earth and Planetary Science Letters*, **272**, 105-117, doi:10.1016/j.epsl.2008.04.030.

McQuarrie, N., Tobgay, T., Long, S.P., Rieners, P.W. and Cosca, M.A., 2014. Variable exhumation rates and variable displacement rates: documenting recent slowing of Himalayan shortening in western Bhutan. *Earth and Planetary Science Letters*, **386**, 161-174, doi: 10.1016/j.epsl.2013.10.045.

Merrihue, C.M., 1965. Trace-element determinations and potassium-argon dating by mass spectroscopy of neutron-irradiated samples. *Trans Am Geophys Union*, **46**, p.125.

Merrihue, C. and Turner, G., 1966. Potassium-argon dating by activation with fast neutrons. *Journal of Geophysical Research*, **71**, 2852-2857, doi: 10.1029/JZ071i011p02852.

Montomoli, C., Iaccarino, S., Carosi, R., Langone, A. and Visonà, D., 2013. Tectonometamorphic discontinuities within the Greater Himalayan Sequence in Western Nepal (Central Himalaya): Insights on the exhumation of crystalline rocks. *Tectophysics*, **608**, 1349-1370, doi:10.1016/j.tecto.2013.06.006.

Montomoli, C., Carosi, R. and Iaccarino, S., 2015. Tectonometamorphic discontinuities in the Greater Himalayan Sequence: a local or a regional feature?. *Geological Society, London, Special Publications*, **412**, 25-41, doi: 10.1144/SP412.3.

Patriat, P., Achache, J., 1984. India-Eurasia collision chronology has implications for crustal shortening and driving mechanism of plates. *Nature*, **311**, 615-621, doi: 10.1038/311621a0.

Parrish, R.R. and Hodges, V., 1996. Isotopic constraints on the age and provenance of the Lesser and Greater Himalayan sequences, Nepalese Himalaya. *Geological Society of America Bulletin*, **108**, 904-911, doi: 10.1130/0016-7606(1996)108<0904:ICOTAA>2.3.CO;2.

Renne, P.R., Swisher, C.C., Deino, A.L., Karner, D.B., Owens, T.L. and DePaolo, D.J., 1998. Intercalibration of standards, absolute ages and uncertainties in 40Ar/39Ar dating. *Chemical Geology*, **145**, 117-152, doi: 10.1016/S0009-2541(97)00159-9.

Renne, P.R. and Norman, E.B., 2001. Determination of the half-life of 37 Ar by mass spectrometry. *Physical Review C*, **63**, 047302, doi: 10.1103/PhysRevC.63.047302.

Robinson, D.M., DeCelles, P.G., Garzione, C.N., Pearson, O.N., Harrison, T.M. and Catlos, E.J., 2003. Kinematic model for the Main Central thrust in Nepal. *Geology*, **31**, 359-362, doi: 10.1130/G19730.1

Robinson, D.M., DeCelles, P.G. and Copeland, P., 2006. Tectonic evolution of the Himalayan thrust belt in western Nepal: Implications for channel flow models. *Geological Society of America*, **118**, 865-885. doi:10.1130/B25911.1.

Roddick, J.C., 1983. High precision intercalibration of 40 Ar-39 Ar standards. *Geochimica et cosmochimica Acta*, **47**, 887-898, 10.1016/0016-7037(83)90154-0.

Sakai, H., 1983. Geology of the Tansen Group of the Lesser Himalaya in Nepal. *Mem. Fac. Sci., Kyushu Univ.*, **25**, 27-74.

Sakai H., Takigami Y., Nakamuta Y. and Nomura H., 1999. Inverted metamorphism in the Pre-Siwalik foreland basin sediments beneath the crystalline nappe, western Nepal Himalaya. *Journal of Asian Earth Science* , **17**, 727–39, doi: 10.1016/S1367-9120(99)00035-8.

Sakai, H., Iwano, H., Danhara, T., Takigami, Y., Rai, S.M., Upreti, B.N. and Hirata, T., 2013a. Rift-related origin of the Paleoproterozoic Kuncha Formation, and cooling history of the Kuncha nappe and Taplejung granites, eastern Nepal Lesser Himalaya: a multichronological approach. *Island Arc*, **22**, 338-360, doi: 10.1111/iar.12021.

Sakai, H., Iwano, H., Danhara, T., Hirata, T., & Takigami, Y., 2013b. Emplacement of hot Lesser Himalayan nappes from 15 to 10 Ma in the Jumla–Surkhet region, western Nepal, and their thermal imprint on the underlying Early Miocene fluvial Dumri Formation. *Island Arc*, **22**, 361-381, doi: 10.1111/iar.12030.

Scaillet, S., Feraud, G., Ballevre, M. and Amouric, M., 1992. MgFe and [(Mg, Fe) Si-Al2] compositional control on argon behaviour in high-pressure white micas: A 40Ar39Ar

continuous laser-probe study from the Dora-Maira nappe of the internal western Alps, Italy. *Geochimica et Cosmochimica Acta*, **56**, 2851- 872, doi: 10.1016/0016-7037(92)90364-O.

Schelling, D., 1992. The tectonostratigraphy and structure of the eastern Nepal Himalaya. *Tectonics*, **11**, 925-943, doi: 10.1029/92TC00213.

Schelling, D. and Arita, K., 1991. Thrust tectonics, crustal shortening, and the structure of the far-eastern Nepal Himalaya. *Tectonics*, **10**, 851-862, doi: 10.1029/91TC01011.

Searle, M.P. and Godin, L., 2003. The South Tibetan detachment and the Manaslu leucogranite: A structural reinterpretation and restoration of the Annapurna-Manaslu Himalaya, Nepal. *The Journal of geology*, **111**, 505-523, doi: 10.1086/376763.

Searle, M.P., Windley, B.F., Coward, M.P., Cooper, D.J.W., Rex, A.J., Rex, D., Tingdong, Li, Xuchang, Xiao, Jan, M.Q., Thakur, V.C. and Kumar, S., 1987. The closing of Tethys and the tectonics of the Himalaya. *Geological Society of America Bulletin*, **98**, 678-701, doi: 10.1130/0016-7606(1987)98<678:TCOTAT>2.0.CO;2.

Searle, M.P., Law, R.D. and Jessup, M.J., 2006. Crustal structure, restoration and evolution of the Greater Himalaya in Nepal-South Tibet: implications for channel flow and ductile extrusion of the middle crust. *Geological Society, London, Special Publications*, *268*(1), pp.355-378, doi:

Searle, M.P., Law, R.D., Godin, L., Larson, K.P, Streule, M.J., Cottle, J.M. and Jessup, M.J., 2008. Defining the Himalayan Main Central Thrust in Nepal. *Journal of the Geological Society*, **165**, 523-534, doi: 10.1144/0016-76492007-081.

Shrestha, S., Larson, K.P., Guilmette, C. and Smit, M.A., 2017. The *P-T-t* evolution of the exhumed Himalayan metamorphic core in the Likhu Khola region, East Central Nepal. *J Metamorph Geol.* Accepted Author Manuscript. doi:10.1111/jmg.12250

Steiger, R.H., & Jager, E., 1977. Subcommision on geochronology: convention on the use of decay constants in geo- and cosmo-chronology. *Earth and Planetary Science Letters*, **36**, 121-122, doi: 10.1016/0012-821X(77)90060-7.

Stöcklin, J., 1980. Geology of Nepal and its regional frame Thirty-third William Smith Lecture. *Journal of the Geological Society*, **137**, 1-34, doi: 10.1144/gsjgs.137.1.0001.

Stübner, K., Warren, C., Ratschbacher, L., Sperner, B., Kleeberg, R., Pfänder, J. and Grujic, D., 2017. Anomalously old biotite 40Ar/39Ar ages in the NW Himalaya. *Lithosphere*, L586-1, doi: 10.1130/L586.1.

Stüwe, K. and Foster, D., 2001. 40 Ar/39 Ar, pressure, temperature and fission track constraints on the age and nature of metamorphism around the main central thrust in the eastern Bhutan Himalaya. *Journal of Asian Earth Sciences*, **19**, 85-95, doi: 10.1016/S1367-9120(00)00018-3.

Thiede, R.C., Arrowsmith, J.R., Bookhagen, B., McWilliams, M.O., Sobel, E.R. and Strecker, M.R., 2005. From tectonically to erosionally controlled development of the Himalayan orogen. *Geology*, **33**, 689-692, doi: 10.1130/G21483AR.1.

Treloar, P.J., Rex, D.C., Guise, P.G., Wheeler, J., Hurford, A.J. and Carter, A., 2000. Geochronological constraints on the evolution of the Nanga Parbat syntaxis, Pakistan, Himalaya. *Geological Society Special Publication*, **170**, 137-162.

Upreti, B.N., 1999. An overview of the stratigraphy and tectonics of the Nepal Himalaya. *Journal of Asian Earth Sciences*, **17**, 577-606. 10.1016/S1367-9120(99)00047-4.

Vannay, J.C., Grasemann, B., Rahn, M., Frank, W., Carter, A., Baudraz, V. and Cosca, M., 2004. Miocene to Holocene exhumation of metamorphic crustal wedges in the NW

Himalaya: Evidence for tectonic extrusion coupled to fluvial erosion. *Tectonics*, **23**, doi: 10.1029/2002TC001429.

Vannay, J.C. and Hodges, K.V., 1996. Tectonometamorphic evolution of the Himalayan metamorphic core between the Annapurna and Dhaulagiri, central Nepal. *Journal of Metamorphic Geology*, **14**, 635-656, doi: 10.1046/j.1525-1314.1996.00426.x.

Villa, I.M., 1990. Geochronology and excess Ar geochemistry of the Lhotse Nup leucogranite, Nepal Himalaya. *Geothermal Research*, **44**, 89-103, 10.1016/0377-0273(90)90013-6.

Villa, I.M., 1998. Isotopic closure. *Terra Nova-Oxford*, **10**, 42-47, doi: 10.1046/j.1365-3121.1998.00156.x

Villa, I.M., and Lombardo, B., 1986. Osservazioni cronometriche sul raffreddamento dei graniti himalayani: *Rendiconti della Società Italiana di Mineralogia e Petrologia*, **41**, 410.

Walker, J.D., Martin, M.W., Bowring, S.A., Searle, M.P., Waters, D.J. and Hodges, K.V., 1999. Metamorphism, melting, and extension: age constraints from the High Himalayan slab of southeast Zanskar and northwest Lahaul. *The Journal of Geology*, **107**, 473-495, doi: 10.1086/314360.

Webb, A.A.G., 2013. Preliminary balanced palinspastic reconstruction of Cenozoic deformation across the Himachal Himalaya (northwestern India). *Geosphere*, **9**, 572–587, doi: 10.1130/GES00787.1.

Webb, A.A.G., Yin, A., Harrison, T.M., Célérier, J. and Burgess, W.P., 2007. The leading edge of the Greater Himalayan Crystalline complex revealed in the NW Indian Himalaya: Implications for the evolution of the Himalayan orogen: *Geology*, **35**, 955, doi: 10.1130/G23931A.1.

Webb, A.A.G., Schmitt, A.K., He, D. and Weigand, E.L., 2011. Structural and geochronological evidence for the leading edge of the Greater Himalayan Crystalline complex in the central Nepal Himalaya: *Earth and Planetary Science Letters*, **304**, 483–495, doi: 10.1016/j.epsl.2011.02.024.

Wobus, C., Pringle, M., Whipple, K. and Hodges, K., 2008. A Late Miocene acceleration of exhumation in the Himalayan crystalline core. *Earth and Planetary Science Letters*, **269**, 1-10, doi: 10.1016/j.epsl.2008.02.019.

Yin, A., 2006. Cenozoic tectonic evolution of the Himalayan orogen as constrained by along-strike variation of structural geometry, exhumation history, and foreland sedimentation. *Earth-Science Reviews*, **76**, 1-131, doi: 10.1016/j.earscirev.2005.05.004.

Yin, A., 2009. Cenozoic tectonic evolution of Asia: A preliminary systhesis. *Tectonophysics*, **448**, 293-325, doi: 10.1016/j.tecto.2009.06.002.

Yin, A., and Harrison, T.M., 2000. Geologic evolution of the Himalayan Tibetan orogen: *Annual Reviews in Earth and Planetary Science*, **28**, 211–280, doi: 10.1146/annurev.earth.28.1.211.

Appendices

Appendix A: Thermochronology data from different regions of Himalaya

A1. Thermochronology of north-western India

Region	Rock Unit	Rock Type	Ar-Ar age (Ma)	K-Ar age (Ma)	Remarks
Walker et al., 1999					
Zanskar-Lahaul, north-west India	Top of GHS	Gneiss	20.4		Ms, isochron
Zanskar-Lahaul, north-west India	Top of GHS	Leucogranite	20.8		Ms, isochron
Zanskar-Lahaul, north-west India	Top of GHS	Leucogranite	20.2		Ms, isochron
Zanskar-Lahaul, north-west India			20.9		Bt, isochron
Zanskar-Lahaul, north-west India	Top of GHS	Leucogranite	20.8		Ms, isochron
Zanskar-Lahaul, north-west India	Top of GHS	Leucogranite	20.6		Ms, isochron
Zanskar-Lahaul, north-west India			20		Bt, isochron
Zanskar-Lahaul, north-west India	Middle of GHS	Gneiss	21.7		Ms, plateau
Zanskar-Lahaul, north-west India	Bottom of GHS	Gneiss	22		Ms, isochron
Theide et al., 2014					
Sutlej Section, north-west India	TSS		19.2		Ms, Vannay et al., 2004
Sutlej Section, north-west India	TSS		18.8		Ms, Vannay et al., 2004
Sutlej Section, north-west India	TSS		17.6		Ms, Vannay et al., 2004
Sutlej Section, north-west India	TSS	Immediate HW of STDS	17.2		Ms, Vannay et al., 2004

Region	Rock Unit	Rock Type	Ar-Ar age (Ma)	K-Ar age (Ma)	Remarks
Sutlej Section, north-west India	TSS	Immediate HW of STDS	17.03		Ms
Sutlej Section, north-west India	GHS Top	Immediate FW of STDS	16.18		Ms
Sutlej Section, north-west India	GHS Top (valley bottom)	Immediate FW of STDS	15.5		Ms, Vannay et al., 2004
Sutlej Section, north-west India	GHS Top		18.8		Ms, Vannay et al., 2004
Sutlej Section, north-west India	GHS Top		18.4		Ms, Vannay et al., 2004
Sutlej Section, north-west India	Middle GHS		15.9		Ms, Vannay et al., 2004
Sutlej Section, north-west India	Middle GHS		14.86		Ms
Sutlej Section, north-west India	Middle GHS (valley bottom)		19.9		Ms, Vannay et al., 2004
Sutlej Section, north-west India	GHS bottom		17.3		Ms, Vannay et al., 2004
Sutlej Section, north-west India	GHS bottom		16.4		Ms, Vannay et al., 2004
Sutlej Section, north-west India	GHS bottom	Immediate HW of MCT	9.7		Ms, Vannay et al., 2004
Sutlej Section, north-west India	LHS Top (valley bottom)	Immediate FW of MCT	4.4		Ms, Vannay et al., 2004
Sutlej Section, north-west India	LHS Top	Immediate FW of MCT	6.3		Ms, Vannay et al., 2004
Sutlej Section, north-west India	LHS Top		5.6		Ms, Vannay et al., 2004

Region	Rock Unit	Rock Type	Ar-Ar age (Ma)	K-Ar age (Ma)	Remarks
Sutlej Section, north-west India	LHS Middle		5.2		Ms, Vannay et al., 2004
Sutlej Section, north-west India	LHS Middle	Near valley bottom	6.68		Ms,
Sutlej Section, north-west India	LHS Middle	Valley bottom	4.3		Ms, Vannay et al., 2004
Sutlej Section, north-west India	TSS		19.2		Ms, Vannay et al., 2004
Sutlej Section, north-west India	TSS		18.8		Ms, Vannay et al., 2004
Sutlej Section, north-west India	TSS		17.6		Ms, Vannay et al., 2004
Sutlej Section, north-west India	TSS	Immediate HW of STDS	17.2		Ms, Vannay et al., 2004
Sutlej Section, north-west India	TSS	Immediate HW of STDS	17.03		Ms
Sutlej Section, north-west India	GHS Top	Immediate FW of STDS	16.18		Ms
Sutlej Section, north-west India	GHS Top (valley bottom)	Immediate FW of STDS	15.5		Ms, Vannay et al., 2004
Sutlej Section, north-west India	GHS Top		18.8		Ms, Vannay et al., 2004
Sutlej Section, north-west India	GHS Top		18.4		Ms, Vannay et al., 2004

A2. Thermochronology of far-western Nepal

Region	Rock Unit	Rock Type	Ar-Ar age (Ma)	K-Ar age (Ma)	Remarks
LeFort, 1987					
Zanskar	GHS	Leucogranite (several plutons)			Ms Rb-Sr age 17 Ma
Badrinath	GHS	Leucogranite (2plutons)		18	
Mustang	GHS	Leucogranite (=mugu)		15, 24	
Mustang	GHS	Leucogranite (=mugu)		20, 36	Bt
Sakai, 1999; Sakai 2013					
Jumla/Surkhet	GHS (Karnali Klippe)	Gneiss (Bt-Grt)	25.69		Bt plateau age (1999)
	Kunchha Nappe (MCT zone)	Schist (2-mica-Grt)	19.11		Ms
	Lahore Khola Augen Gneiss	Parajul Khola granite	258+		Bt (max age)
	LHS (Dumri Formation)	Metasandstone	16.64		Ms min age (1999)
			46.78		total fusion age
Bollinger and Janots, 2006					
Sirdang Window	Topmost LH	amphibolite (Hbl-Bt-Ab-Qz)	11.6		Bt (Plateau)
			12.5		Hbl (Plateau
Sirdang Window	Topmost LH	mica-schist (Grt-Bt-Ms)	8.7		Bt (Plateau)
			4.7		Ms (Plateau)
Askot-Chiplakot Window	LH (core of window)	Qz, Bt and carbonaceous material	16.1		Ms (Plateau)
Askot-Chiplakot Window	LH (core of window)		24.4		Ms (Weighted Mean Age)
Askot-Chiplakot Window	LH (core of window)		17.7		Ms (Weighted Mean Age)

A3. Thermochronology of west-central Nepal

Region	Rock Unit	Rock Type	Ar-Ar age (Ma)	K-Ar age (Ma)	Remarks
Arita et al, 1990					
Modi Khola upper stream	GHS, Upper Formation I	Ky-Grt-Bt Gneiss (Pelitic)		56.7	Bt
Modi Khola upper stream	GHS, Lower Formation I	Grt-Hbl-Pl calc. gneiss		61.5	Hbl
Bollinger et al, 2003					
Marsyangdi	LH north		9.3		Ms, Weighted mean age
Marsyangdi	LH north		6.9		
Marsyangdi	LH north		5.5		
Marsyangdi	LH north		5.6		
Marsyangdi	LH north		7.7		
Marsyangdi	LH north		5.7		
Marsyangdi	LH north		5.1		
Marsyangdi	LH north		3.9		
Marsyangdi	LH north		5.2		
Marsyangdi	LH north		10		
Marsyangdi	LH north		6.3		
Marsyangdi	LH south		4.3		
Marsyangdi	MCT Zone		2.4		
Marsyangdi	MCT Zone		18.9		
Marsyangdi	GHS		29.1		
Damauli	LH (Thrust)		15.6		
Damauli	LH (Thrust)		18.4		
Damauli	Damauli Klippe (Thrust)		22.4		
Damauli	LH		31.3		
Damauli	Damauli Klippe		23.8		
Catlos et al, 2001					
Marsyangdi	Formation II		15.5		Whole gas age
Marsyangdi	Formation II		16.6		Whole gas age
Marsyangdi	Formation II		14.9		Whole gas age
Marsyangdi	Formation I	Sil-gneiss	8.6		Whole gas age
Marsyangdi	Formation I	Ky-gneiss	4.6		Whole gas age

Region	Rock Unit	Rock Type	Ar-Ar age (Ma)	K-Ar age (Ma)	Remarks
Marsyangdi	Formation I	Ky-gneiss	9.4		Whole gas age
Marsyangdi	MCT zone	Ky-schist	6.2		Whole gas age
Marsyangdi	MCT zone	Ky-schist	3.1		Whole gas age
Marsyangdi	MCT zone	Ky-schist	2.9		Whole gas age
Marsyangdi	MCT zone	Grt-schist	2.8		Whole gas age
Daraudi	GHS Form. I	Ky/Sil	4.4		Whole gas age
Daraudi	MCT Zone	Ky/Sil-schist	2.8		Whole gas age
Daraudi	MCT Zone	Ky/Sil-schist	5.7		Whole gas age
Daraudi	MCT Zone	Ky/Sil-schist	7.9		Whole gas age
Daraudi	MCT Zone	Ky/Sil-schist	3.3		Whole gas age
Daraudi	MCT Zone	Ky/Sil-schist	2.64		Whole gas age
Daraudi	MCT Zone	Ky/Sil-schist	2.8		Whole gas age
Daraudi	MCT Zone	Grt-schist	3.4		Whole gas age
Daraudi	MCT Zone (at the base)	Grt-schist	6.28		Whole gas age
Daraudi	Ulleri Augen Gneiss	Augen gneiss	9.2		Whole gas age
Daraudi		Grt	4.85		Whole gas age
Daraudi		Bt	125		Whole gas age
Daraudi		Bt	275		Whole gas age
Coleman & Hodges, 1997					
Marsyangdi	TSS	phlogopite marble,	26.84		Phl plateau furnace
Marsyangdi	TSS	phlogopite marble	29.88		Phl plateau laser
Marsyangdi	Leucogranite dike (TSS)	Leucogranite	16.8		Bt plateau laser
Marsyangdi	TSS (Hanging wall)	biotite schist	28.71		Bt plateau laser
Marsyangdi	GHC Unit II	amphibolite gneiss	35.28		Hbl plateau furnace
Marsyangdi	GHC Unit III	Bt-schist/gneiss	15.53		Bt plateau laser
Marsyangdi	GHC Unit III	Foliated leucogranite	16.86		Bt plateau laser
Marsyangdi	GHC-UNIT II	Bt-schist/gneiss	15.13		Bt plateau laser
Godin et al, 2001					

Region	Rock Unit	Rock Type	Ar-Ar age (Ma)	K-Ar age (Ma)	Remarks
Kaligandaki	TSS Nilgiri Formation	limestone with fine bands of ms	18.1		Ms, isochron
Kaligandaki	TSS Annapurna Formation	calc-psammite Ms-Bt	12.7		Ms, isochron
			27.1		Bt, plateau
Kaligandaki	TSS Annapurna Formation	Ms-limestone	11.8		Ms, isochron
Kaligandaki	TSS		13.1		Vannay & Hodges 1996
Kaligandaki	Formation III	Bt-Grt schist	14.5		Bt, plateau/isochron
Kaligandaki	Formation III	leucogranitic augen gneiss	15.5		Ms, isochron
			22.1		Bt, isochron
Kaligandaki	Formation III	Bt-Grt schist	13.4		Ms, isochron
Kaligandaki	Formation III	leucogranitic augen gneiss	14.3		Ms, plateau
			13		Bt, plateau/isochron
Kaligandaki	Formation III		14.5		Vannay & Hodges 1996
Kaligandaki	Formation III	calc-silicate gneiss	52.1		Hbl, isochron
Kaligandaki	Formation I		14.7		Vannay & Hodges 1996
Kaligandaki	LHS		13.9		Vannay & Hodges 1996
Guillot et al, 1994					
Manaslu	Manaslu Granite	pelitic schist	18.5		Ms Isochron, Furnace
			20		Bt Isochron, Furnace

Region	Rock Unit	Rock Type	Ar-Ar age (Ma)	K-Ar age (Ma)	Remarks
Manaslu	Manaslu Granite	pelitic schist	18.5		Ms Isochron, Furnace
			18.3		Bt Isochron, Furnace
	Manaslu Granite		18.4		Ms,Copeland et al 1990
	Manaslu Granite		17.6		Ms, Copeland et al 1990
Manaslu	Manaslu Granite	impure calc. Sandstone	22.8		Hbl, Isochron, Furnace
			22.4		Hbl, Isochron, Laser
Manaslu	Manaslu Granite	impure calc. sandstone	22.8		Hbl, Isochron, Furnace
Manaslu	Manaslu Granite	impure calc. sandstone	18.6		Ms Isochron, Furnace
			17.6		Bt Isochron, Furnace
	Manaslu Granite		17.1		Ms, Copeland et al 1990
	Manaslu Granite		16.5		Bt, Copeland et al 1990
Huntington and Hodges, 2006					
Marsyangdi		Bahundada Gneiss	5.1		Ms, plateau
Marsyangdi		Bahundada Gneiss	3.49		Ms, Total fusion
Marsyangdi		Bahundada Gneiss	4.98		Ms, plateau
Marsyangdi		Bahundada Gneiss	4.13		Ms, plateau
Marsyangdi		Bahundada Gneiss	3.84		Ms, plateau
Marsyangdi		Bahundada Gneiss	3.32		Ms, Total fusion
Marsyangdi		Bahundada Gneiss	2.46		Ms, plateau

Region	Rock Unit	Rock Type	Ar-Ar age (Ma)	K-Ar age (Ma)	Remarks
Marsyangdi		Siurun Complex	5.3		Ms, Total fusion age

A4. Thermochronology of central Nepal

Region	Rock Unit	Rock Type	Ar-Ar age (Ma)	K-Ar age (Ma)	Remarks
Arita et al, 1997					
Tistung-Palung	Shivapuri Gneiss	Schist (Pelitic)	13.6		Ms
Tistung-Palung	Sopyang	Schist (Pelitic)	31		Ms
Tistung-Palung	Tistung	Phyllite	20.5		whole rock
Tistung-Palung	Kalitar	Schist (Pelitic)	15.1		Ms
Tistung-Palung	Palung Granite	Granite (Massive)	44		Ms
Tistung-Palung	Palung Granite	Granite (Massive)		49	Ms
Tistung-Palung	Palung Granite	Granite (Massive)		51	Ms
Tistung-Palung	Palung Granite	Granite (Mylonitic)	19.6		Ms
Tistung-Palung	Kunchha (just below MCT)	Metasandstone quartzose	15.4		Ms
Tistung-Palung	1 km from Palung Granite	Marble		48	Phl, Krummanacher
Macfarlane, 1993					
Langtang	LHS	Amphibilite	41		Hbl, minimum age
Langtang	MCT zone	fault gauge	2.3		Ms, isochron
Langtang	MCT zone	amphibolite	28.5		Hbl, total gas age
Langtang	MCT zone	augen orthogneiss	8.9		Ms, isochron
Langtang			21.4		Bt, isochron
Langtang			5.5		Kfs, minimum
Langtang	MCT zone	gt-ky pelitic gneiss	5.8		Ms, isochron
Langtang			7.8		Bt, isochron
Langtang	MCT zone	gt-ky pelitic gneiss	8.5		Ms, isochron
Langtang	MCT zone	gt-ky pelitic gneiss	6.9		Ms, isochron
Langtang			11		Bt, isochron

Region	Rock Unit	Rock Type	Ar-Ar age (Ma)	K-Ar age (Ma)	Remarks
Langtang	GHS	migmatitic pelitic gneiss	6.7		Ms, isochron
Langtang			12.7		Bt, isochron
Langtang	GHS	migmatitic pelitic gneiss	6.7		Ms, isochron
Langtang			16.3		Bt, isochron
Langtang	GHS	migmatitic pelitic gneiss	6.1		Ms, isochron
Langtang			8.4		Bt, isochron
Langtang	GHS	migmatitic pelitic gneiss	9.7		Ms, isochron
Langtang			86.4		Bt, isochron
Langtang	GHS	granite	4.6		Ms, isochron
Langtang			7.7		Bt, isochron
Langtang	GHS	sill-gt gneiss	5.4		Bt, isochron
Langtang	GHS	sill-gt gneiss	8		Bt, isochron
Langtang	GHS	granite	8.1		Bt, isochron
Langtang	GHS	migmatitic pelitic gneiss	19.3		Bt, isochron
Wobus et al, 2008					
Langtang Valley	GHS	Psammite	6.94		bt, isochron
Langtang Valley	GHS	Schist	8.39		bt, isochron
Langtang Valley	GHS	Schist	8.88		bt, isochron
Langtang Valley	GHS	migmatite	8.79		bt, total fusion
Langtang Valley	GHS	migmatite	8.08		bt, isochron
Langtang Valley	GHS	migmatite	9.44		bt, isochron
Langtang Valley	GHS	Gneiss	9.63		bt, isochron
Langtang Valley	GHS	Gneiss	12.9		bt, isochron
Langtang Valley	GHS	Gneiss	13.96		bt, isochron
Langtang Valley	GHS	Psammite	20.81		bt, isochron
Herman et al, 2008					
Kathmandu Complex			**9.6**		Ms, plateau,average
Kathmandu Complex			**7.8**		Ms, plateau

Region	Rock Unit	Rock Type	Ar-Ar age (Ma)	K-Ar age (Ma)	Remarks
Kathmandu Complex			5.1		Ms, Isochron
Kathmandu Complex			12.1		Ms, plateau,average
Kathmandu Complex			12.1		Ms, plateau,average
Kathmandu Complex			11.6		Ms, plateau
Kathmandu Complex			7.5		Ms, plateau
Kathmandu Complex			9.8		Ms, plateau,average
Kathmandu Complex			22		Ms, plateau
Kathmandu Complex			16.6		Ms, plateau,average

A5. Thermochronology of Eastern Nepal

Region	Rock Unit	Rock Type	Ar-Ar age (Ma)	K-Ar age (Ma)	Remarks
Hodges et al, 1998					
Everest	Rongbuk Granite	granite	16.56		Ms, Plateau
Everest	Rongbuk Granite	granite	16.51		Bt, Plateau
Everest	GHS Metasediments		20		
Hubbard & Harrison, 1989					
Everest	GHS Top	leucogranite	15.5		Kfs, Minimum age
Everest			16.6		Ms, Isochron
Everest	GHS Top	pegmatite	21.7		Kfs, Minimum age
Everest			16.8		Bt, Isochron
Everest			17		Ms, Isochron
Everest	GHS Top	Augen Gneiss	18.7		Kfs, Minimum age
Everest			17.2		Bt, Isochron
Everest	GHS Mid	Amphibolite	22.7		Hbl, Minimum age
Everest	GHS Mid	Bt-Gneiss	20.2		Bt, Isochron
Everest	GHS Low	Pegmatite	6.4		Kfs, Minimum age
Everest			7.5		Bt, Isochron
Everest			7.7		Ms, Isochron
Everest	GHS Low	Bt-Gneiss	3.6		Kfs, Minimum age
Everest			9.1		Bt, Isochron
Everest	MCT zone	Amphibolite	2.4		Hbl, Minimum age
Everest	MCT zone	Amphibolite	20.9		Hbl, Isochron
Everest			58.3		Bt, Isochron
Everest	MCT zone	Bt-Gneiss	88.8		Bt, Minimum age

Region	Rock Unit	Rock Type	Ar-Ar age (Ma)	K-Ar age (Ma)	Remarks
Everest	MCT zone	Augen Gneiss	8		Kfs, Minimum age
Everest			36.3		Bt, Minimum age
Everest			12		Ms, Isochron
Copeland et al, 1987					
North Side Everest	GHS top	Leucogranite	17.1		Bt
North Side Everest	GHS top	Leucogranite	16.7		Ms
North Side Everest	GHS top	Leucogranite	16.2		Kfs
Krummenacher et al, 1978					
Lho La pass		Leucogranite		19	K-Ar, Bt
Pumori		Leucogranite		47	K-Ar, Bt
Everest Basecamp		Leucogranite		19	K-Ar, Bt
north side Nuptse		mica schist		17	K-Ar, Bt
north side Nuptse		amphibolite		24	K-Ar, Hbl
north side Nuptse		biotite gneiss		18	K-Ar, Bt
north side Nuptse		amphibolite		56	K-Ar, amphibole
Pangboche		amphibolite		40	K-Ar, Bt
Pangboche		amphibolite		350	K-Ar, Hbl
Tyangboche		biotite gneiss		16	K-Ar, Bt
South of Namche	GHS Low	augen gneiss		13.4	K-Ar, Bt
South of Namche	GHS Low	migmatite		10.5	K-Ar, Bt
South of Namche	GHS Low	migmatitic diorite		10	K-Ar, Bt
South of Ghat	GHS Low	biotite gneiss		14	K-Ar, Bt
Puiyan	MCT zone	Augen Gneiss		9	K-Ar, Bt
Puiyan	MCT zone	Bt-Gneiss		5.5	K-Ar, Bt

Region	Rock Unit	Rock Type	Ar-Ar age (Ma)	K-Ar age (Ma)	Remarks
north of KhariLa	MCT	Bt-Gneiss		3.4	K-Ar, Bt
north of KhariLa	MCT	mica schist		8.5	K-Ar, Bt
Villa and Lombardo, 1986					
Lhotse Nup Glacier	**leucogranite**	leucogranite	15.67		Ms
Lhotse Nup Glacier			15.87		Bt
Lhotse Nup Glacier	leucogranite	leucogranite	15.35		Ms
Lhotse Nup Glacier			15.32		Bt
Lhotse Nup Glacier	contact metamorphic	amphibole	17		
Sakai et al, 2013					
Taplejung	GHC	Kyanite Gneiss	21.45		Bt (minimum)
Taplejung	MCT Zone upper part ??)	Schistose Gneiss	21.04		Bt (minimum)
Taplejung	Mitlung Augen Gneiss	Augen Gneiss	25.01		Bt
			13.78		Ms
Taplejung	Tamor River Granite	Granite			
Taplejung	Tamor River Granite	mylonitic granite	1562		Ms
Taplejung	Tamor River Granite	Granite (boundary)	1674		Ms
Taplejung	Kabeli Khola Granite	Granite	1642		Ms
Taplejung	Kabeli Khola Granite	Granite	1669		Ms
Taplejung	Amarpur Granite	Granite	1558		Ms
Imayama et al, 2012					
Taplejung (Ghunsa Khola)	Kangchenjunga Migmatites	Granitic orthogneiss		16.23	Bt

Region	Rock Unit	Rock Type	Ar-Ar age (Ma)	K-Ar age (Ma)	Remarks
Taplejung (Ghunsa Khola)	Kangchenjunga Migmatites			20.1	Bt
Taplejung (Ghunsa Khola)	Kangchenjunga Migmatites	Sil-migmatitic gneiss		9	Bt
Taplejung (Ghunsa Khola)	Kangchenjunga Migmatites	Sil-migmatitic gneiss		20.2	Bt
Taplejung (Ghunsa Khola)	Junbesi Paragneiss	Ky-Sil migmatite gneiss		26.8	Bt
Taplejung (Ghunsa Khola)	MCT zone	Mylonitic augen gneiss		16.73	Bt

A6. Thermochronology of Sikkim-Bhutan Himalaya

Region	Rock Unit	Rock Type	Ar-Ar age (Ma)	K-Ar age (Ma)	Remarks
Kellet et al., 2013					
Sikkim	GHS	deformed leucosome	13.23		Ms, plateau
Sikkim	GHS	deformed leucogranite	12.4		Ms, total gas age
Sikkim	GHS	fine grained aplite	13		Ms, total gas age
Sikkim	GHS	Non-foliated leucosome	13.26		Ms, plateau
Gong et al., 2011					
Yadong, Eastern Himalaya	GHS top (surrounding Yadong Granulite)	Biotite Moyite	12.6		Kfs, Gong et al 2004
			11.5		Bt, Gong et al 2005
Yadong, Eastern Himalaya	GHS top (Yadong Granulite)	Granulite (High Pressure)	48.5		Bt, Gong et al 2006
			31.8		Hbl, Gong et al 2007
Yadong, Eastern Himalaya	GHS middle	Granitic Gneiss ms-bt	13.9		ms
			11		bt
Yadong, Eastern Himalaya	GHS middle	Granitic Gneiss mb-bt	11.3		bt
McQuarrie et al., 2014					
Central Bhutan, Wang Chu	GHS	Upper Metasediment	11.6		detrial muscovite
Central Bhutan, Wang Chu	GHS	Upper Metasediment	11.7		detrial muscovite
Central Bhutan, Wang Chu	GHS	Lower Metasediment	11.7		detrial muscovite
Central Bhutan, Wang Chu	GHS	Lower Metasediment	11.5		detrial muscovite
Central Bhutan, Wang Chu	GHS	Lower Metasediment	10.6		detrial muscovite

Region	Rock Unit	Rock Type	Ar-Ar age (Ma)	K-Ar age (Ma)	Remarks
Central Bhutan, Wang Chu	Immediate HW of MCT, GHS	Paragneiss	11.7		ms
Central Bhutan, Wang Chu	Immediate HW of MCT, GHS	Paragneiss	11.4		ms
Long et al., 2012					
Eastern Bhutan, Kuru Chu	Lower LH Thrust Sheet	Jaishidanda,quartzite	8.4		Ms integrated
Eastern Bhutan, Kuru Chu	Lower LH Thrust Sheet	Shumar, quartzite	9.18		Ms, plateau
Eastern Bhutan, Kuru Chu	Lower LH Thrust Sheet	shumar, quartzite	12.95		Ms integrated
Eastern Bhutan, Kuru Chu	LH, Shumar Thrust sheet	daling, orthogneiss	11.78		Ms integrated
Eastern Bhutan, Kuru Chu	LH, Shumar Thrust sheet	shumar quartzite	12.11		Ms integrated
Eastern Bhutan, Kuru Chu	Shumar Thrust sheet, klippe	daling, quartzite	1395.7		Ms integrated
Eastern Bhutan, Kuru Chu	Baxa group horse, in upper LH duplex	baxa, quartzite	14.78		ms, minimum age
Eastern Bhutan, Kuru Chu	Diuri formation thrust sheet	diuri, diamictite	1020		ms, minimum age
Stuwe & Foster, 2001					
Eastern Bhutan, Tashigang	GH	gt-bi-mu-q	14.1		ms, isochron
			43.4		bt, total fusion age
Eastern Bhutan, Tashigang	GH	bi-mu-q-plag	11.1		ms, isochron
Eastern Bhutan,			11.2		bt, minimum age
Eastern Bhutan, Tashigang	GH	bi-mu-q-plag			
Eastern Bhutan, Tashigang	GH	bi-mu-q-plag	14.1		ms-total fusion

Region	Rock Unit	Rock Type	Ar-Ar age (Ma)	K-Ar age (Ma)	Remarks
			18		bt, minimum
Eastern Bhutan, Tashigang	GH	gt-bi-mu-ky-q	11.6		ms, isochron
			19.8		bt, average of central part

Appendix B: Photomicrographs of specimen used for $^{40}Ar/^{39}Ar$ thermochronology analyses

B1. KM 031

A relict biotite showing undulose extinction and feldspar replaced by muscovite.

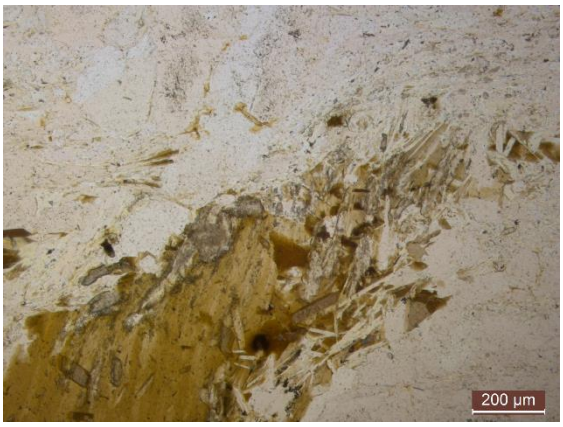

Under plane polarized light

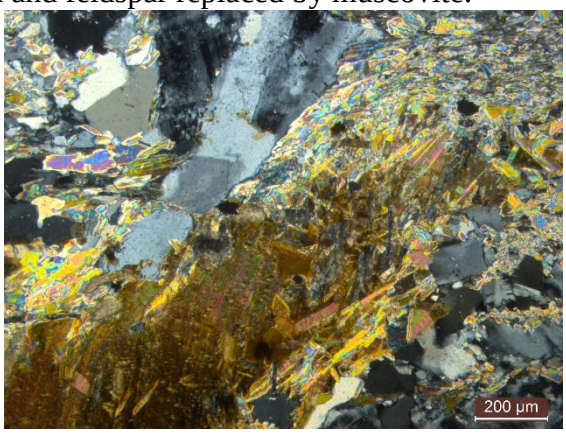

Under crossed polarized light

A coarse grained older generation muscovite shows undulose extinction while finer grained biotite and muscovite of later generation define the foliation plane.

Under plane polarized light

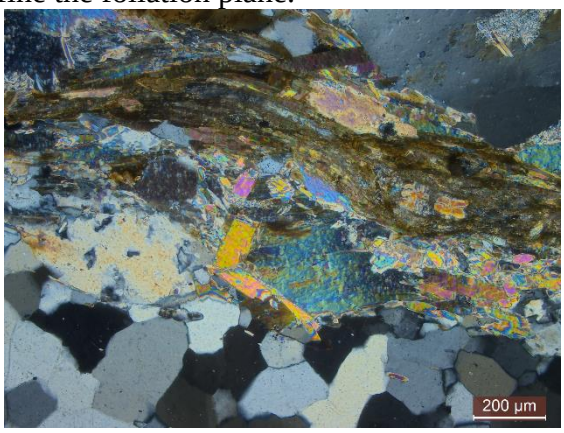

Under crossed polarized light

B2. KM 025

Coarse grained muscovite of older generation shows evidence of deformation and and undulose extinction.

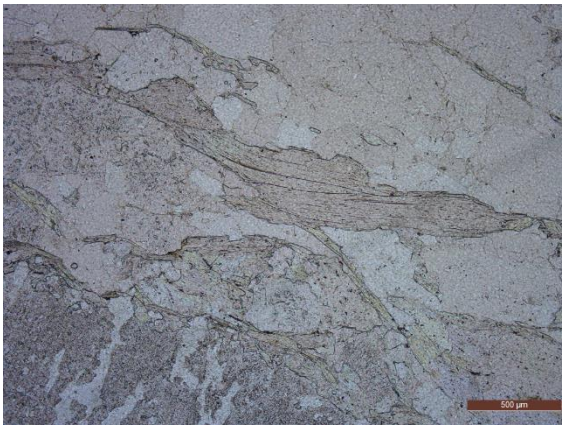

Under plane polarized light

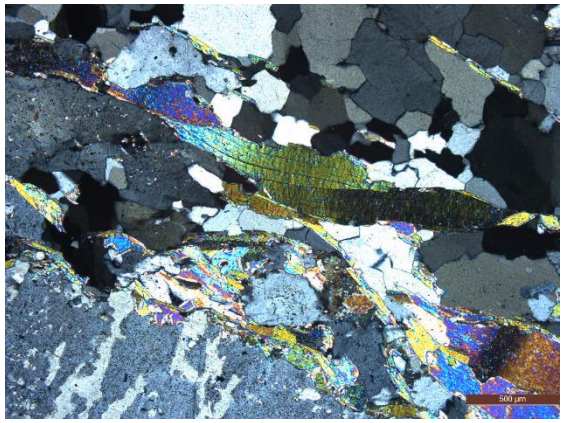

Under crossed polarized light

A coarse grained muscovite of older generation being replaced by finer grained muscovite of second generation.

Under plane polarized light

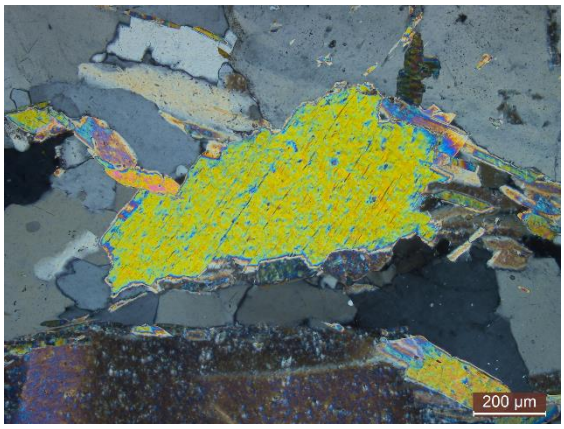

Under crossed polarized light

B3. KM 014

Coarse grained muscovite of older generation being replaced by finer grained biotite and muscovite of new generation that define the foliation plane.

Under plane polarized light

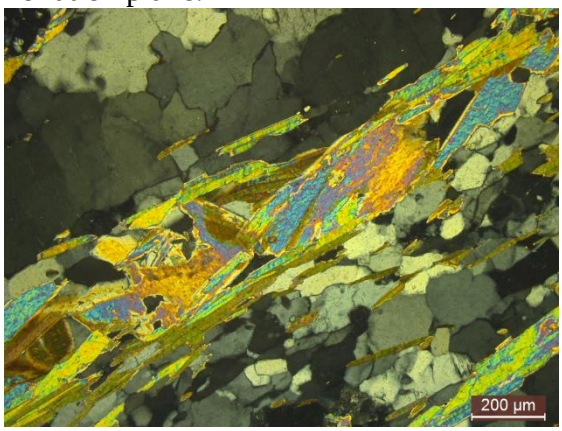

Under crossed polarized light

B4. KM 013

Deformed coarse grained muscovite of first generation showing undulose extinction replaced by finer grained newer generation muscovite.

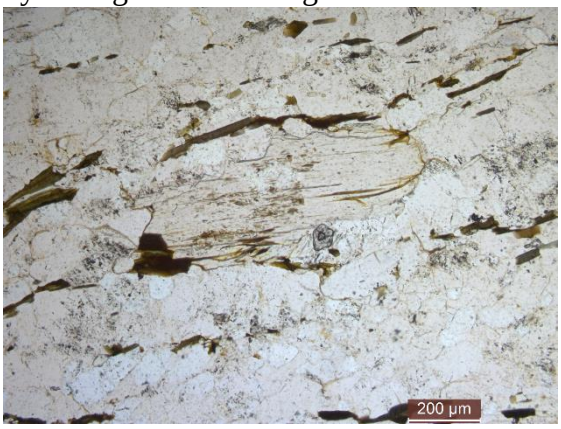

Under plane polarized light

Under crossed polarized light

Appendix C: Photographs of mica grains used for $^{40}Ar/^{39}Ar$ thermochronology Analyses

C1. KM 078

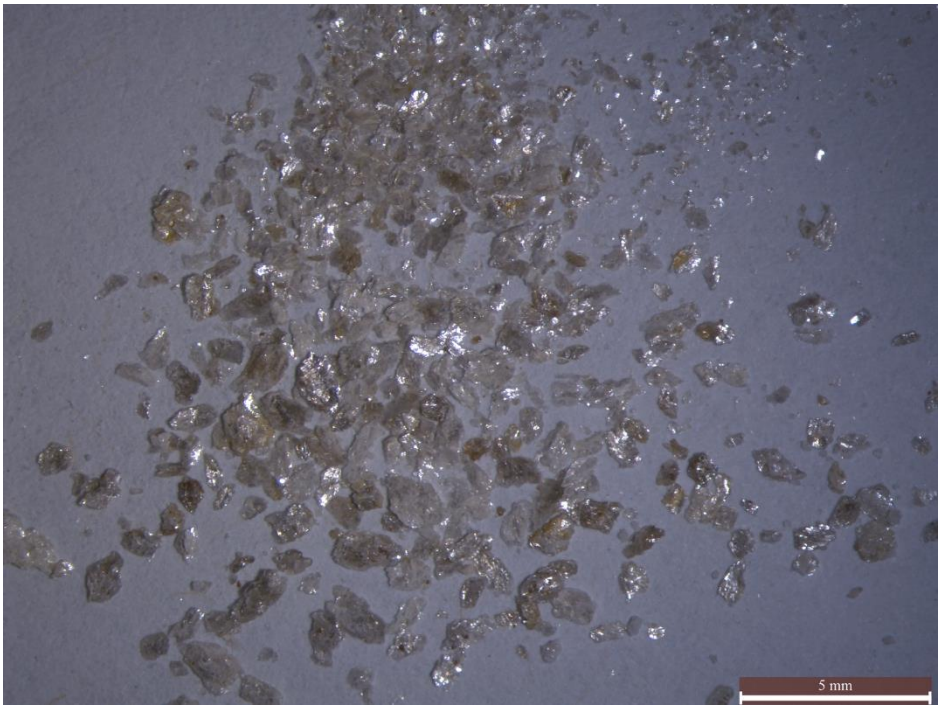

KM 078 Muscovite (1X)

C2. KM 074

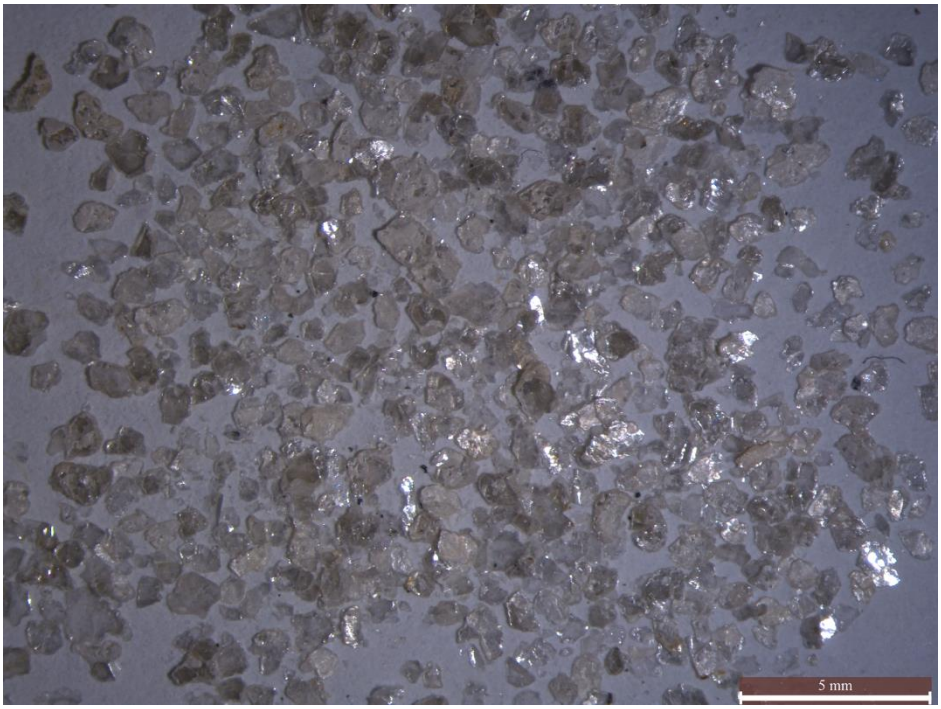

KM 074 Muscovite (1X)

C3. KM 073

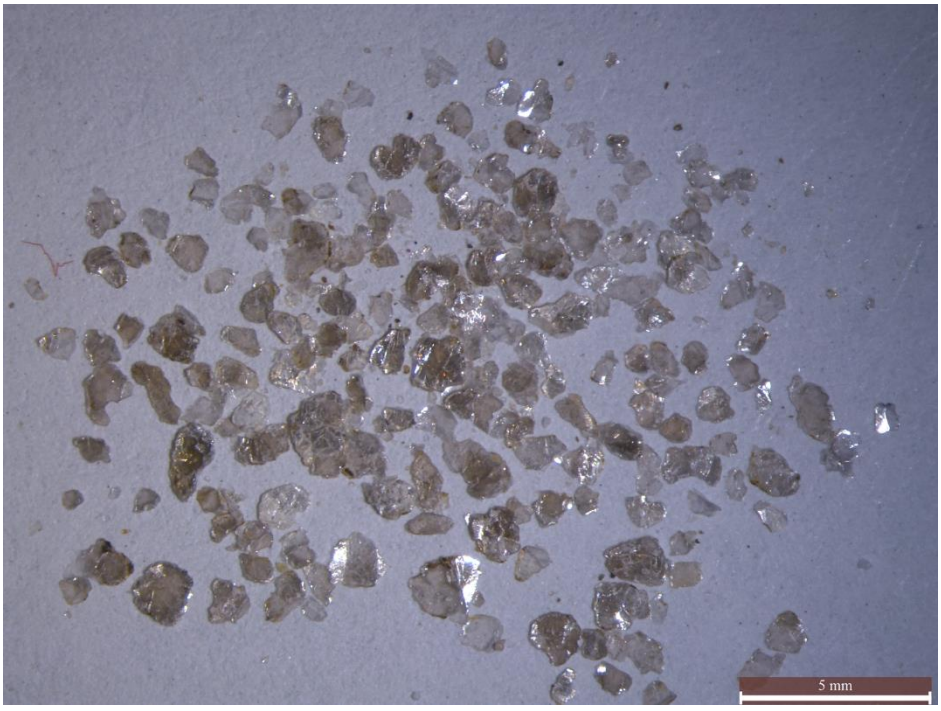

KM 073 Muscovite (1X)

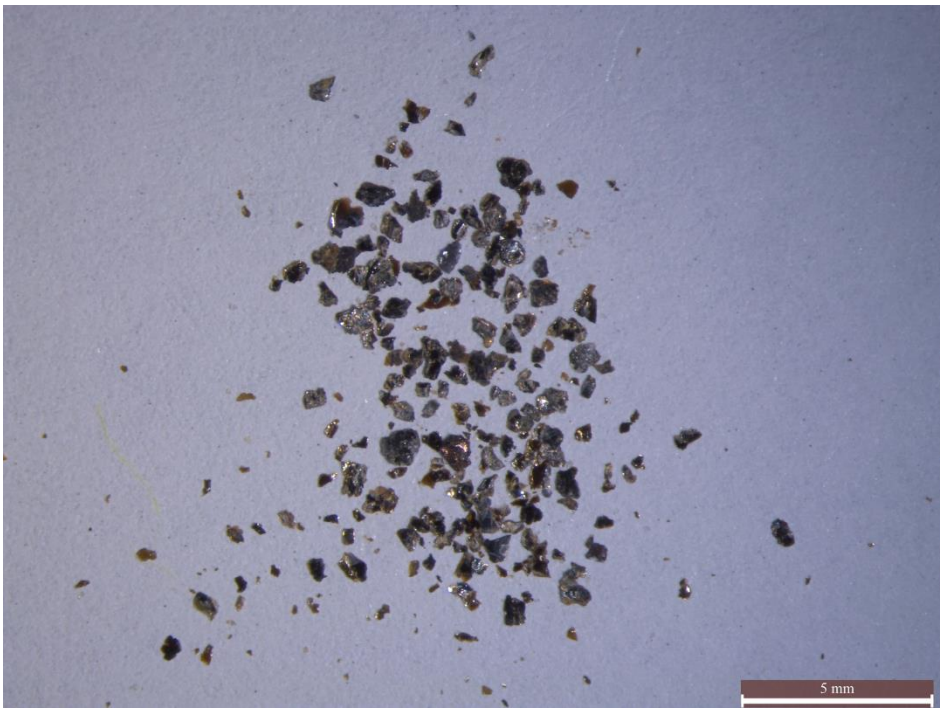

KM 073 Biotite (1X)

C4. KM 068

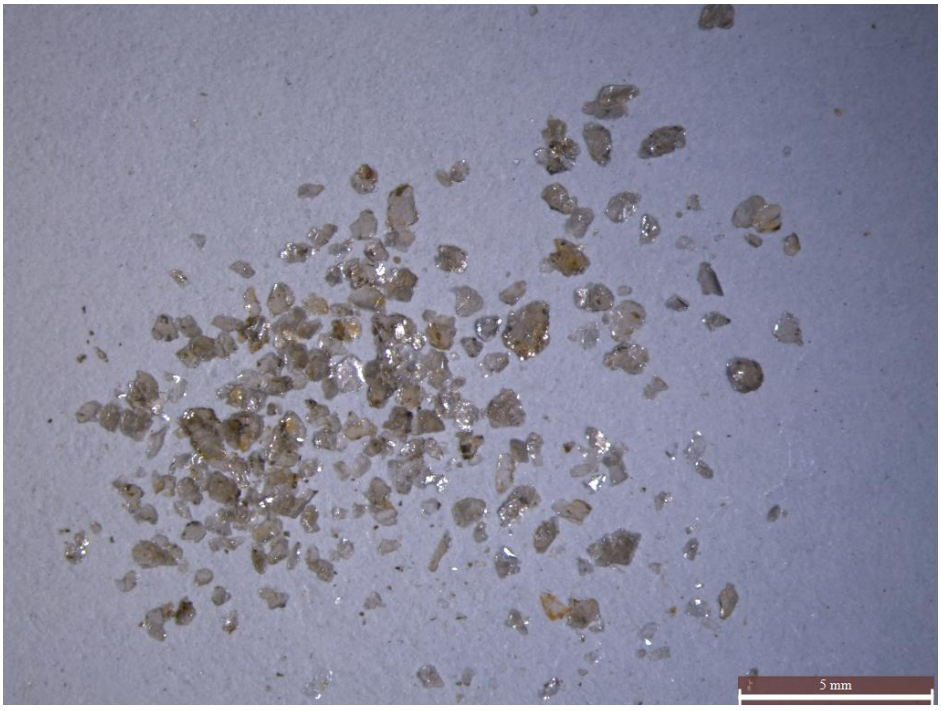

KM 068 Muscovite (1X)

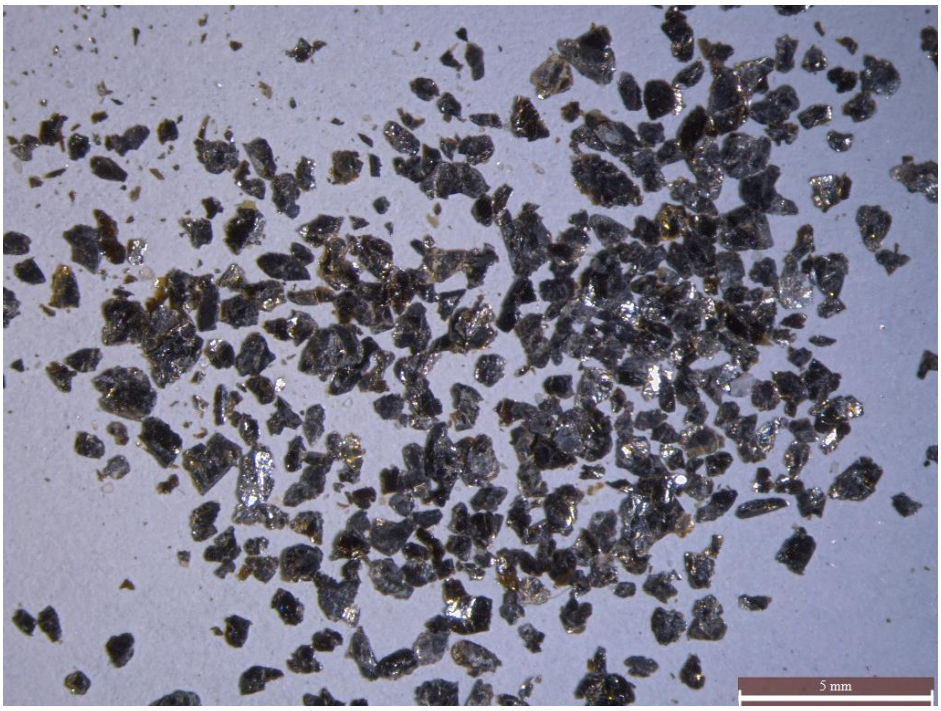

KM 068 Biotite (1X)

C5. KM 060

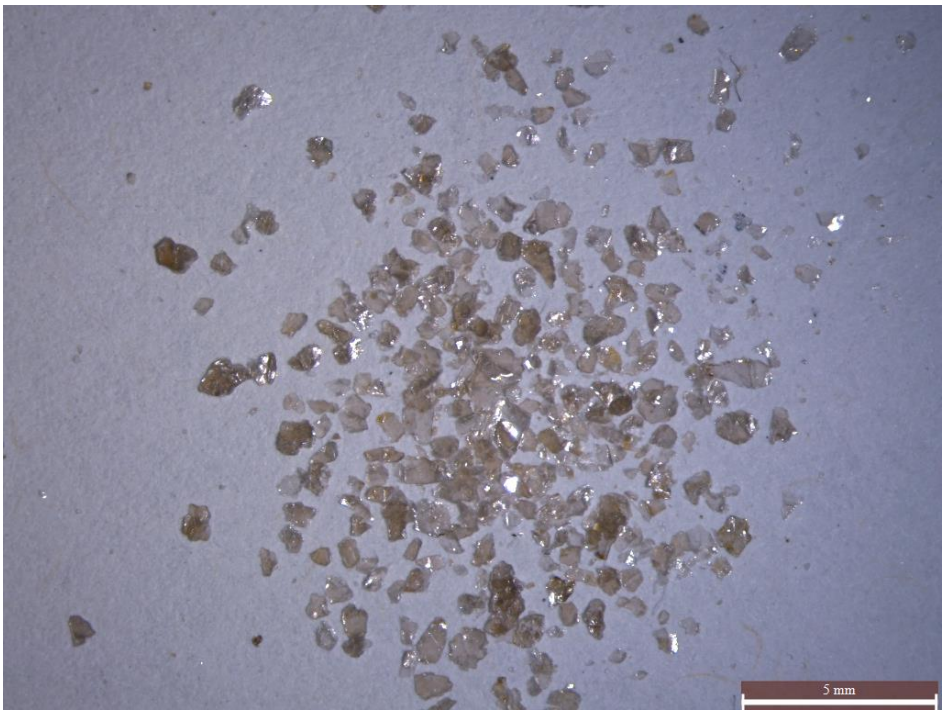

KM 060 Muscovite (1X)

C6. KM 054

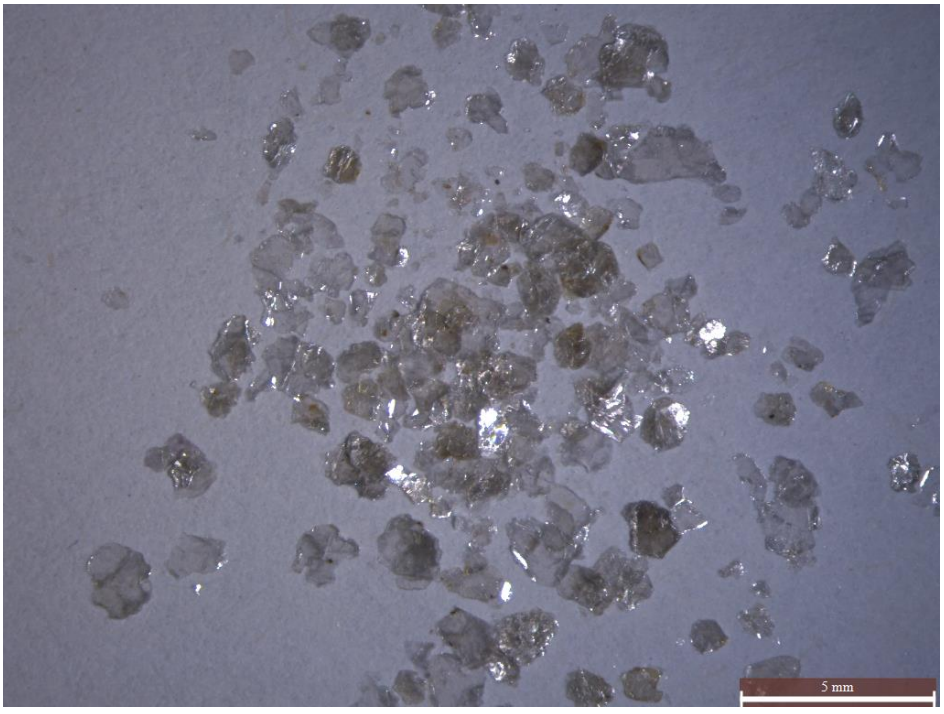

KM 054 Muscovite (1X)

C7. KM 053

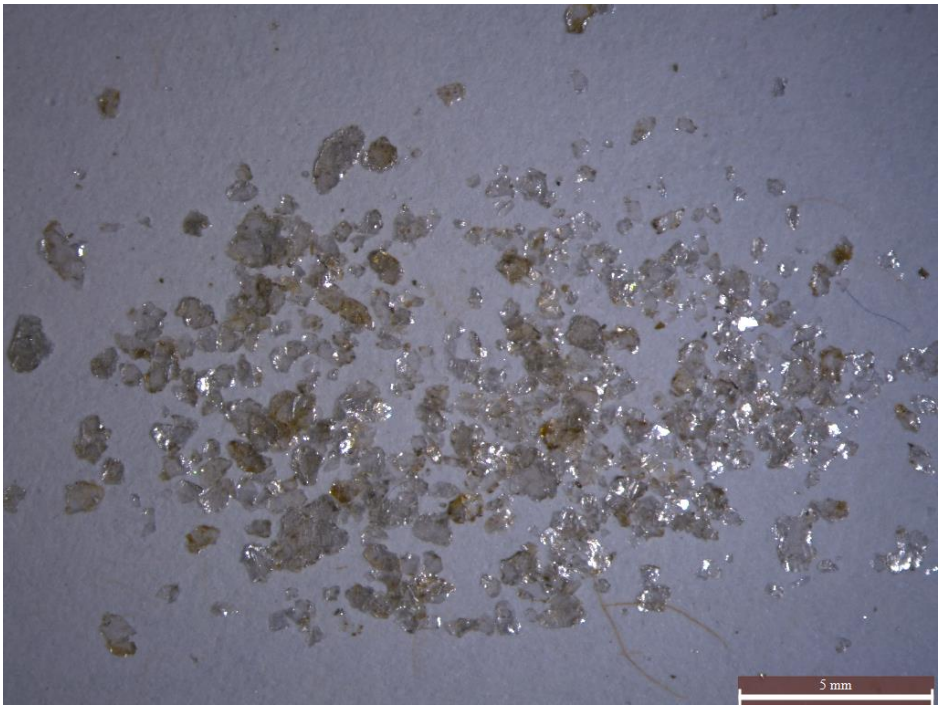

KM 053 Muscovite (1X)

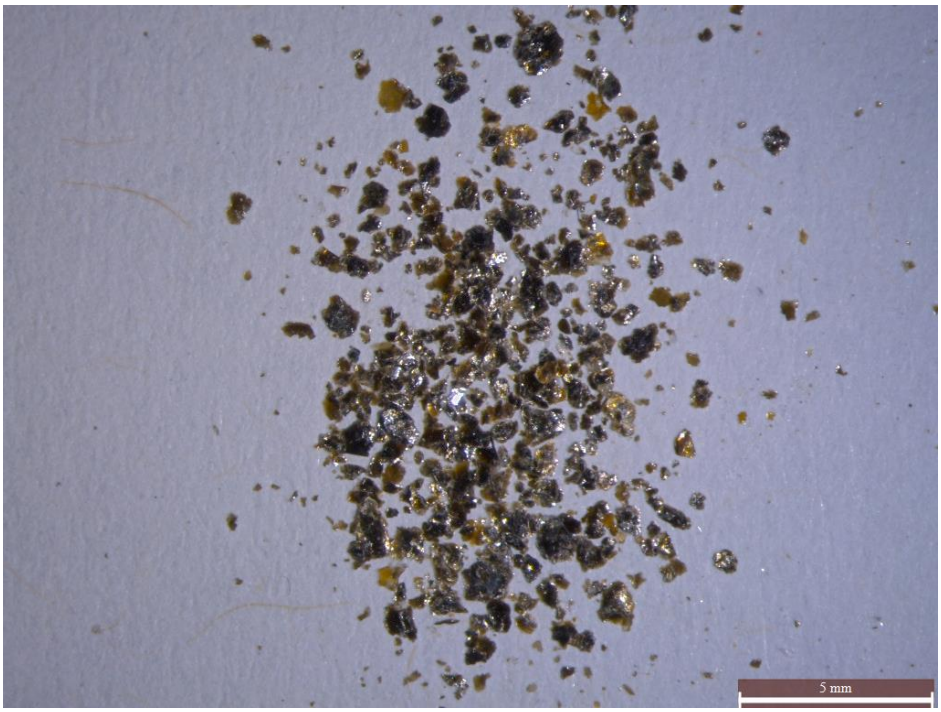

KM 053 Biotite (1X)

C8. KM 051B

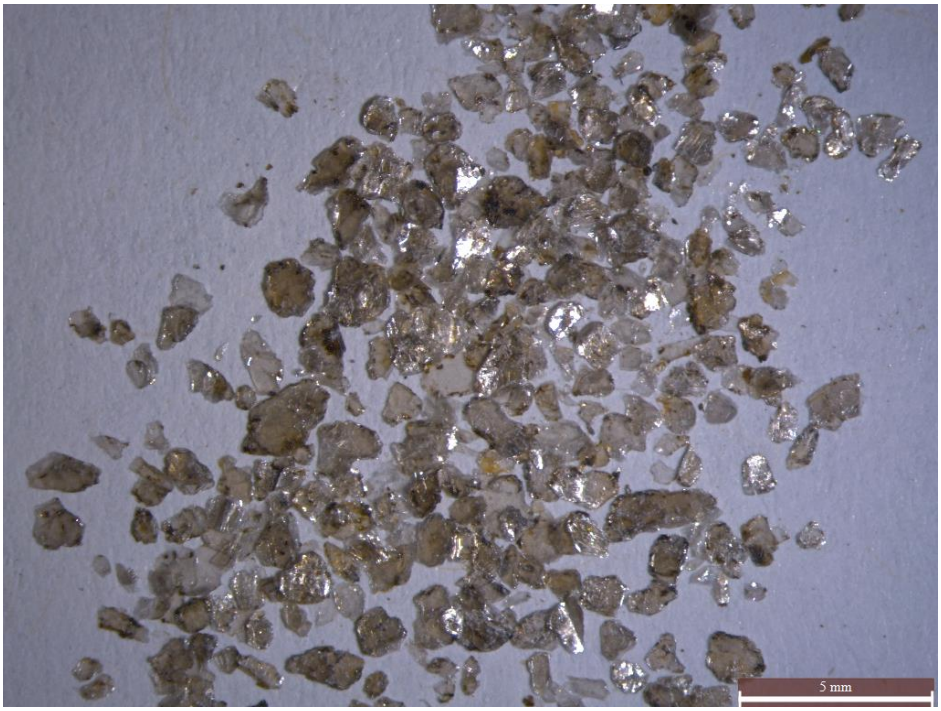

KM 051B Muscovite (1X)

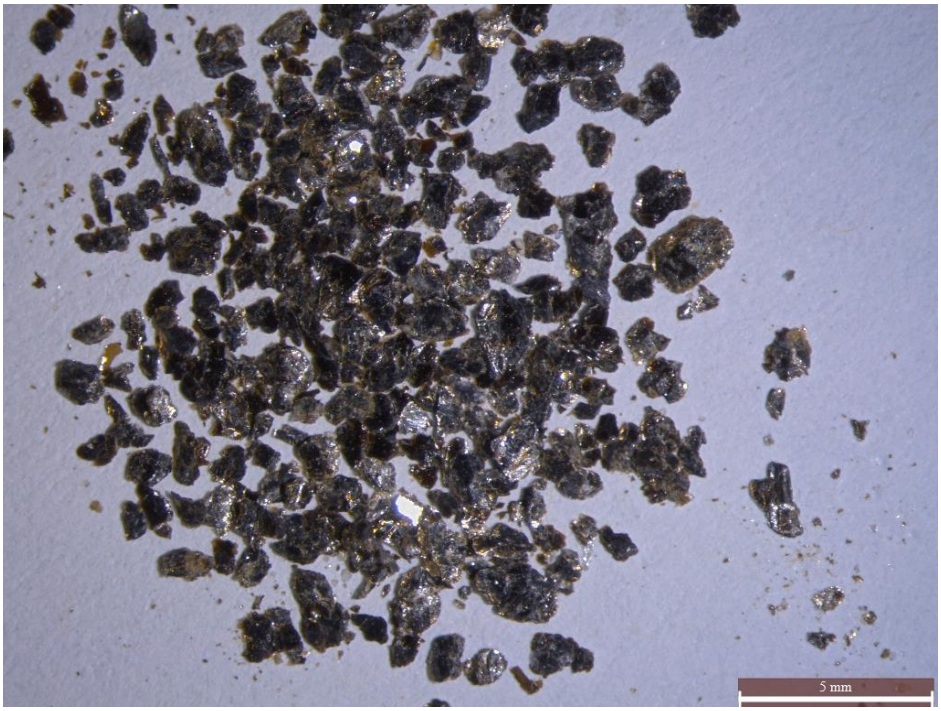

KM 051B Biotite (1X)

C9. KM 051A

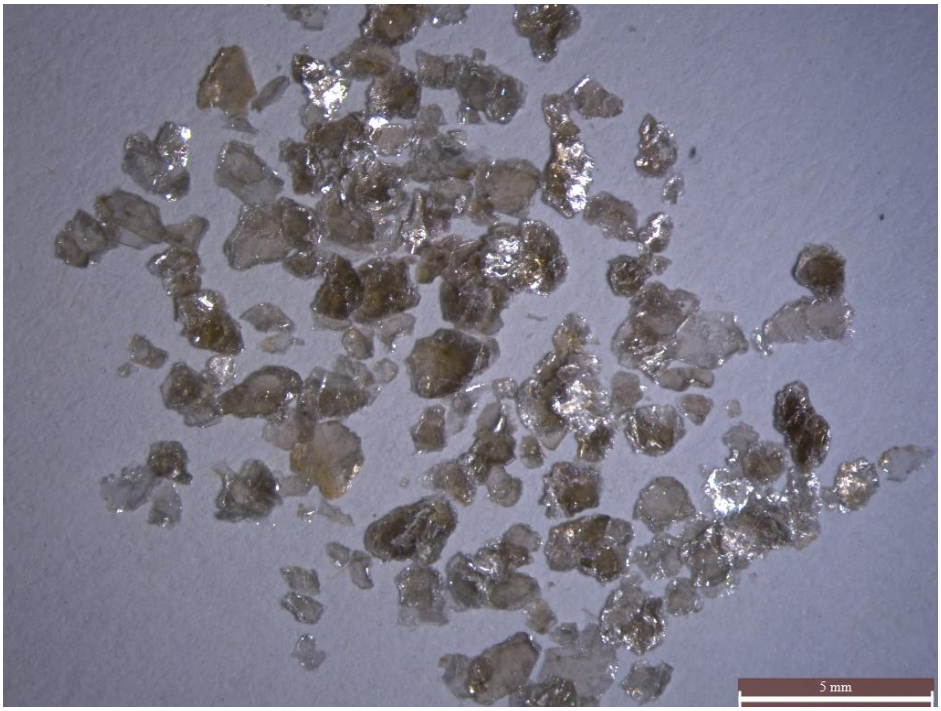

KM 051A Muscovite (1X)

C10. KM 031

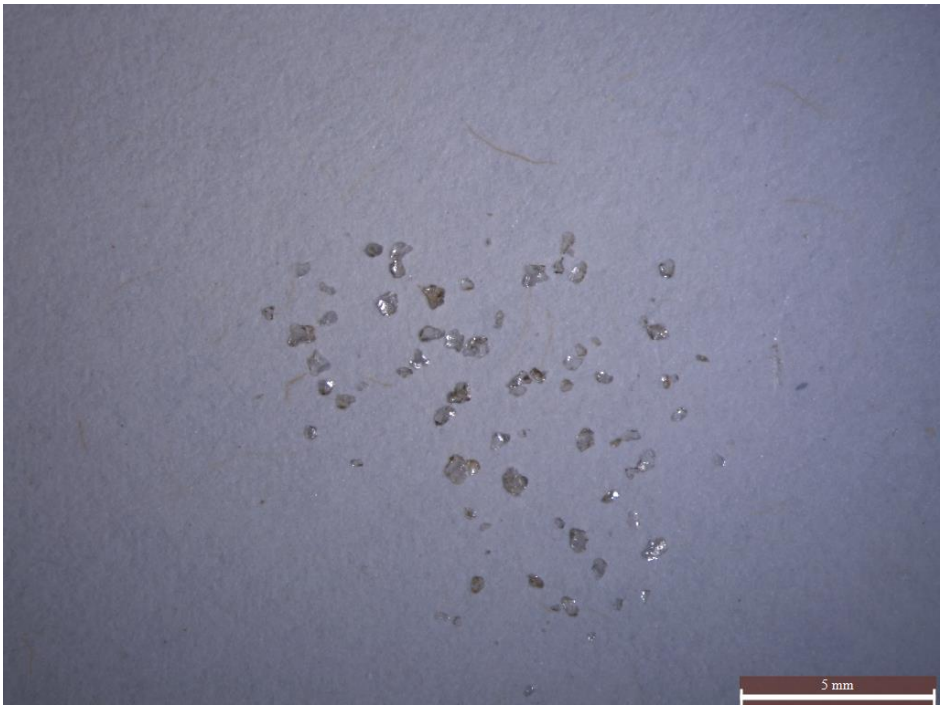

KM 031 Muscovite (1X)

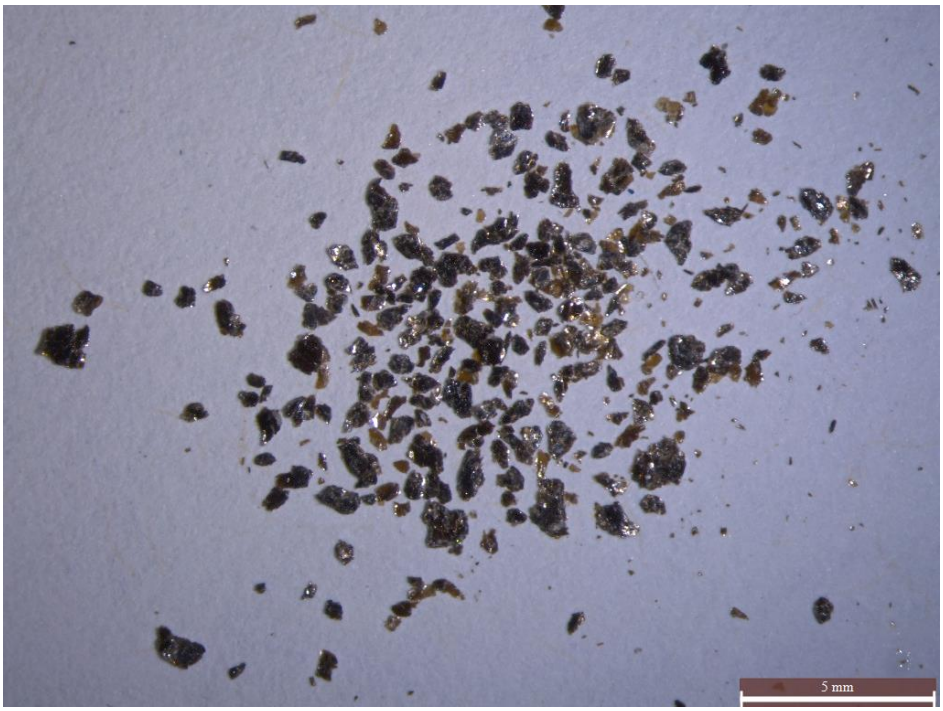

KM 031 Biotite (1X)

C11. KM 030

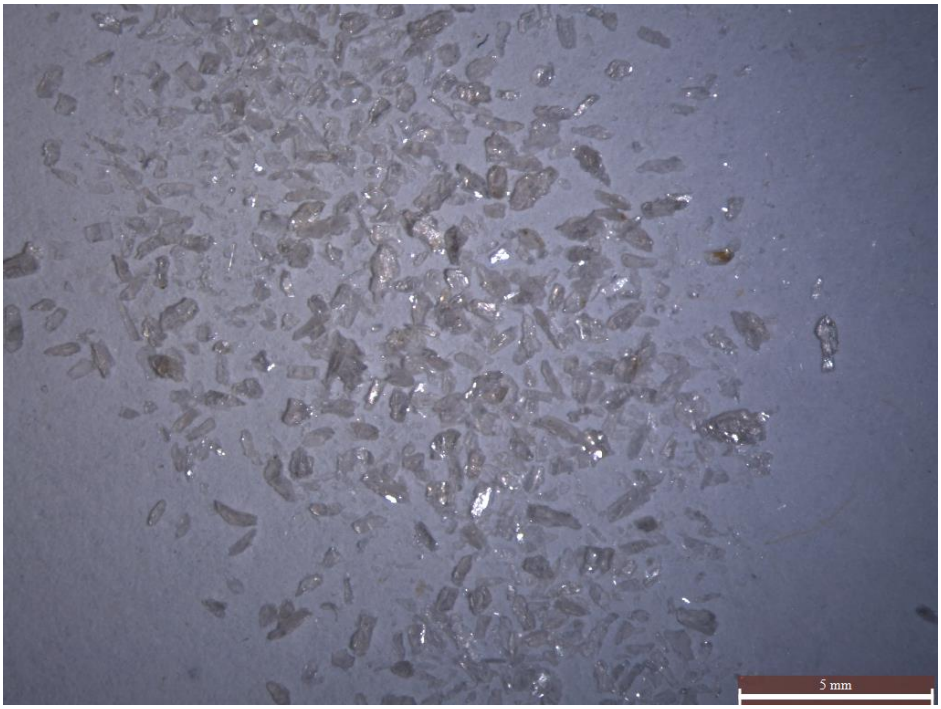

KM 030 Muscovite (1X)

C12. KM 025

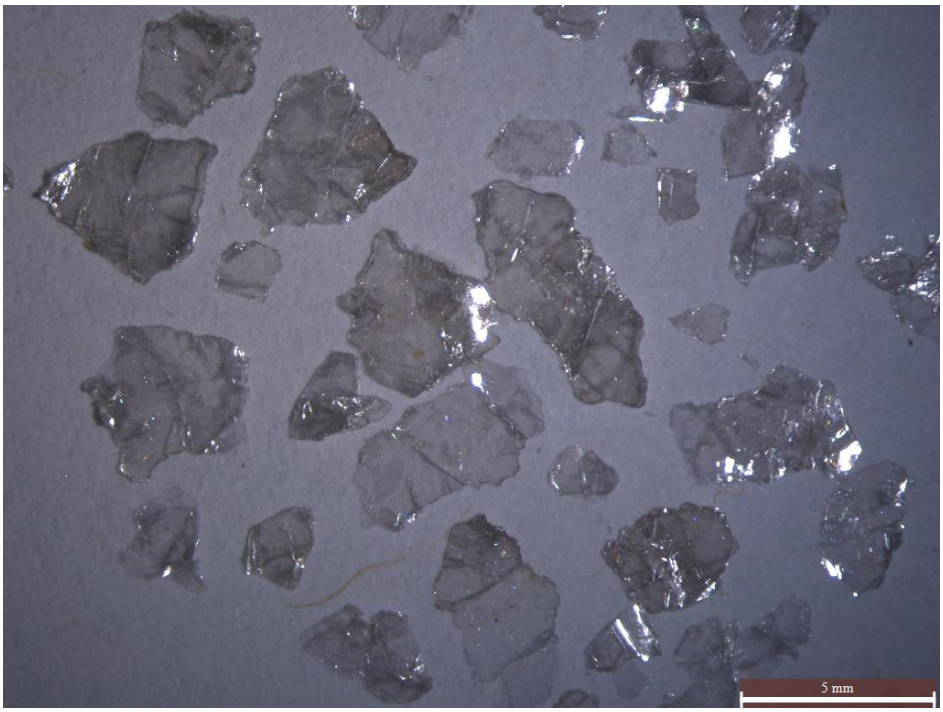

KM 025 Muscovite (1X)

C13. KM 014

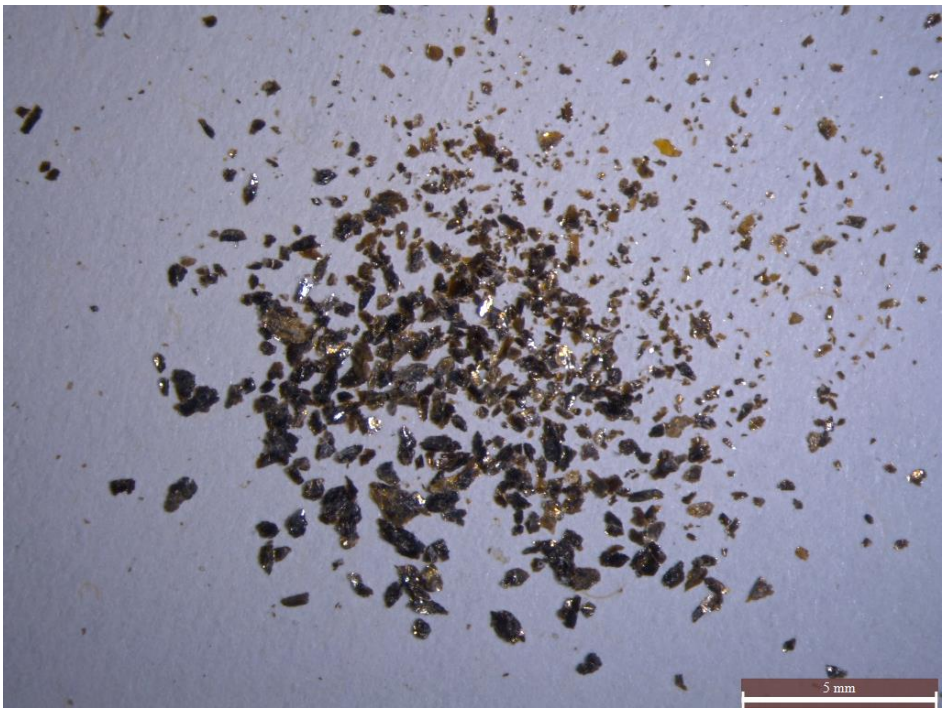

KM 014 Biotite (1X)

C14. KM 013

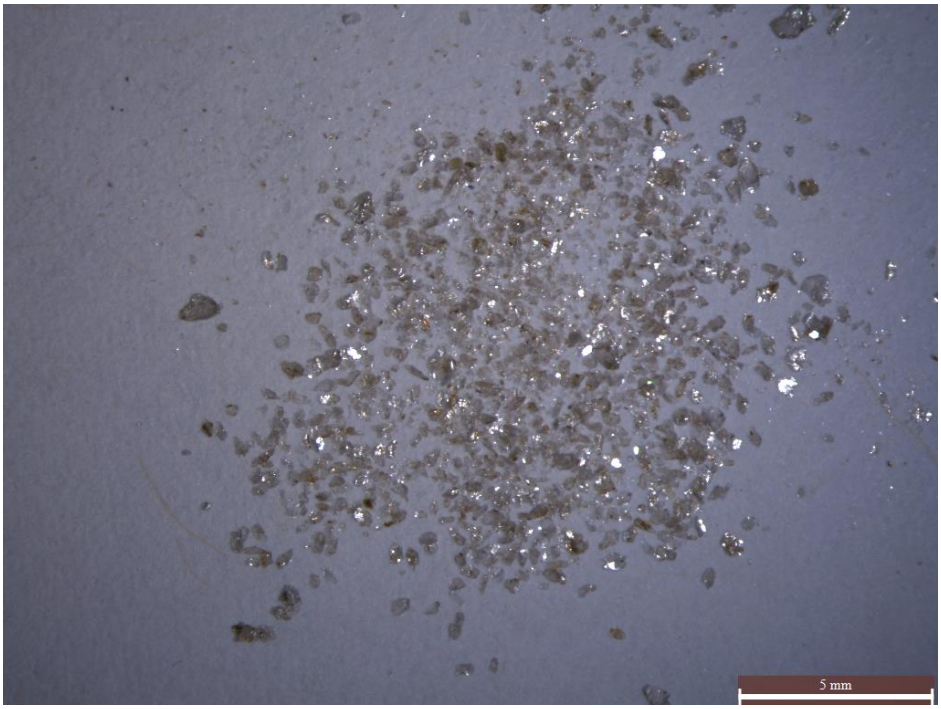

KM 013 Muscovite (1X)

C15. LK 032

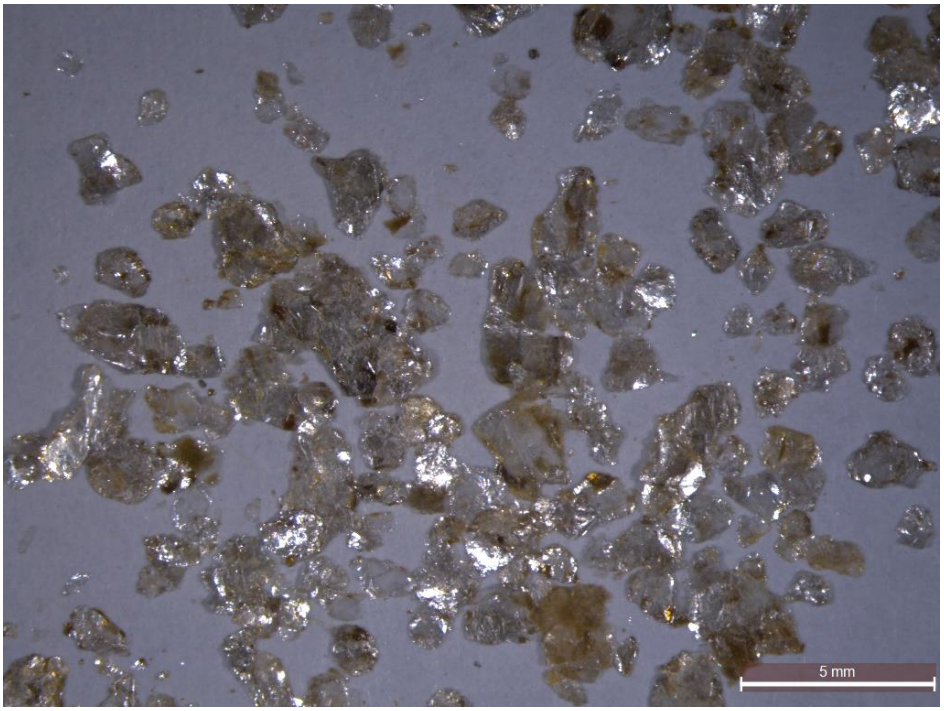

LK 032 Muscovite (1X)

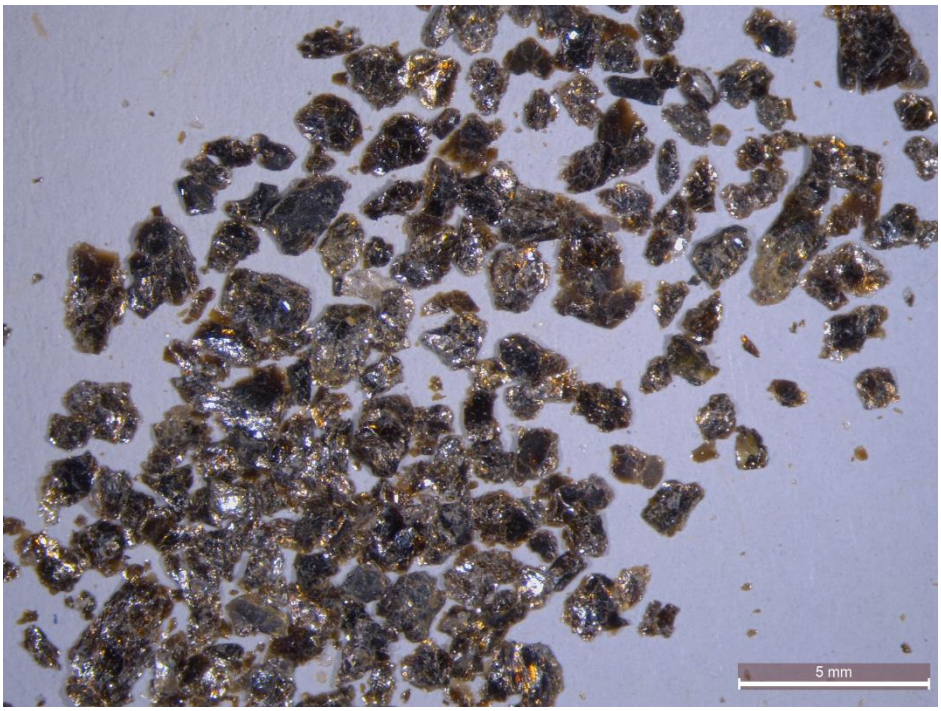

LK 032 Biotite (1X)

C16. LK 039

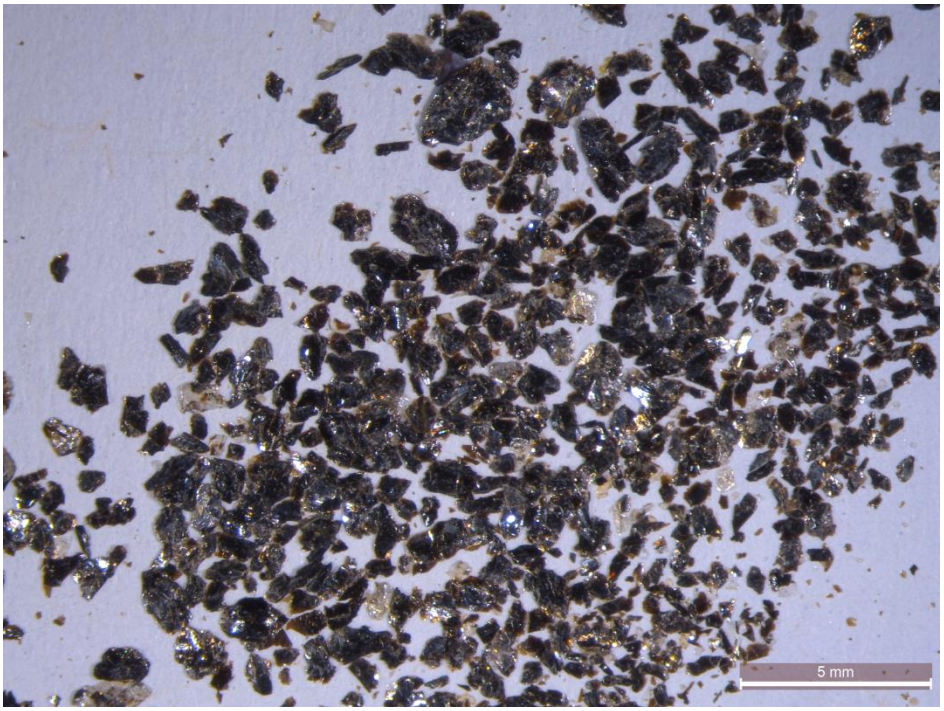

LK 039 Biotite (1X)

C17. LK 046

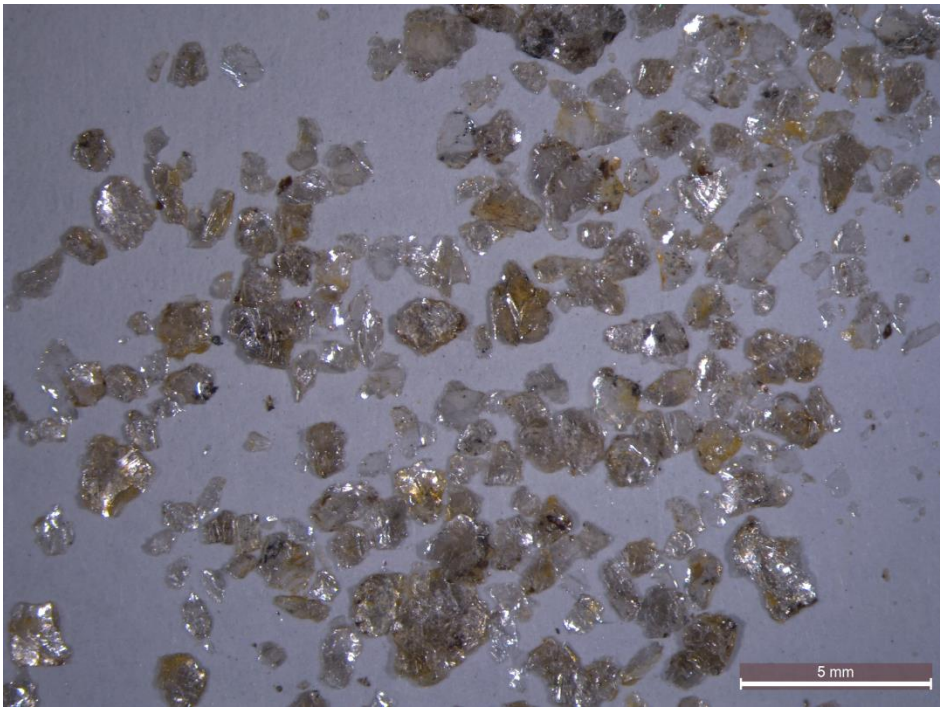

LK 046 Muscovite (1X)

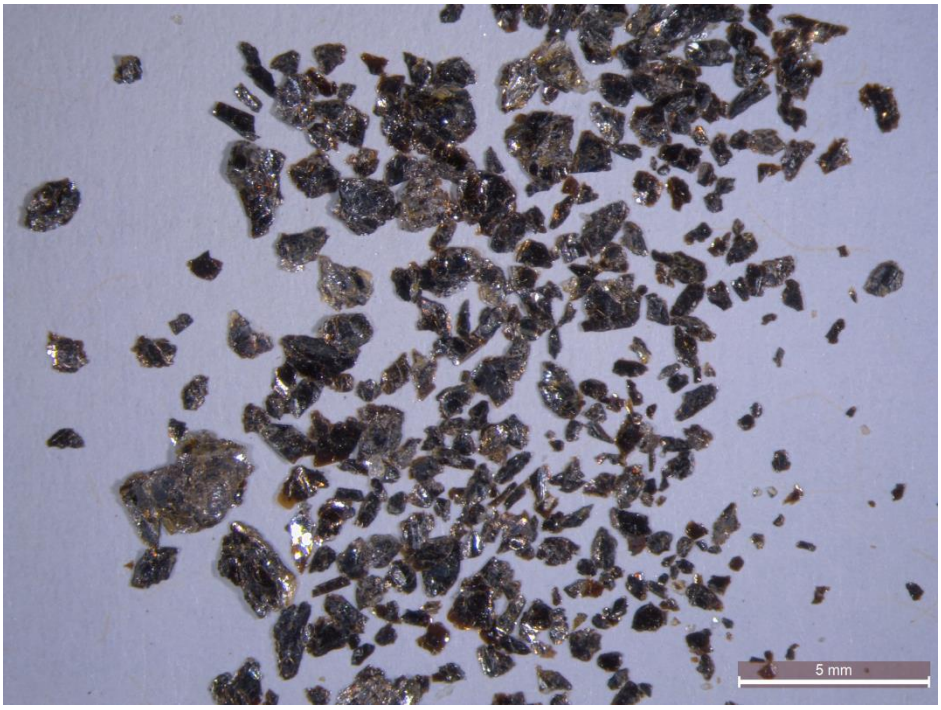

LK 046 Biotite (1X)

C18. LK 048

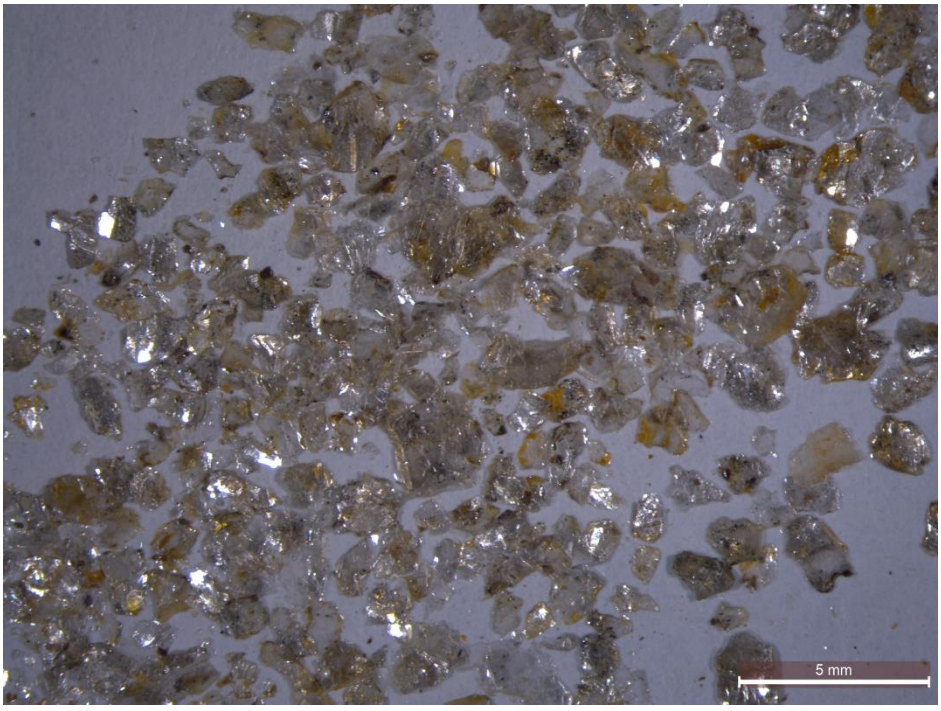

LK 048 muscovite (1X)

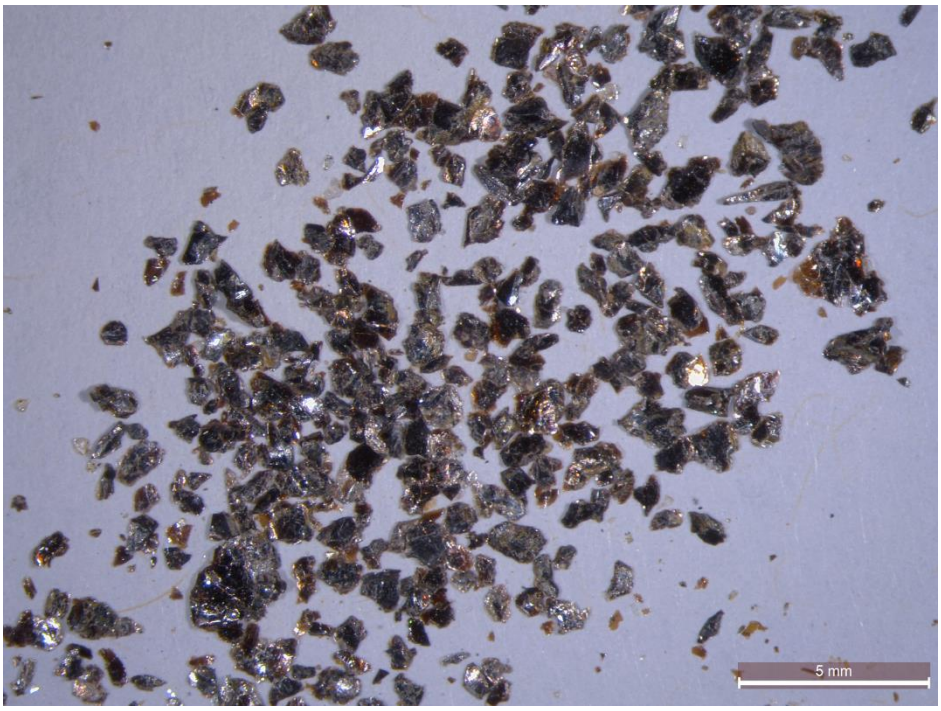

LK 048 biotite (1X)

C19. LK 051

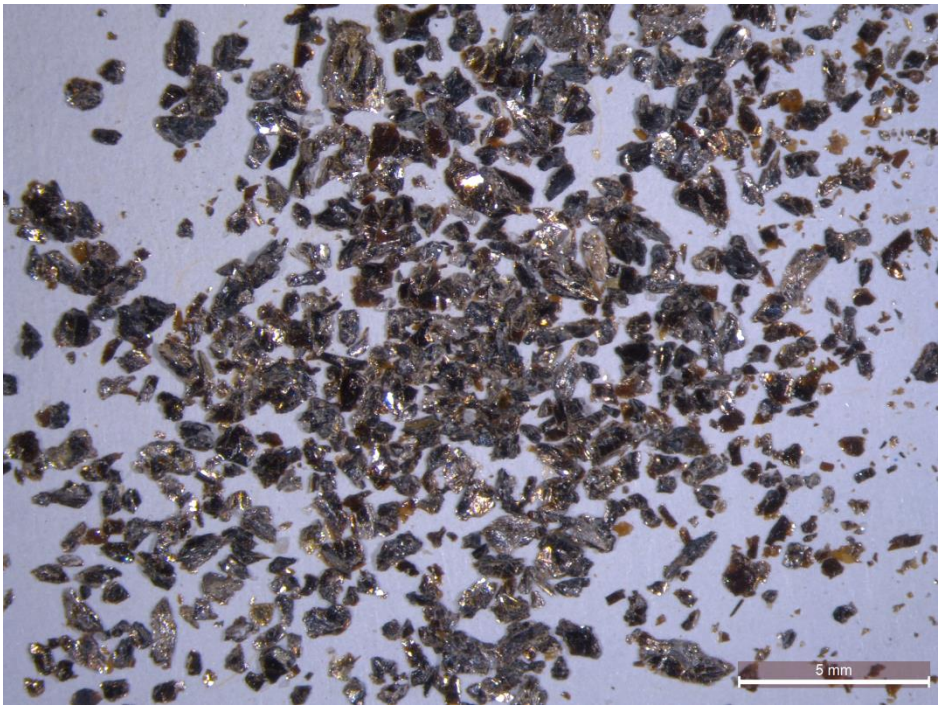

LK 051 biotite (1X)

C20. LK 052

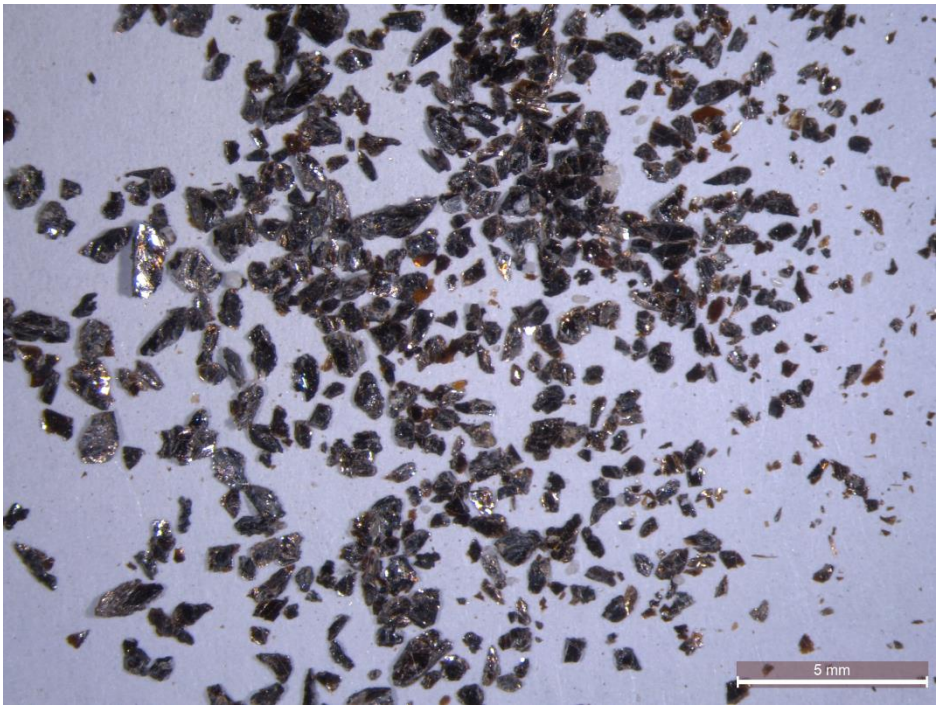

LK 052 biotite (1X)

C21. LK 055

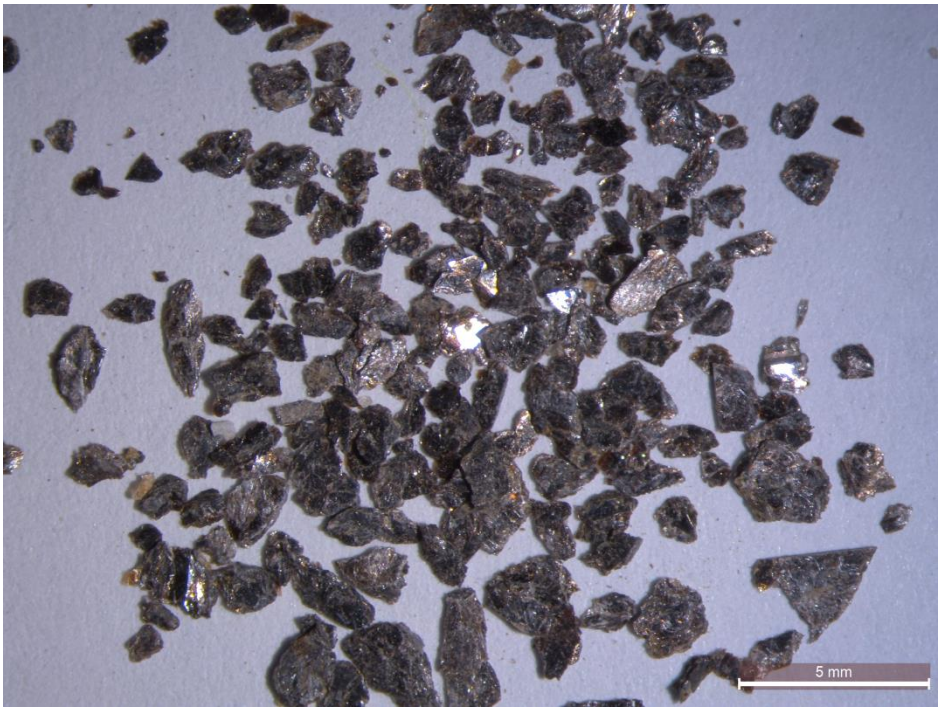

LK 055 biotite (1X)

C22. LK 059

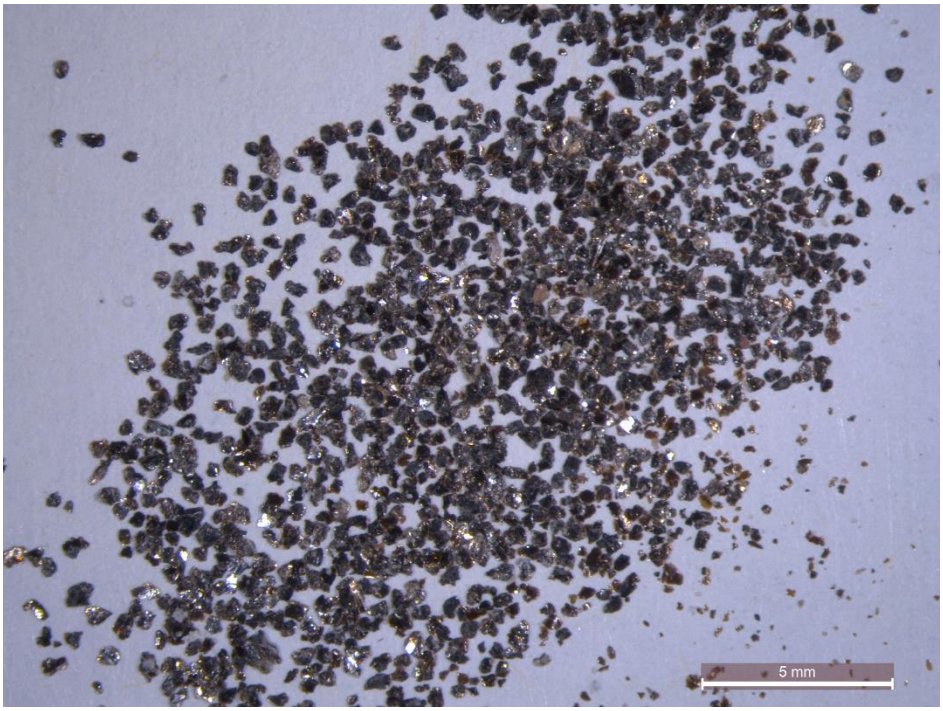

LK 059 biotite (1X)